
Aspects of nuclear collectivity studied in projectile Coulomb excitation experiments

Vom Fachbereich Physik
der Technischen Universität Darmstadt

zur Erlangung des Grades
eines Doktors der Naturwissenschaften (Dr. rer. nat.)

genehmigte Dissertation von
Thomas Möller M.Sc.
aus Fulda

Referent: Prof. Dr. Dr. h.c. Norbert Pietralla

Korreferent: Prof. Dr. Joachim Enders

Tag der Einreichung: 22. Mai 2014

Tag der Prüfung: 18. Juni 2014

Darmstadt 2014

D17



Abstract

Projectile Coulomb excitation experiments have been performed on the nuclei $^{130,132}\text{Ba}$, ^{154}Sm , and $^{194,196}\text{Pt}$. A detailed description of the experiments and the data analysis is given. The results on absolute decay rates of the low-lying collective states of these nuclei allow for a comparison with predictions from different theoretical models of nuclear quadrupole collectivity. For the nucleus ^{154}Sm the data on the decay rates of the states of the first $K = 0$ band support the assignment of this band as the beta band of this nucleus. The results for the nuclei $^{194,196}\text{Pt}$ allow for a comparison with the selection rules of the $O(6)$ dynamical symmetry of the Interacting Boson Model. The nucleus ^{196}Pt indeed manifests the $O(6)$ symmetry. The results on $B(M1; 2_i^+ \rightarrow 2_1^+)$ values of the nuclei $^{130,132}\text{Ba}$ complete the experimental data on the evolution of the one quadrupole-phonon state of mixed proton-neutron symmetry ($2_{1,ms}^+$) in the $A = 130$ mass region. The results support the previous observation of increased fragmentation of the $2_{1,ms}^+$ state for mid-shell nuclei, although one candidate of a $2_{1,ms}^+$ state of ^{130}Ba , if confirmed, would alter this interpretation.

Zusammenfassung

Experimente der Projektil-Coulombanregung sind an den Kernen $^{130,132}\text{Ba}$, ^{154}Sm und $^{194,196}\text{Pt}$ durchgeführt worden. Die Experimente und ihre Auswertung werden detailliert beschrieben. Die Ergebnisse in Form von absoluten Werten von Zerfallsraten tiefliegender kollektiver Zustände dieser Kerne ermöglichen Vergleiche mit Vorhersagen unterschiedlicher theoretischer Modelle nuklearer Quadrupolkollektivität. Für den Kern ^{154}Sm konnte anhand der Ergebnisse der Zerfallsraten der ersten angeregten $K = 0$ Bande eine Zuweisung dieser Bande als beta-Bande bestätigt werden. Die Ergebnisse für die Kerne $^{194,196}\text{Pt}$ ermöglichten Vergleiche mit den Auswahlregeln der dynamischen $O(6)$ Symmetrie des Interacting Boson Modells. Der Kern ^{196}Pt stellt tatsächlich eine Manifestierung der $O(6)$ Symmetrie dar. Die Ergebnisse der $B(M1; 2_i^+ \rightarrow 2_1^+)$ Werte in den Kernen $^{130,132}\text{Ba}$ vervollständigen die experimentellen Daten zum ein-Quadrupol-Phonon Zustand gemischter Proton-Neutron Symmetrie ($2_{1,ms}^+$) in der $A = 130$ Massenregion. Die

Ergebnisse bestätigen frühere Beobachtungen einer zunehmenden Fragmentierung dieses Zustandes für Kerne in der Schalenmitte, obwohl ein Kandidat des $2_{1,ms}^+$ Zustandes im Falle seiner Bestätigung diese Interpretation noch verändern kann.

Contents

Abstract / Zusammenfassung	1
Contents	5
1. Introduction	7
2. Theoretical approaches to nuclear quadrupole collectivity	11
2.1. Nuclear Shell Model	11
2.2. Vibrational and Rotational Nuclei	14
2.2.1. Vibrator	15
2.2.2. Rotor	17
2.2.3. γ -soft nuclei	20
2.3. Interacting Boson Model	21
2.3.1. Basics	21
2.3.2. The dynamical symmetries of the IBA	23
U(5)	25
SU(3)	26
O(6)	27
2.3.3. The pn version of the Interacting Boson Model, IBM-2	29
<i>F</i> -spin and mixed symmetric states	30
<i>Q</i> -Phonon Scheme	32
Signatures of mixed-symmetric states	32
2.4. Transitional Nuclei	33
2.4.1. E(5)	34
2.4.2. X(5)	35
2.4.3. The confined- β -soft rotor model	36

3. Experimental Method	41
3.1. Coulomb excitation	41
3.2. Experimental Principle	45
3.2.1. Basic Concept	45
3.2.2. Connection to nuclear structure observables	48
3.3. Experimental Setup	50
3.3.1. ATLAS accelerator	50
3.3.2. Gammasphere spectrometer	50
4. Data analysis and results	55
4.1. Data processing and corrections	55
4.2. Angular distribution analysis	64
4.3. Coulex calculations	66
4.4. Results	70
4.4.1. ^{154}Sm	70
4.4.2. $^{194,196}\text{Pt}$	78
^{194}Pt analysis	78
^{196}Pt analysis	83
4.4.3. $^{130,132}\text{Ba}$	88
^{130}Ba analysis	88
^{132}Ba analysis	93
5. Discussion	97
5.1. Mixed-symmetry states of $^{130,132}\text{Ba}$	97
5.1.1. ^{130}Ba	98
5.1.2. ^{132}Ba	100
5.1.3. $2_{1,\text{ms}}^+$ states in the $A = 130$ mass region	102
5.2. Test of the $O(6)$ symmetry in $^{194,196}\text{Pt}$	108
5.2.1. ^{196}Pt	109
5.2.2. ^{194}Pt	111
5.3. Investigation of the β band of ^{154}Sm	116
6. Summary and Outlook	119

A. CLX Input file	121
B. Figures and Tables on the Analyses	123
B.1. ^{130}Ba experiment	123
B.2. ^{132}Ba experiment	128
B.3. ^{154}Sm experiment	133
B.4. ^{194}Pt experiment	140
B.5. ^{196}Pt experiment	148
Bibliography	157
List of Figures	167
List of Tables	169
Acronyms	171
Acknowledgements	173
Lebenslauf	175



1 Introduction

The atomic nucleus is a fascinating physical object. With a size measured in units of 10^{-15} m its dimensions are far beyond the abilities of human imagination. It is remarkable that an atomic nucleus only makes up about 0.001% of the volume of its atom leaving the rest empty. Yet, atomic nuclei comprise more than 99.9% of the mass of all visible matter. Our contemporary idea of the properties of the atomic nucleus can be traced back to its groundbreaking discovery together with the development of the model of the atom by Rutherford in 1911 [Rut11]. Since then, nuclear scientists have made tremendous progress in the description of the atomic nucleus. But even today not all properties of the atomic nucleus have been fully understood.

The atomic nucleus is a mesoscopic quantum system consisting of $\approx 1 - 300$ interacting nucleons of two different species, namely protons and neutrons. However, their interaction is still subject to ongoing investigations. Recent attempts to model realistic interactions try to deduce the interactions between the nucleons from the fundamentals of QCD, e.g. [Epe09], and involve different degrees of many-body terms. Given these considerations one would expect the structure of the nucleus to be chaotic and complicated. However, empirical data on level schemes, in particular of even-even nuclei all across the nuclear chart reveal a different observation. In fact, almost all even-even nuclei exhibit some surprisingly simple parts of their level schemes whose patterns are repeating in different regions of the nuclear chart. One well-known example are the first two excited states of even-even nuclei that in most cases are of angular momentum $J^\pi = 2^+$ and $J^\pi = 4^+$. The ratio of their excitation energies, $R_{4/2} = E(4_1^+)/E(2_1^+)$, exhibits a very uniform behavior as a function of the distance from the nuclear magic numbers. A plot of the values of $R_{4/2}$ across the nuclide chart is shown in Fig. 1.1.

While a unified description of nuclear structure is still not available, different approaches have been established to describe certain features of the nuclei. For nuclei near closed shells the nuclear shell model [Tal93] is capable of a good description, provided that the underlying single-particle energies and interactions are known. Nuclei further away of closed shells exhibit characteristic features that can be described by the phenomenon of quadrupole collectivity, which arises from a coherent motion of the nucleons, a phenomenon that can be observed in numerous even-even nuclei across the nuclear chart. A very successful theoretical framework for the description of collectivity has been found in the geometrical model

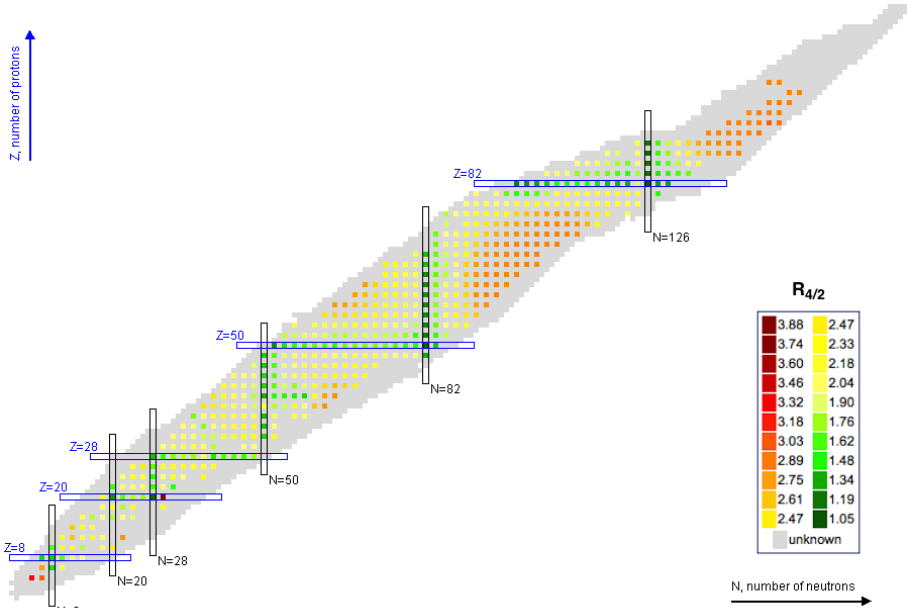


Figure 1.1.: Color-coded illustration of the ratio $R_{4/2} = E(4_1^+)/E(2_1^+)$ for the even-even nuclei across the entire nuclear chart [Nat14].

introduced by Bohr and Mottelson [Boh98], treating the nucleus as a shaped object which can be subject to excitations of vibrational and rotational character. A different ansatz was developed in terms of algebraic models, among which the Interacting Boson Model (IBM) [Iac87] is the most widely known. Short introductory chapters on all of the above-mentioned theoretical models will be given in the subsequent chapters.

The models which describe the different phenomena of quadrupole collectivity allow for the deduction of simple rules for experimental signatures – experimentally accessible quantities that are characteristic of the respective theoretical models and can, thus, help in guiding experimentalists to design and perform dedicated experiments. Experimental results on the quantities serving as signatures of given theoretical models are the most crucial testing ground for the applicability of a model. Such observables can be relative quantities like decay branching ratios or γ -ray multipole mixing ratios. However, absolute quantities, for example in the form of selection rules for electromagnetic transitions, allow for more substantial

interpretations of experimental data. In the past, the experimental identification of characteristic features of quadrupole collectivity has often been subject to either lengthy campaigns, investigating the same nucleus under different experimental probes and techniques to combine the results for conclusive information. Or, the observables for sufficient identification of predictions have not been available at all, and conclusions had to rely on relative quantities, only.

The recent technical developments in the field of experimental nuclear physics begin to change this picture. More powerful heavy ion accelerators have been developed [ATL14] that allow for the investigation of rare isotopes which are unfeasible to be prepared as targets. In addition, large arrays of semiconductor detectors have been designed that allow for highly efficient detection of electromagnetic radiation [Ebe08, Lee90].

One of the most suitable experimental techniques for the investigation of quadrupole collectivity is the electromagnetic excitation, or Coulomb excitation (Coulx), which has been used for this kind of research for almost 60 years now. Using this method in combination with contemporary accelerators and powerful HPGe detector arrays opens new possibilities in the field of nuclear structure research.

It is the purpose of this work to demonstrate the ability of this approach to address crucial aspects of nuclear quadrupole collectivity on an absolute scale within single experiments. In the course of this work, experiments focusing on the signatures of three different aspects of nuclear collectivity have been performed, namely experiments on the nuclei ^{154}Sm , $^{130,132}\text{Ba}$, and $^{194,196}\text{Pt}$. The nucleus ^{154}Sm is of rotational nature and the results of this work give new insights into the nature of its first excited $K = 0$ band. In the γ -soft nuclei $^{194,196}\text{Pt}$, the selection rules of the $O(6)$ dynamical symmetry of the Interacting Boson Model (IBM) have been compared to new experimental data. The results for the nuclei $^{130,132}\text{Ba}$ complete the experimental data on states with mixed proton-neutron symmetry in the $A = 130$ mass region. On the example of these nuclei, it will be shown in the present work, how the experimental technique works and is utilized. The data analysis will be explained in detail and the results will be presented.

The content of chapters 2 and 3 represents a compilation of knowledge from textbooks and prior publications by others. The author has no intention to claim these contents as his own ideas or his own work. These chapters are given to provide the reader with the theoretical background based on which the present experimental results have been interpreted. The personal contribution by the author is summarized in chapters 4 and 5, where the data analysis and the interpretation of the data are given.



2 Theoretical approaches to nuclear quadrupole collectivity

In this chapter, it is intended to briefly introduce some of the basic features of the models used for the discussion of the experiments performed in the course of this work with respect to nuclear collectivity.

In section 2.1 a brief overview on the description of nuclear structure in terms of single particles and their residual interactions is given. In principle, given the knowledge of the details of the interactions, this model should be able to produce the most exact results but becomes computationally challenging when it comes to the description of collectivity.

Those limitations can be overcome by the description of the nucleus in the framework of a geometrical object. The most relevant concepts of this approach will be shortly introduced in section 2.2. However, these models only describe limits not manifested in a large number of real nuclei. Yet, these limits are important cornerstones for the description of collective behavior in nuclei.

Section 2.3 deals with the Interacting Boson Model (IBM). It originates from a truncation of the nuclear shell model space and, yet, is capable of the description of collectivity of nuclei across the nuclear chart. One key feature of the IBM is its algebraic structure that distinguishes it from the models discussed before.

This chapter gives a brief introduction on some well-established theoretical models that are treated exhaustively in several textbooks. Unless otherwise stated this chapter is based on the respective parts of the textbooks of [Ber07], [Cas01a], [Kra87], and [May94].

2.1 Nuclear Shell Model

The nuclear shell model in its original form was introduced by Maria Goeppert-Mayer [Goe50] and Haxel, Jensen, and Suess [Hax49] independently. It was a great success, because it was capable of explaining the increased stability of nuclei consisting of the particular *magic numbers* of protons and neutrons: 2, 8, 20, 28, 50, 82, and 126.

The key idea behind this model is the independent motion of the nucleons under the influence of a central potential. Other than in atomic physics, this potential has no external source. Instead, the potential acting on the A -th nucleon is generated by the $A-1$ other nucleons. The Hamiltonian is modified by adding and subtracting a central potential $U(r)$

$$H = \underbrace{\sum_i \left[T_i(\mathbf{r}_i) + U(r_i) \right]}_{\equiv H_0} + \sum_{ij} V_{ij}(\mathbf{r}_i, \mathbf{r}_j) - \sum_i U(r_i) = H_0 + H_{\text{res}}, \quad (2.1)$$

shown here for simplicity on the example of free nucleon motion with two-body interactions. The contribution of the residual interaction H_{res} is assumed to be small. In first approximation it can be neglected, which is a good approximation for the derivation of the single particle orbits. However, H_{res} has important influence on the formation of nuclear structure, which will be discussed later. Because of the short-range character of the nucleon-nucleon interaction, the radial dependency of the potential $U(r)$ is chosen to be similar to the nuclear density $\rho(r)$, or even simpler, e.g. approximated by the Harmonic Oscillator (HO),

$$U(r) = \frac{1}{2} m \omega^2 r^2. \quad (2.2)$$

Although the HO shows the wrong asymptotic behavior, its shape for the region inside the nuclear volume is a good approximation and is valid for the study of bound states. By also taking a spin-orbit interaction V_{ls} into account

$$H_0 = \sum_i \left[T_i(\mathbf{r}_i) + \frac{1}{2} m \omega^2 r_i^2 \right] + V_{ls}(r) \mathbf{l} \cdot \mathbf{s}, \quad (2.3)$$

the solution of the Schrödinger equation yields the orbits that are shown qualitatively in Fig. 2.1. The orbits are labeled with the quantum numbers nl_j , where n is the radial quantum number, l is the orbital angular momentum, and j is the total angular momentum $j = l \pm 1/2$. The value of V_{ls} is chosen to be negative, resulting in the decrease of the energy of the orbitals with $j_> = l + 1/2$, while orbitals of $j_< = l - 1/2$ are raised. According to the Pauli principle each orbit can be populated by $2j + 1$ nucleons. Filling the orbits consecutively results in large energetic gaps for nucleon numbers that resemble the empirical magic numbers. It is obvious that this model is only a rough estimate. In fact, the sequence of the orbits as well as their energies are dependent on the region of the nuclear chart, and, not treated explicitly here, is different for protons and neutrons.

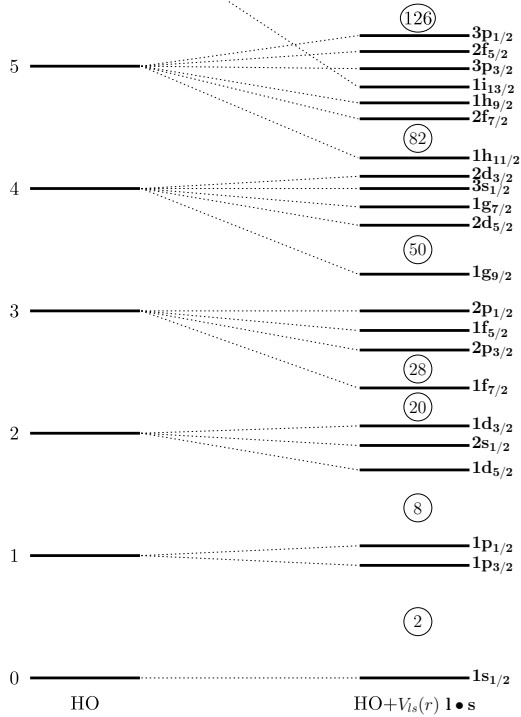


Figure 2.1.: Qualitative illustration of the orbits resulting from the shell model.

As a consequence of the Pauli principle, the $2j + 1$ nucleons of a completely filled orbit nl_j couple to a total angular momentum of $J = 0$. Therefore, the properties of the nuclear structure are determined by the nucleons in partially filled orbits, called *valence nucleons* and the residual interaction of V_{res} among them. Valence nucleons of the same kind in the same orbit nl_j can couple to different total angular momenta J , whose degeneracy is broken by the residual interaction between them. A figurative example of such an interaction is the δ interaction

$$V_{\text{res}} = -V_0 \delta(\mathbf{r}_1 - \mathbf{r}_2), \quad (2.4)$$

which models the short-range part of the nucleon-nucleon interaction. The δ interaction is maximal for two nucleons with maximum spatial overlap of their wave functions. This is the case for two antiparallely aligned nucleons with $M = m_1 + m_2 = 0$. As a consequence of the δ interaction the energy of configurations of nucleons coupled to angular momentum 0^+ are decreased the most,

followed by the $2^+, 4^+, \dots$ configurations, depending on which coupled angular momenta are allowed. Other models yield similar results, e.g. the pairing interaction. In general, configurations with a minimal number of nucleons not paired to $J = 0$, also referred to as configurations with minimal *seniority* ν , are favored by V_{res} . Thus, the shell model predicts that all even-even nuclei have a ground state with $J^\pi = 0^+$, which is also experimentally observed. As a consequence, some properties of even-odd nuclei can be predicted from the orbit of the last unpaired nucleon, e.g. the ground state spin and parity of the nucleus.

With an increasing number of valence nucleons, the long-range quadrupole part of the residual interactions become more and more important. This results in the formation of an increasingly deformed shape and in the formation of nuclear collectivity. At the same time the number of possible configurations increases rapidly and becomes computationally exhaustive. While the shell model can be expected to yield the most exact results (provided the information on single particle energies and interactions has been chosen correctly) the description of collective phenomena of atomic nuclei in its framework is hindered by overwhelmingly large model spaces. Therefore, different ansatzes have been developed to facilitate the theoretical description of nuclear collectivity. In the following sections, the most important approaches will be introduced, namely the geometrical model, which describes the nucleus as a shaped object of coherently behaving nucleons, and the Interacting Boson Model, which results from a truncation of the shell-model space to the physically most relevant configurations.

2.2 Vibrational and Rotational Nuclei

While the shell model offers a good description of nuclear structure for nuclei in close proximity to closed shells, a very figurative way for the description of certain phenomena observed in atomic nuclei is the geometrical model introduced by Bohr and Mottelson [Boh98]. Despite the very complex interplay of nucleons and forces present in the nucleus, a geometrical picture of the nucleus explains in a simple way the basic features of the collective behavior of certain nuclei away from closed shells, where the shell model descriptions become very complex and exhaustive in terms of computational power. The underlying idea is the assumption of the nucleus as a drop of a “liquid” of nucleons. It is mathematically described by a parametrization of its surface in terms of an expansion in spherical harmonics Y_λ^μ

$$R(\theta, \phi) = R_0 \left(1 + \sum_{\lambda=0}^{\infty} \sum_{\mu=-\lambda}^{\lambda} \alpha_{\lambda\mu} Y_\lambda^\mu(\theta, \phi) \right). \quad (2.5)$$

Nuclear excitations are described in this model by excitations of the shape of the surface. Near closed shells, this liquid takes a spherical shape and can be excited to perform oscillations around this equilibrium shape, while in mid-shell regions of the nuclear chart deformed shapes develop, which allow the nucleus to undergo rotational motion. The system can be described by the Bohr-Hamiltonian [Boh98, Cas01a], which is given as

$$H = -\frac{\hbar^2}{2m} \left[\frac{1}{\beta^4} \frac{\partial}{\partial \beta} \left[\beta^4 \frac{\partial}{\partial \beta} \right] + \frac{1}{\beta^2} \frac{1}{\sin 3\gamma} \frac{\partial}{\partial \gamma} \left[\sin 3\gamma \frac{\partial}{\partial \gamma} \right] \right] + \frac{\hbar^2}{2I} R^2 + V, \quad (2.6)$$

in which R is the rotational angular momentum and β and γ denote the shape variables. They will be explained in more detail with the model of the rotor in 2.2.2.

2.2.1 Vibrator

Nuclei near closed shells have a spherical shape. With increasing distance to the shell closures they behave increasingly collective and exhibit level schemes typical for vibrating nuclei. To describe a vibrating, spherical nucleus with equilibrium radius R_0 the description of its surface of (2.5) is regarded in its time-dependent form

$$R(\theta, \phi, t) = R_0 \left(1 + \sum_{\lambda=0}^{\infty} \sum_{\mu=-\lambda}^{\lambda} \alpha_{\lambda\mu}(t) Y_{\lambda}^{\mu}(\theta, \phi) \right). \quad (2.7)$$

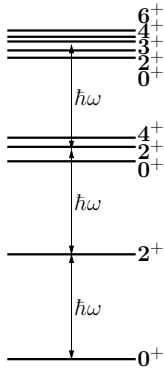
In the expansion the term of $\lambda = 0$ can be neglected because this term describes a nucleus that changes its volume while keeping its basic spherical shape. This so-called *breathing mode* occurs at large energies and can be neglected for the description of the low-lying collective states of the nucleus. The value of $\lambda = 1$ can also be neglected. It corresponds to a translation of the nucleus as a whole, which does not affect its internal structure. The higher lying values of $\lambda = 2, 3, \dots$ correspond to quadrupole, octupole, ... vibrations of the surface. In the following, the discussion will focus on quadrupole collectivity and, thus, the $\lambda = 2$ term of (2.7), neglecting minor contributions from the volume conservation condition. For $\lambda = 2$ the expansion coefficients $\alpha_{2\mu}$ are symmetric with respect to the value of μ , i.e.

$$\alpha_{2\mu} = \alpha_{2-\mu} \quad (2.8)$$

The Hamiltonian for the vibrator can be written as [Cas01a, p. 180]

$$H = \frac{1}{2} B \sum_{\mu} \left| \frac{d\alpha_{2\mu}}{dt} \right|^2 + \frac{1}{2} C \sum_{\mu} |\alpha_{2\mu}|^2. \quad (2.9)$$

a) Vibrator



b) Rotor

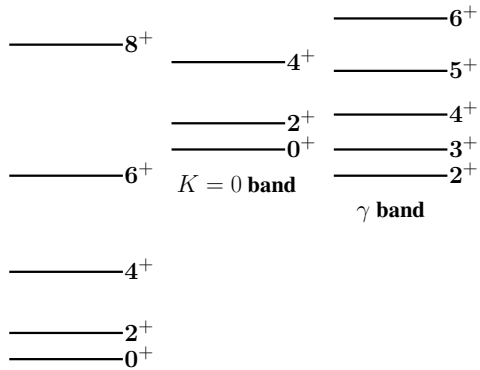


Figure 2.2.: Schematic low-lying level schemes of a) vibrating nuclei and b) rotating nuclei.

This Hamiltonian has the form of a Harmonic Oscillator with a frequency of

$$\omega = \frac{C}{B}. \quad (2.10)$$

Therefore, analog to excitations in solid state physics, excitations of a vibrating nucleus can be imagined as phonons with angular momentum λ and parity $(-1)^\lambda$, i.e. quadrupole phonons with positive parity $J^\pi = 2^+$ in the case of quadrupole excitations $\lambda = 2$.

The allowed angular momenta for the coupling of N phonons can be derived in the m -scheme. Since the quadrupole phonons have integer spin, they have to be treated like bosons, allowing for each combination of m states. This results in a triplet of $0^+, 2^+, 4^+$ states for two-phonon excitations and a quintuplet $0^+, 2^+, 3^+, 4^+, 6^+$ for three-phonon excitations. In practice the states of a multi-phonon excitation are not exactly degenerate, but exhibit multiplets of close-lying levels as depicted schematically in Fig. 2.2. In this picture, thus, the value of $R_{4/2} = E(2_1^+)/E(4_1^+)$ is expected to be $R_{4/2} = 2$, which in fact is observed in collective nuclei near closed shells.

In a simple notation vibrational N -phonon states can be written as

$$|N_{\text{ph}}\rangle = (\mathbf{b}^\dagger)^N |0\rangle, \quad (2.11)$$

with \mathbf{b}^\dagger being the quadrupole phonon creation operator. A destruction operator \mathbf{b} acting on a state $|N_{\text{ph}}\rangle$ leads to the expression

$$\mathbf{b}|N_{\text{ph}}\rangle = \sqrt{N_{\text{ph}}}|N_{\text{ph}} - 1\rangle. \quad (2.12)$$

From this expression it can be deduced that the $E2$ transition strength of an N -phonon state is proportional to N_{ph} . Thus, for a vibrating nucleus the ratio between the transition strengths of two-phonon and one-phonon states can be predicted, in particular the quantity $B_{4/2} = B(E2; 4_1^+ \rightarrow 2_1^+)/B(E2; 2_1^+ \rightarrow 0_1^+) = 2$ is predicted by the phonon model.

2.2.2 Rotor

With increasing distance to the closed shells, nuclei start to exhibit increasingly deformed shapes. In these regions of the nuclear chart, the residual interaction among the valence nuclei becomes more and more dominant and determines the nuclear properties. In particular the long-range component of the quadrupole part of the nucleon-nucleon interaction favors non-spherical configurations even in the nuclear ground state. The rotational picture of the atomic nucleus describes the nucleus in terms of a deformed object with moment of inertia I . Even without further specification of the underlying residual interactions this picture yields stunningly good descriptions of many phenomena observed in nuclei in mid-shell regions of the nuclear chart. Some basic ideas will be discussed in the following section.

The nuclear deformation can again be described by using the parametrization of the nuclear surface introduced in equation (2.5). Analog to the case of vibrational nuclei all terms but the quadrupole term of $\lambda = 2$ will be neglected in the following, since this term is most important for the description of low-lying collective state in atomic nuclei, again neglecting minor contributions from the volume conservation condition. The expression of (2.5), thus, reduces to

$$R(\theta, \phi) = R_0 \left(1 + \sum_{\mu=-2}^2 \alpha_{2\mu} Y_2^\mu(\theta, \phi) \right). \quad (2.13)$$

The intrinsic coordinate system can be chosen such that

$$\alpha_{20} \equiv \alpha_0, \quad \alpha_{21} = \alpha_{2-1} = 0, \quad \alpha_{22} = \alpha_{2-2} \equiv \alpha_2. \quad (2.14)$$

A commonly used notation for nuclear deformation are the deformation parameters β and γ , defined by

$$\alpha_0 = \beta \cos \gamma, \quad \alpha_2 = \frac{1}{\sqrt{2}} \beta \sin \gamma, \quad \text{with } \beta \geq 0. \quad (2.15)$$

In this notation, the value of β describes the *degree* of deformation. $\beta = 0$ corresponds to a spherical shape. The parameter γ describes the *triaxiality* of the deformed nucleus. For $\beta \neq 0$, $\gamma = 0$ corresponds to a axially deformed, prolate shape, i.e. the nucleus possesses a symmetry axis and is stretched along this axis like in the shape of an American Football. $\gamma = \pi/3$ corresponds to an oblate shape in which the nucleus is compressed along the symmetry axis, as for the shape of a discus. For values of $\gamma \neq n \cdot \pi/3$, the shape is triaxially deformed.

With the onset of nuclear deformation, also the charge distribution in the nucleus is no longer spherical. Consequently, a deformed nucleus exhibits a static quadrupole moment Q . It is connected to the deformation parameter β by the relation

$$Q_0 = \frac{3}{\sqrt{5}\pi} R_0^2 Z \beta (1 + 0.16\beta). \quad (2.16)$$

Here Q_0 represents the *intrinsic* quadrupole moment of the nucleus, which has to be distinguished from the experimentally observable *spectroscopic* quadrupole moment Q , which relates to Q_0 by

$$Q = \frac{3K^2 - J(J+1)}{(J+1)(2J+3)} Q_0, \quad (2.17)$$

where K denotes the projection of the total angular momentum J on the symmetry axis of the nucleus. It follows directly from (2.17) that for states with $J = 0$ (in particular for the nuclear ground state) the spectroscopic quadrupole moment vanishes. For the 2_1^+ state of the ground state band ($K = 0$), $Q = -2/7 Q_0$. The intrinsic quadrupole moment $Q_0(2_1^+)$ state is connected to the transition strength from the ground state by

$$B(E2; 0_1^+ \rightarrow 2_1^+) = \frac{5}{16\pi} e^2 Q_0^2(2_1^+). \quad (2.18)$$

The onset of deformation allows for rotational motion of the nucleus. The rotational energy of an even-even nucleus with ground state spin $J^\pi = 0^+$ can be written quantum mechanically

$$E_{\text{rot}} = \frac{\hbar^2}{2I} J(J+1), \quad (2.19)$$

with the moment of inertia I . Only even values of $J = 0, 2, 4, \dots$ can be found in a rotational band on top of a 0^+ ground state [Cas01a, p. 204]. From expression (2.19) it follows that for a rotational nucleus $E(2_1^+) = 6\hbar^2/2I$ and $E(4_1^+) = 20\hbar^2/2I$, and, consequently, $R_{4/2} = 3.33$. The characteristic $J(J + 1)$ dependence of the energies of states in rotational bands is in fact frequently observed for nuclei in mid-shell regions of the nuclear chart. A schematic example is depicted in Fig. 2.2.

Besides the possibility of rotations, also vibrational excitations of a deformed nucleus are possible. They usually appear in the level scheme as band heads of rotational bands corresponding to superpositions of vibrational and rotational excitations. The vibrational excitations do not always exhibit $J = 0$. Therefore, (2.19) has to be generalized to

$$E_{\text{rot}} = \frac{\hbar^2}{2I} [J(J + 1) - K(K + 1)] . \quad (2.20)$$

Again, this results in rotational bands analog to the ground state ($K = 0$) band. However, for rotational bands on top of $K \neq 0$ states even as well as odd angular momenta $J = K, K + 1, K + 2, \dots$ are allowed [Cas01a, p. 205f.]. In the low-lying level schemes of many nuclei, in particular two rotational bands based on top of a 0^+ and a 2^+ state are frequently observed. The band on top of the 2^+ state is connected with the vibrational excitation of the nucleus as a function of the deformation parameter γ and is therefore usually referred to as the γ band of the nucleus. The rotational band on top of the 0^+ state had originally been assigned analogously, i.e. as the vibration in terms of the deformation parameter β . However, this assignment is still object to vivid discussions and will be further addressed within this work in the discussion of the experiment on ^{154}Sm in the framework of the confined- β -soft rotor model (CBS) (cf. 2.4.3 and 5.3).

The character of the states in rotational bands as a superposition of a rotation and an excitation (regardless of its nature) allows for the prediction of ratios of transition strengths of two transitions that have the same initial band and the same final band. The transition matrix elements can be separated into a *rotational* part and a *structural* part. The latter is the same for all states within the same rotational band and will, therefore, cancel out in a ratio. The result is a ratio usually referred to as the *Alaga rule* [Ala55] that is solely dependent on squares of Clebsch-Gordan coefficients

$$\frac{B(E2; J_i \rightarrow J_f)}{B(E2; J_i \rightarrow J'_f)} = \frac{\langle J_i K_i 2 \Delta K | J_f K_f \rangle^2}{\langle J_i K_i 2 \Delta K | J'_f K'_f \rangle^2} , \quad (2.21)$$

a) γ -soft

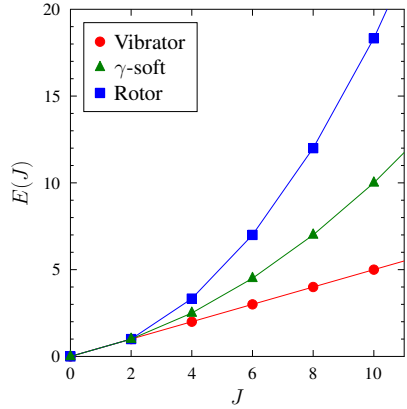
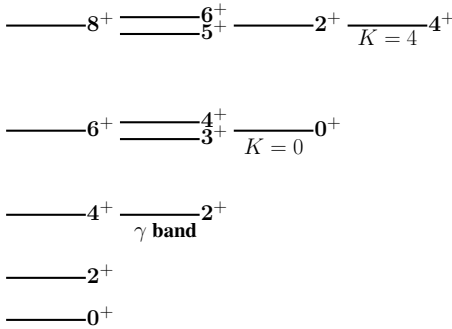


Figure 2.3.: Left: Schematic level scheme of a γ -soft nucleus. Right: Relative energies of the levels in the ground state band of vibrators, rotors, and γ -soft nuclei.

with angular momentum J and its projection K of states in two rotational bands indicated by indices i and f . The expressions in angle brackets denote Clebsch-Gordan coefficients for angular momentum coupling.

2.2.3 γ -soft nuclei

The third cornerstone of the phase diagram of nuclear structure (Fig. 2.4) is the class of γ -soft nuclei introduced by Wilets and Jean in 1956 [Wil56]. As the name suggests, it is characterized by a deformed nucleus whose potential has been chosen to be independent of the deformation parameter γ . (It has become customary to refer to this model by the term γ soft, although the meaning of γ -softness is more general than of γ independence.) The level scheme of such a nucleus exhibits certain characteristic features. A schematic illustration of the level scheme of a γ -soft nucleus is shown in Fig. 2.3(a). The levels are labeled by the quantum number Λ . The excitation energies of the Yrast states follow the relation $E \propto \Lambda(\Lambda + 3)$, and with $J = 2\Lambda$, it follows that

$$E \propto J(J + 6), \quad (2.22)$$

and, thus, the energies $E(J)$ of the Yrast states do not increase as rapidly with angular momentum J as in the rotational case, yet faster than for vibrational nuclei, cf. Fig. 2.3(b). Consequently, the $R_{4/2}$ ratio in γ -soft nuclei is $R_{4/2} = 2.5$.

For $\Lambda = 2$, there are two degenerate states with angular momentum 2^+ and 4^+ , but, unlike in the vibrational case, no 0^+ state.

The quasi- γ band of a γ -soft nucleus exhibits a characteristic energy staggering, i.e. the states of this band do not follow the relation of (2.22). Instead, odd-spin and the respective consecutive even-spin states are (nearly) degenerate, e.g. the 3^+ and 4^+ states.

The model of γ -softness is closely related to the $O(6)$ dynamical symmetry of the Interacting Boson Model (cf. section 2.3.2), which will be dealt with in the discussion of the results of the $^{194,196}\text{Pt}$ experiments in 5.2.

2.3 Interacting Boson Model

In the preceding sections 2.1 and 2.2, two different approaches to the description of nuclear structure have been introduced with the shell model and the geometrical model. The Interacting Boson Model (IBM) can be seen as an intermediate way between the two. It originates from a truncation of the shell model space and, yet, is capable of the description of collective phenomena of different kinds. Moreover, the IBM can be used to describe nuclei all over the phase diagram of Fig. 2.4.

In the following section 2.3.1 the main features of the IBM will be introduced. In 2.3.2 the analytically solvable limits of the IBM will be discussed. The model will be extended to also include the proton-neutron degree of freedom in 2.3.3.

Literature on the IBM exists in abundance. The following discussions are based to a large extent on the textbook of Iachello and Arima [Iac87] and on a review article by Casten and Warner [Cas88].

2.3.1 Basics

The IBM has been introduced by Iachello and Arima [Iac87]. It is based on the idea of a pairwise coupling of two nucleons that are then treated as a boson. The number of bosons for a given nucleus is $N = 1/2 (N_\pi + N_\nu)$, where N_π and N_ν are the numbers of valence protons and neutrons. Any contributions from the doubly-magic core of the nucleus are neglected. Apparently, N is conserved for a given nucleus. N is always counted as the closest distance to the closed shell treating particles and holes alike. In the simplest version of the IBM-1 no distinction is made between protons and neutrons. (The proton-neutron version of the IBM, the IBM-2, will be discussed in 2.3.3.)

In the sd-IBM-1 each boson can only carry an angular momentum of $L = 0$ (s boson) or $L = 2$ (d boson)¹. In this respect the IBM can be seen as a truncation of the nuclear shell model to configurations of $J = 0, 2$. The bosons can be treated mathematically in terms of creation and destruction operators

$$s^\dagger, s, \quad \text{and} \quad d_\mu^\dagger, \tilde{d}_\mu, \quad (2.23)$$

respectively, with $\mu = -2 \dots 2$. The operator \tilde{d}_μ is defined as

$$\tilde{d}_\mu = (-1)^\mu d_{-\mu} \quad (2.24)$$

in order to have the properties of a spherical tensor. For these operators the commutation relations

$$\begin{aligned} [s, s^\dagger] &= 1, & [s, s] &= [s^\dagger, s^\dagger] = 0, \\ [d_\mu, d_{\mu'}^\dagger] &= \delta_{\mu\mu'}, & [d_\mu, d_{\mu'}] &= [d_\mu^\dagger, d_{\mu'}^\dagger] = 0, \\ [s, d_\mu^\dagger] &= [s, d_\mu] = [s^\dagger, d_\mu^\dagger] &= [s^\dagger, d_\mu] = 0, \end{aligned} \quad (2.25)$$

apply.

The most general Hamiltonian for the treatment of excited states can be written as

$$\begin{aligned} H &= \varepsilon' \hat{n}_d + \frac{1}{2} \sum_L C'_L (d^\dagger d^\dagger)^{(L)} \cdot (\tilde{d}\tilde{d})^{(L)} \\ &+ \frac{\nu_2}{\sqrt{10}} [(d^\dagger d^\dagger)^{(2)} \cdot \tilde{d}s + H.c.] \\ &+ \frac{\nu_0}{2\sqrt{5}} (d^{\dagger 2} s^2 + H.c.), \end{aligned} \quad (2.26)$$

with the d boson-number operator $\hat{n}_d = d^\dagger \tilde{d}$. Oftentimes the Hamiltonian is used in its multipole form

$$H = \varepsilon'' \hat{n}_d + a_0 P^\dagger P + a_1 \hat{L}^2 + a_2 Q^2 + a_3 T_3^2 + a_4 T_4^2, \quad (2.27)$$

¹ In the framework of the Interacting Boson Model the angular-momentum quantum number is usually denoted by L . The present work will stick to this habit.

in which

$$\begin{aligned}
 P &= \frac{1}{2} (\tilde{d}^2 - s^2) , \\
 T_l &= (d^\dagger \tilde{d})^{(l)} , \quad l = 0, 1, 2, 3, 4 , \\
 Q &= (d^\dagger s + s^\dagger \tilde{d}) - \frac{\sqrt{7}}{2} T_2 = (d^\dagger s + s^\dagger \tilde{d}) - \frac{\sqrt{7}}{2} (d^\dagger \tilde{d})^{(2)} , \\
 \hat{n}_d &= \sqrt{5} T_0 , \\
 \hat{L} &= \sqrt{10} T_1 .
 \end{aligned}$$

As a basis for IBM calculations mostly the states of the U(5) dynamical symmetry are chosen (see sec. 2.3.2 below). In this basis the states can be labeled according to the quantum numbers

$$|N n_d \nu n_\Delta L \rangle , \quad (2.28)$$

where N denotes the total boson number, n_d the number of d bosons, ν denotes d -boson seniority, n_Δ denotes the number of d -boson triplets coupled to 0, and L denotes the angular momentum.

The $E2$ transition operator is defined by

$$T(E2) = e_B ((d^\dagger s + s^\dagger \tilde{d}) + \chi [d^\dagger \tilde{d}]^{(2)}) . \quad (2.29)$$

It has the same form as the Q operator of Eq. 2.27 except for the parameter χ . In the framework of the *consistent-Q formalism* [War83] the factor of $\sqrt{7}/2$ in the operator Q is replaced by χ and is kept equal for the operators Q^χ and $T(E2)$.

2.3.2 The dynamical symmetries of the IBA

One of the main characteristic features of the IBM is its algebraic structure. This will be briefly summarized in the following.

The five components of the d boson and the s boson span a six-dimensional space. Under the constraint of total boson number conservation, 36 different bilinear combinations of two-body operators are possible, namely

$$s^\dagger s \quad s^\dagger \tilde{d}_\mu \quad d_{\mu}^\dagger, s \quad (d^\dagger, \tilde{d})_\mu^{(l)} , \quad (2.30)$$

with $l = 0, 1, 2, 3, 4$ and $\mu = 4, 3, \dots, -4$, $|\mu| \leq l$. It can be shown that these operators *close on commutation*, i.e. each commutator of pair of these operators results in a linear combination of the operators of (2.30) (or vanishes). Therefore, these operators are *generators* of the Lie Algebra $U(6)$. Among the set of (2.30), several subgroups can be found that themselves close on commutation, and thus, are generators of a sub algebra of $U(6)$. Under the physical constraint that a decomposition of $U(6)$ has to include the rotational algebra $O(3)$, three chains of decompositions are possible:

$$U(6) \supset U(5) \supset O(5) \supset O(3) \supset O(2), \quad (2.31a)$$

$$U(6) \supset SU(3) \supset O(3) \supset O(2), \quad (2.31b)$$

$$U(6) \supset O(6) \supset O(5) \supset O(3) \supset O(2). \quad (2.31c)$$

For each of the groups in the decompositions of (2.31) operators exist that commute with all the generators of the group. These are called *Casimir operators*. A Hamiltonian consisting of Casimir operators is diagonal and its eigenvalues can be written by a sum of the eigenvalues of the Casimir operators. These eigenvalues are unique for a group and referred to as *irreducible representation*. For the $U(6)$ algebra of the IBM, the irreducible representation is the total number of bosons, N . Each step of decomposition into a new subgroup introduces a new irreducible representation that breaks the degeneracy of the eigenvalues of the Casimir operator of the preceding group. This situation of a Hamiltonian consisting of Casimir operators of a chain of subalgebras is called a *dynamical symmetry*. The three types of dynamical symmetries of (2.31) are the cornerstones of the phase diagram of the IBM, which is shown in Fig. 2.4.

Within the IBM also the description of the rest of the diagram between the dynamical symmetries is possible, e.g. by the use of the simplified Hamiltonian [Cas06]

$$H = \varepsilon \hat{n}_d + \kappa Q^\chi Q^\chi = c \left((1 - \zeta) \hat{n}_d - \frac{\zeta}{4N} Q^\chi Q^\chi \right), \quad (2.32)$$

where c is used as a normalization factor. The triangle of Fig. 2.4 can be spanned by a variation of the parameters ζ and χ between the limits

$$\begin{aligned} 0 &\leq \zeta \leq 1, \\ -1.32 &\leq \chi \leq 0. \end{aligned}$$

In the consistent- Q formalism the value of χ is kept equal for the Q operator and for the transition operator $T(E2)$. The values of $\zeta = 0$ corresponds to the $U(5)$ limit.

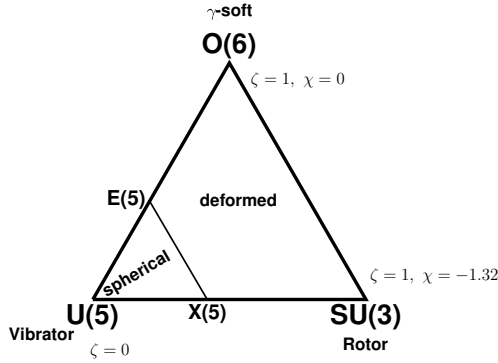


Figure 2.4.: Symmetry triangle of the IBM. The dynamical symmetries are the cornerstones of phase diagram of the IBM. Using the Hamiltonian of the consistent- Q formalism of (2.32) the whole triangle can be described in the IBM by varying the parameters ζ and χ . The points E(5) and X(5) denote the shape phase-transitional points, cf. sections 2.4.1 and 2.4.2.

By a change in ζ different positions inside the triangle can be described, until for $\zeta = 1$ the opposite leg of the triangle is reached. The position between the O(6) limit and the SU(3) limit can be chosen by a variation of χ .

U(5)

The U(5) dynamical symmetry [Ari76] is based on the subchain decomposition of the U(6) algebra of (2.31a). The corresponding quantum numbers of the irreducible representations are

$$\begin{array}{cccccc} \text{U}(6) & \supset & \text{U}(5) & \supset & \text{O}(5) & \supset & \text{O}(3) & \supset & \text{O}(2) \\ [N] & & n_d & & \nu, \tilde{n}_\Delta & & L & & M_L \end{array} \quad (2.33)$$

In terms of the multipole form of (2.27) the Hamiltonian for the U(5) symmetry is given as

$$H = \varepsilon \hat{n}_d + a_1 \hat{L}^2 + a_3 T_3^2 + a_4 T_4^2. \quad (2.34)$$

For the simplest case of $H = \varepsilon \hat{n}_d$, the resulting spectrum resembles that of a vibrating nucleus, in which levels with the same number of phonons n_d are degenerate. The additional terms in (2.34) break these degeneracies. Therefore

the U(5) limit is also capable of the description of anharmonic vibrators, i.e. $R_{4/2}(U(5)) \in [2.0 \dots 3.33]$. For a characterization of a nucleus in terms of the U(5) symmetry it is therefore important also to consider the $B(E2)$ values.

For the U(5) symmetry often only the first term of the $E2$ transition operator of (2.29) is used,

$$T(E2) = e_B((d^\dagger s + s^\dagger \tilde{d})) . \quad (2.35)$$

Using this operator $E2$ transitions are allowed for $\Delta n_d = \pm 1$, which is analog to the phonon picture of vibrational nuclei [Cas88]. This selection rule is the key signature for the experimental assignment of U(5) symmetry to a given nucleus.

In the U(5) dynamical symmetry the IBM makes parameter-free predictions on ratios of transition strengths, which can serve as important benchmarks for the comparison of experimental results with the predictions of the model. Those predictions include the ratios [Iac87]

$$\begin{aligned} & \frac{B(E2; 4_1^+ \rightarrow 2_1^+)}{B(E2; 2_1^+ \rightarrow 0_1^+)} \\ &= \frac{B(E2; 2_2^+ \rightarrow 2_1^+)}{B(E2; 2_1^+ \rightarrow 0_1^+)} \\ &= \frac{B(E2; 0_2^+ \rightarrow 2_1^+)}{B(E2; 2_1^+ \rightarrow 0_1^+)} = 2 \frac{N-1}{N} \xrightarrow{N \rightarrow \infty} 2 , \end{aligned} \quad (2.36)$$

where N denotes the total boson number of the nucleus. The predictions for the limit $N \rightarrow \infty$ are equal to the predictions of the simple vibrator model.

SU(3)

The SU(3) dynamical symmetry [Ari78a] is based on the subchain decomposition of the U(6) algebra of (2.31b). The corresponding quantum numbers of the irreducible representations are

$$\begin{array}{ccccccc} U(6) & \supset & SU(3) & \supset & O(3) & \supset & O(2) \\ [N] & & (\lambda, \mu), \tilde{\chi} & & L & & M_L . \end{array} \quad (2.37)$$

The Hamiltonian for this symmetry limit takes the form

$$H = a_1 \hat{L}^2 + a_2 Q^2 . \quad (2.38)$$

The resulting level scheme can be classified in terms of the quantum numbers λ and μ . (In the transition from SU(3) to its subgroup the additional quantum number K' has to be introduced.) The level scheme for the three lowest lying bands described by the quantum number pairs $(\lambda, \mu) = (2n, 0)$ and $(\lambda, \mu) = (2n - 4, 2)$ exhibits bands that can be identified in the geometrical picture as the rotational ground-state band, the $K = 0$ band, and the γ band. Unlike in the geometrical picture, however, the levels with even angular momentum in the $K = 0$ and the γ bands are degenerate in SU(3). In this respect the SU(3) limit of the IBM describes a special class of rotational nuclei.

In SU(3), the $E2$ transition operator of (2.29) is used. It forbids transitions that connect different representations of (λ, μ) , e.g. transition from the γ to the ground-state band. However, transitions between the β and γ bands are allowed, since they belong to the same representation, which is in contrast to the geometrical picture [Cas88].

The predictions of ratios of transition strengths between the lowest-lying states in the SU(3) limit are given as [Iac87]

$$\frac{B(E2; 4_1^+ \rightarrow 2_1^+)}{B(E2; 2_1^+ \rightarrow 0_1^+)} = \frac{10(N-1)(2N+5)}{7N(2N+3)} \xrightarrow{N \rightarrow \infty} \frac{10}{7}, \quad (2.39a)$$

$$\frac{B(E2; 2_2^+ \rightarrow 2_1^+)}{B(E2; 2_1^+ \rightarrow 0_1^+)} = 0, \quad (2.39b)$$

$$\frac{B(E2; 0_2^+ \rightarrow 2_1^+)}{B(E2; 2_1^+ \rightarrow 0_1^+)} = 0, \quad (2.39c)$$

where N denotes the total boson number of the nucleus.

O(6)

The O(6) dynamical symmetry [Ari78b] is based on the subchain decomposition of the U(6) algebra of (2.31c). The corresponding quantum numbers of the irreducible representations are

$$\begin{array}{ccccccc} \text{U}(6) & \supset & \text{O}(6) & \supset & \text{O}(5) & \supset & \text{O}(3) & \supset & \text{O}(2) \\ [N] & & \sigma & & \tau, \tilde{\nu}_\Delta & & L & & M_L. \end{array} \quad (2.40)$$

The Hamiltonian is given by

$$H = a_0 P^\dagger P + a_1 \hat{L}^2 + a_3 T_3^2. \quad (2.41)$$

The $E2$ transition operator is given by

$$T(E2) = e_B ((d^\dagger s + s^\dagger \tilde{d})) . \quad (2.43)$$

The selection rules for $E2$ transitions that follow from (2.43) are [Cas88]

$$\Delta\sigma = 0 , \quad (2.44a)$$

$$\Delta\tau = \pm 1 . \quad (2.44b)$$

These selection rules are the key signatures for the assignment of $O(6)$ symmetry to a nucleus based on experimental data on $E2$ transition strengths. (With the choice of the most general $E2$ transition operator $T(E2) = e_B ((d^\dagger s + s^\dagger \tilde{d}) + \chi [d^\dagger \tilde{d}]^{(2)})$ of (2.29) also transitions with $\Delta\tau = 0, \pm 2$ and $\Delta\sigma = \pm 2$ can be generated [Isa87].)

The predictions of ratios of transition strengths between the lowest-lying states in the $O(6)$ limit are given as [Iac87]

$$\frac{B(E2; 4_1^+ \rightarrow 2_1^+)}{B(E2; 2_1^+ \rightarrow 0_1^+)} = \frac{10(N-1)(N+5)}{7N(N+4)} \xrightarrow{N \rightarrow \infty} \frac{10}{7} , \quad (2.45a)$$

$$\frac{B(E2; 2_2^+ \rightarrow 2_1^+)}{B(E2; 2_1^+ \rightarrow 0_1^+)} = \frac{10(N-1)(N+5)}{7N(N+4)} \xrightarrow{N \rightarrow \infty} \frac{10}{7} , \quad (2.45b)$$

$$\frac{B(E2; 0_2^+ \rightarrow 2_1^+)}{B(E2; 2_1^+ \rightarrow 0_1^+)} = 0 , \quad (2.45c)$$

where N denotes the total boson number of the nucleus.

2.3.3 The pn version of the Interacting Boson Model, IBM-2

In the preceding sections the IBM has been introduced in its most simple version where no distinction between protons and neutrons is made. The Interacting Boson Model 2 (IBM-2) has been introduced [Ari77, Iac87, Ots78] as an extension of the aforementioned IBM-1 allowing for the treatment of the proton-neutron degree of freedom. In particular the IBM-2 is capable of the description of states with a mixed proton-neutron symmetry. The main features of the model and the properties and signatures of mixed-symmetry states are introduced in the following.

The creation and destruction operators are defined individually for protons and neutrons as

$$s_\rho^\dagger , \quad d_{\rho,\mu}^\dagger \quad \text{and} \quad s_\rho , \quad \tilde{d}_{\rho,\mu} , \quad (2.46)$$

with $\rho = \pi, \nu$ and $\mu = 2, 1, \dots, -2$. The Hamiltonian contains individual proton and neutron terms and additional proton-neutron boson interaction terms are introduced. In this respect the analog of the Hamiltonian in the consistent- Q formalism of Eq. (2.32) can be written as

$$H = \varepsilon_\pi \hat{n}_{d_\pi} + \varepsilon_\nu \hat{n}_{d_\nu} + \kappa_{\pi\pi} Q_\pi^{\chi_\pi} \cdot Q_\pi^{\chi_\pi} + \kappa_{\nu\nu} Q_\nu^{\chi_\nu} \cdot Q_\nu^{\chi_\nu} + 2\kappa_{\pi\nu} Q_\pi^{\chi_\pi} \cdot Q_\nu^{\chi_\nu} + \hat{M}(\xi_1, \xi_2, \xi_3), \quad (2.47)$$

where the \hat{n}_{d_ρ} are the d -boson number operators for protons and neutrons with the respective d -boson energies ε_ρ . The $Q_\rho^{\chi_\rho}$ denote the quadrupole operator for proton-bosons and neutron-bosons. The last term of (2.47) denotes the so-called Majorana interaction and is defined as

$$\hat{M}(\xi_1, \xi_2, \xi_3) = \frac{1}{2} \xi_2 (s_\pi^\dagger d_\nu^\dagger - d_\pi^\dagger s_\nu^\dagger) \cdot (s_\pi \tilde{d}_\nu - \tilde{d}_\pi s_\nu) - \sum_{K=1,3} \xi_K \left([d_\pi^\dagger d_\nu^\dagger]^{(K)} \cdot [\tilde{d}_\pi \tilde{d}_\nu]^{(K)} \right). \quad (2.48)$$

F-spin and mixed symmetric states

For a formal distinction of proton and neutron bosons the F -spin quantum number has been introduced [Ari77]. The concept of F -spin [Isa86] is formally equivalent to the isospin formalism but is applied to proton and neutron bosons instead of nucleons. Therefore, proton (neutron) bosons are assigned an F -spin of $F = 1/2$ with projection quantum numbers $F_z = +1/2$ ($F_z = -1/2$). The value of F_z for a nucleus is, thus,

$$F_z = \left(+\frac{1}{2} \right) N_\pi + \left(-\frac{1}{2} \right) N_\nu = \frac{1}{2} (N_\pi - N_\nu), \quad (2.49)$$

with the proton and neutron boson numbers N_π and N_ν , respectively. The maximal value F can take is

$$F_{\max} = \frac{1}{2} (N_\pi + N_\nu). \quad (2.50)$$

States described in the IBM-2 can be quantified by their F -spin quantum number which is a measure of the symmetry of the wave function with respect to the exchange of proton and neutron labels. States that have an F -spin of $F = F_{\max}$ are

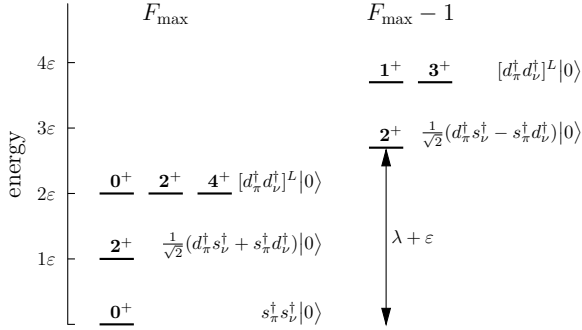


Figure 2.6.: Illustration of the low-lying level scheme of the simplified IBM-2 Hamiltonian $H = \varepsilon \hat{n}_d + \lambda \hat{M}$ of (2.51) for $N_\pi = N_\nu = 1$. The Majorana operator \hat{M} only affects the states with $F = F_{\max} - 1$. Figure adapted from [Pie08].

unchanged under this exchange and are referred to as *fully symmetric states* (FSS). The solutions from the IBM-1 of 2.3.1 can be identified as the solutions from the IBM-2 with $F = F_{\max}$ F -spin values. States with $F = F_{\max} - 1$ are not symmetric under the exchange of proton and neutron labels and are called *mixed symmetric states* (MSS). In the Hamiltonian of (2.47) the Majorana interaction (2.48) is sensitive to states with $F = F_{\max} - 1$ only. These states reside at excitation energies higher than the FS states. A schematic drawing is shown in Fig. 2.6 using the simplified Hamiltonian

$$H = \varepsilon \hat{n}_d + \lambda \hat{M}, \quad (2.51)$$

for a vibrator nucleus with $N_\pi = N_\nu = 1$, where $\varepsilon = \varepsilon_\pi = \varepsilon_\nu$. Besides the vibrator-like levels for the $F = F_{\max}$ states, the $F = F_{\max} - 1$ states reside at higher energies and are sensitive on the Majorana part of the Hamiltonian of (2.51). For vibrating nuclei near closed-shells, the MS state lowest in energy is the mixed symmetric $2_{1,ms}^+$ state. Its wave function contains the same terms as the fully symmetric 2_1^+ state, but is antisymmetric under the exchange of proton and neutron labels. (For more complex cases with $N_\pi, N_\nu > 1$ the complete antisymmetry of the wave function dissolves in favor of what is usually called *mixed symmetry*.) For rotational nuclei the lowest state of mixed symmetry is the well-known 1^+ scissors mode, which was first experimentally observed at the DALINAC in Darmstadt [Boh84].

A detailed review on the $2_{1,ms}^+$ excitation has been published by Pietralla *et al.* [Pie08].

Q-Phonon Scheme

A very figurative way for the description of mixed-symmetric states is provided in the framework of the Q-phonon picture [Ots94, Sie94]. It is based on the idea of describing the nuclear states by phonon excitations, but unlike in the picture of vibrational nuclei the phonons in the Q-phonon scheme do not act on the phonon vacuum. Instead, an excitation of angular momentum L can be described by the repeated action of the quadrupole phonon operator Q on the correlated ground state of the nucleus $[Q \dots Q]^{(L)}|0_1^+\rangle$. The validity of this picture has been shown empirically [Pie94] by an evaluation of the ratio

$$R^{(2)} = \frac{\sum_{i>1} B(E2; 0_1^+ \rightarrow 2_i^+)}{\sum_{i\geq 1} B(E2; 0_1^+ \rightarrow 2_i^+)} \quad (2.52)$$

for all collective nuclei from $Z = 30$ to $Z = 82$. It was shown that for all collective nuclei the value of $R^{(2)} \leq 10\%$, i.e. that the 2_1^+ states of all collective nuclei can indeed be described by a quadruple phonon excitation of the nuclear ground state. An analog evaluation of the odd-spin states in collective nuclei [Pie95] has come to similar results.

The Q-phonon scheme can be used to describe the low-lying level scheme of Fig. 2.6 by the coupling of symmetric and mixed-symmetric Q phonons, e.g.

$$\begin{aligned} |2_1^+\rangle &= Q_s|0_1^+\rangle & |2_{ms}^+\rangle &= Q_m|0_1^+\rangle \\ |4_1^+\rangle &= [Q_s Q_s]^{(4)}|0_1^+\rangle & |1_{ms}^+\rangle &= [Q_s Q_m]^{(1)}|0_1^+\rangle \\ & & |3_{ms}^+\rangle &= [Q_s Q_m]^{(3)}|0_1^+\rangle. \end{aligned} \quad (2.53)$$

The expressions of (2.53) are given without normalization factors. In these relations, $Q_s = Q_\pi + Q_\nu$ and $Q_m = Q_\pi/N_\pi - Q_\nu/N_\nu$ denote symmetric and mixed-symmetric quadrupole operators. The representation of (2.53) reveals the importance of the $2_{1,ms}^+$ state as building block of nuclear collectivity, since the two-phonon mixed-symmetric states, 1_{ms}^+ and 3_{ms}^+ , are generated by the coupling of a mixed-symmetric phonon with a symmetric phonon.

Signatures of mixed-symmetric states

Mixed-symmetric states are of isovector character. Their $E2$ decay to the corresponding fully-symmetric states is forbidden. Instead, strong $M1$ decays are expected to connect these states. In the case of the $2_{1,ms}^+$ state, a transition with

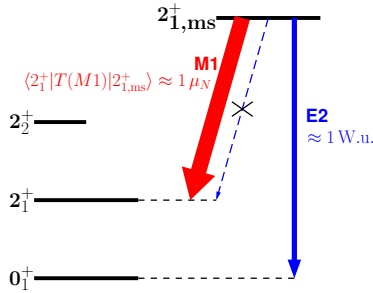


Figure 2.7.: The unique decay signature of mixed-symmetric states is a predominant $M1$ decay to the corresponding fully-symmetric state.

a matrix element of $\langle 2_1^+ | T(M1) | 2_{1,ms}^+ \rangle \approx 1 \mu_N$ is expected. At the same time the $E2$ transition to the ground-state can be expected to be weakly collective with a strength of the order of $\approx 1 \text{ W.u.}$. These transition strengths result in a very short lifetime of the $2_{1,ms}^+$ state of the order of $\tau(2_{1,ms}^+) \approx 100 \text{ fs}$. A schematic illustration of the $E2$ and $M1$ decays [Pie98b] of mixed-symmetric states is shown in Fig. 2.7. The best-investigated nucleus in this respect is the nucleus ^{94}Mo [Pie99, Pie00, Fra01, Fra03]. In this nucleus the one and two-phonon mixed-symmetric states have been identified on the basis of these signature transitions.

2.4 Transitional Nuclei

The model descriptions of vibrators, rotors, and γ -soft nuclei discussed above are important cornerstones for the understanding of nuclear collectivity. Most real nuclei, however, are usually situated in between these ideal cases. It is therefore necessary to study the shape transitions that occur on the paths between these limits. In this respect, the shape transitions along the legs of the symmetry triangle of nuclear collectivity have been investigated thoroughly. The transition on the path from $U(5)$ to $O(6)$ has been identified as a second-order phase transition and the transition between $U(5)$ and $SU(3)$ as a first-order phase transition [Die80]. For these points analytical solutions have been found which will be introduced in the following chapters, namely the transitional points of $E(5)$ in 2.4.1 and $X(5)$ in 2.4.2. (It shall be noted that despite the similarity in the nomenclature of the phase shape transitional points to the dynamic symmetries of the IBM the $E(5)$ and $X(5)$ solutions are not situated within the IBM framework.) As a generalization of the

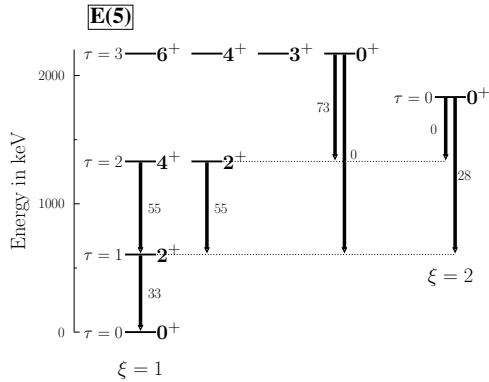


Figure 2.8.: Level scheme of the E(5) shape phase transitional point between the U(5) and O(6) dynamical symmetries of the IBM compared to the level scheme of ^{134}Ba . Figure adapted from [Iac00] and [Cas00].

solution of the X(5) shape phase-transitional point, the confined- β -soft rotor model has been introduced to describe nuclei on the transition from X(5) to SU(3). It will be discussed in 2.4.3.

2.4.1 E(5)

For the transitional point on the path from U(5) to O(6) a solution in terms of a dynamical symmetry has been given by Iachello [Iac00]. The main assumption is a potential with no dependence on the shape parameter γ and an infinite square well potential in the shape parameter β , for which the solution of the Bohr-Hamiltonian of (2.6) can be given in Bessel functions. The eigenvalues of the problem are then functions of the zeros of the Bessel functions. The resulting level scheme can be described in terms of quantum numbers ξ , τ , and L . A level scheme is depicted in Fig. 2.8. The solution yields fixed ratios of observables, e.g. $R_{4/2} = 2.20$. Compared to the dynamical symmetries of the subgroup decompositions of (2.31) the character of a dynamical symmetry arises from the class of zeros of the Bessel functions of the Hamilton operator.

As an empirical realization of the E(5) symmetry the nucleus ^{134}Ba [Cas00] has been suggested, cf. Fig. 2.8.

2.4.2 X(5)

X(5) denotes the critical point in the shape phase transition on the path from U(5) to SU(3), cf. Fig. 2.4. A solution of the Bohr Hamiltonian of (2.6) for this point has been suggested by Iachello [Iac01]. The ansatz is a separable potential of the form $V(\beta, \gamma) = v(\beta) + u(\gamma)$, where $v(\beta)$ is chosen as a square well potential in the deformation parameter β ,

$$v(\beta) = \begin{cases} = 0 & \text{for } \beta \leq \beta_W \\ = \infty & \text{for } \beta > \beta_W \end{cases}, \quad (2.54)$$

and $u(\gamma)$ as a HO in the parameter γ around a mean value of $\gamma = 0$ to represent axially deformed, prolate nuclei. The decoupled differential equation in β then is

$$\left[\frac{1}{\beta^4} \frac{\partial}{\partial \beta} \beta^4 \frac{\partial}{\partial \beta} - \frac{1}{4\beta^2} \frac{4}{3} L(L+1) + u(\beta) \right] \xi_L(\beta) = \varepsilon_\beta \xi_L(\beta), \quad (2.55)$$

where $\varepsilon = (2B/\hbar^2)E$ and $u = (2B/\hbar^2)V$. With $\tilde{\xi} = \beta^{3/2}\xi(\beta)$, $\varepsilon_\beta = k_\beta^2$, and $z = \beta k_\beta$, the Bessel equation

$$\tilde{\xi}'' + \frac{\tilde{\xi}'}{z} + \left[1 - \frac{v^2}{z^2} \right] \tilde{\xi} = 0, \quad (2.56)$$

with boundary condition $\tilde{\xi}(\beta_W) = 0$, is obtained, where

$$v = \sqrt{\left(\frac{L(L+1)}{3} + \frac{9}{4} \right)}. \quad (2.57)$$

The solution to (2.56) is

$$\xi_{s,L}(\beta) = c_{s,L} \beta^{-\frac{3}{2}} J_\nu \left(\frac{x_{s,L}}{\beta_W} \beta \right), \quad (2.58)$$

where J_ν is a Bessel function of first kind. The eigenvalues are given by

$$\varepsilon_{\beta;s,L} = \left(\frac{x_{s,L}}{\beta_W} \right)^2, \quad (2.59)$$

where the $x_{s,L}$ are the s th zero of J_ν in (2.58).

The resulting level scheme of the X(5) solution is shown in Fig. 2.9. The X(5)

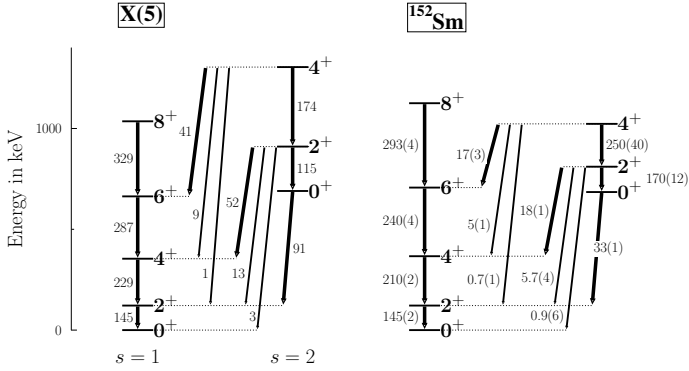


Figure 2.9.: Level scheme of the X(5) shape phase-transitional point between the U(5) and SU(3) dynamical symmetries of the IBM compared to the level scheme of ¹⁵²Sm. Figure adapted from [Iac01] and [Cas01b] using experimental numbers from [Mar13].

solution shows that the wave function as a function of the deformation parameter β of the first excited $s = 2$ 0_2^+ state has a node. This, the excitation of the nucleus in terms of the deformation parameter β , is the definition for a β band. The X(5) solution demonstrates that a β band can occur in any nucleus whose potential is soft in terms of the deformation parameter β , whereas in nuclei with a β -rigid potential no β excitation can occur. The first nucleus considered exhibiting the characteristics of the X(5) critical point has been ¹⁵²Sm [Cas01b]. Further examples are the nuclei ¹⁵⁰Nd [Krü02], ¹⁵⁴Gd [Dew03], ¹⁵⁶Dy [Möl06], and ¹⁷⁸Os [Dew05].

2.4.3 The confined- β -soft rotor model

The confined- β -soft rotor model (CBS) has been introduced [Pie04, Dus05] as a generalization of the X(5) solution. Its aim is the analytic description of the nuclei along the transitional path between the X(5) critical point ($R_{4/2} = 2.9$) and the SU(3) dynamical symmetry ($R_{4/2} = 3.33$) of the IBM. Like X(5) it uses a potential of the form $V(\beta, \gamma) = \nu(\beta) + u(\gamma)$. The potential $u(\gamma)$ is treated in the same way as in X(5). The potential of $\nu(\beta)$ is chosen as an infinite square well with boundaries at $0 \leq \beta_m \leq \beta \leq \beta_M$. Unlike in the X(5) ansatz values of $\beta_m \neq 0$ are allowed in the CBS. The potential can be parametrized by the ratio $r_\beta = \beta_m / \beta_M \in [0, 1]$, which, thus, denotes the width and stiffness of the potential in β . For any value of r_β the model is analytically solvable in terms of Bessel functions of first and second

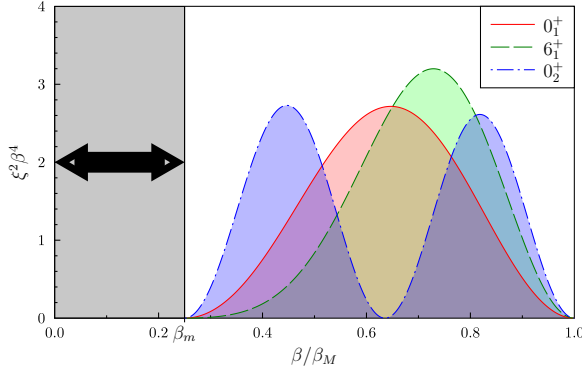


Figure 2.10.: Wave functions $\xi^2 \beta^4$ of the $s = 1$ 0_1^+ and 6_1^+ states and of the $s = 2$ 0_2^+ state in the CBS rotor model. The potential is an infinite square well with boundaries $0 \leq \beta_m \leq \beta \leq \beta_M$ shown here for $r_\beta = 0.25$. The wave function of the $s = 2$ 0_2^+ state exhibits its property as β excitation. The centrifugal stretching results in a shift of the centroids of the wave functions with increasing L .

kind. By variation of the parameter r_β , the entire path between the limits of the model can be spanned, i.e. the CBS solution for the limit $r_\beta = 0$ equals the X(5) solution which allows for large fluctuations in the shape parameter β , whereas the limit $r_\beta \rightarrow \infty$ corresponds to the case of a rigid rotor with equilibrium deformation and no fluctuations in β . In between those limits, the CBS model allows for shape fluctuations, whose degree depends on the choice of the structural parameter r_β . A schematic picture of the potential and its limits is given in Fig. 2.10.

The derivation of the resulting eigenvalues of the CBS model is to a large extent analogous to the aforementioned X(5). The decoupled differential equation for the deformation parameter β is

$$-\frac{\hbar^2}{2B} \left[\frac{1}{\beta^4} \frac{\partial}{\partial \beta} \beta^4 \frac{\partial}{\partial \beta} - \frac{1}{3\beta^2} L(L+1) + v(\beta) \right] \xi_L(\beta) = E \xi_L(\beta). \quad (2.60)$$

By choosing $z = \sqrt{E/(\hbar^2/2B)} \beta$ and $\tilde{\xi} = \beta^{3/2} \xi_L(\beta)$, the Bessel differential equation

$$\tilde{\xi}'' + \frac{\tilde{\xi}'}{z} + \left[1 - \frac{v^2}{z^2} \right] \tilde{\xi} = 0 \quad (2.61)$$

with boundary conditions

$$\tilde{\xi}_v(r_\beta z_M) = \tilde{\xi}_v(z_M) = 0 \quad (2.62)$$

and

$$v = \sqrt{\left(\frac{L(L+1)}{3} + \frac{9}{4}\right)} \quad (2.63)$$

is obtained. A quantization condition is given by

$$Q_v^{r_\beta}(z_M) = J_v(z_M)Y_v(r_\beta z_M) - J_v(r_\beta z_M)Y_v(z_M), \quad (2.64)$$

with the Bessel functions of first and second kind, J_v and Y_v . The solution of (2.61) is

$$\xi_{L,s}(\beta) = c_{L,s} \beta^{-\frac{3}{2}} \left[J_v \left(z_{L,s}^{r_\beta} \frac{\beta}{\beta_M} \right) + \gamma_Y Y_v \left(z_{L,s}^{r_\beta} \frac{\beta}{\beta_M} \right) \right], \quad (2.65)$$

with the relative amplitude γ_Y obtained by the boundary condition of (2.62) to

$$\gamma_Y = - \left[\frac{J_v(r_\beta z_M)}{Y_v(r_\beta z_M)} \right] \quad (2.66)$$

The resulting eigenvalues are

$$E_{L,s} = \frac{\hbar^2}{2B\beta_M^2} \left(z_{L,s}^{r_\beta} \right)^2, \quad (2.67)$$

where $z_{L,s}^{r_\beta}$ is the s th zero of $Q_v^{r_\beta}$ of (2.64). The $E2$ transition operator for transitions between states with no excitation in γ ($\Delta K = 0$) is given by

$$T_\mu^{\Delta K=0}(E2) = e_{\text{eff}} \left[\left(\frac{\beta}{\beta_M} + \chi \left(\frac{\beta}{\beta_M} \right)^2 \right) \right] D_{\mu 0}^2(\Omega), \quad (2.68)$$

with the parameters e_{eff} and χ and the Wigner function $D_{\mu 0}^2(\Omega)$. The operator is defined up to second order in β in analogy to the general $E2$ transition operator of the IBM of (2.29).

The states of the ground state band are denoted by $s = 1$, the states of the first $K = 0$ band are denoted by $s = 2$.

One feature predicted by model is the *centrifugal stretching*, i.e. the change of the moment of inertia of the nucleus with increasing angular momentum [Dus05]. It results in shifts of the centroids of the wave functions with increasing L . This is schematically depicted in Fig. 2.10.

Like the solution for the critical point X(5) the wave function for the $s = 2$ first excited 0^+ state has a node in β , and, thus, fulfills the definition of a β excitation. This has been further supported by a comparison [Kru11] of the results of CBS calculations with those of microscopic calculations in the relativistic mean field approach [Nik09, Li09] for the nuclei $^{150,152}\text{Nd}$. The results on the spectroscopic observables as well as on the wave functions are in very good agreement and further support the interpretation of the first $K = 0$ band in the CBS model as a genuine β band.



3 Experimental Method

All experiments presented in this work have been performed using γ -ray spectroscopy in the projectile-Coulomb excitation technique (Coulex). The main idea of this technique is a scattering reaction of one nucleus off another, in the course of which one or both of the reaction partners are being excited by the exchange of virtual photons. Coulomb excitation is particularly sensitive to the excitation of collective nuclear states and is therefore very well suited for the investigation of different aspects of nuclear collectivity. The nuclei of interest are prepared as an ion beam and collided onto a target. The experiments presented in this work have been performed at the Argonne National Laboratory (ANL) in Argonne, Illinois, USA, near Chicago. ATLAS at the ANL is a user facility under the support of the Office of Nuclear Physics of the United States Department of Energy (DOE). The local linear accelerator was used to provide the ion beams and the 4π -spectrometer Gammasphere was used for the detection of γ radiation.

3.1 Coulomb excitation

The electromagnetic excitation, or Coulomb excitation (Coulex) is a method that has been in use for nuclear structure research for several decades now. In this process a nucleus is excited in the electromagnetic field of another nucleus in a scattering reaction by the exchange of virtual photons. Under certain conditions the Coulomb excitation process can be described in a semi-classical way. Its main ideas will be briefly introduced in the following, based on the classic works on the topic by Alder and Winther [Ald56, Ald60, Win66, Ald75].

In collisions of heavy ions the cross sections for elastic scattering can be described by the well-known Rutherford cross-section

$$\left(\frac{d\sigma}{d\Omega}\right)_{\text{Rutherford}} = \frac{1}{4} \frac{a^2}{\sin^4\left(\frac{\theta}{2}\right)}, \quad (3.1)$$

with the half-distance of closest approach

$$a = \frac{Z_p Z_t e^2}{m_0 v}. \quad (3.2)$$

Here, Z_p and Z_t denote the atomic numbers of projectile and target nucleus, m_0 is the reduced mass of the system, and v is the velocity of the projectile. Although the Coulomb interaction per definition is an inelastic scattering process, under certain conditions it can be treated theoretically in a semi-classical approximation in which the classical trajectories of the elastic scattering process are a good approximation. These conditions are connected to two parameters that can be used to classify scattering reactions.

The effective strength of the interaction can be described by the *Sommerfeld parameter* η , which is given by the ratio of the half-distance of closest approach, a , and the deBroglie wavelength of the projectile ion:

$$\eta = 2\pi \frac{a}{\lambda} = \frac{Z_p Z_t e^2}{\hbar v} . \quad (3.3)$$

For values of $\eta \gg 1$ the electromagnetic interaction is strong enough to ensure that the short-range nuclear interactions are not involved in the reaction. The parameter ξ is the so-called *adiabacity parameter*

$$\xi = \frac{a}{\hbar v} \Delta E , \quad (3.4)$$

with the excitation energy ΔE . For large values of ξ the reaction becomes adiabatic, hindering the excitation process, while for values of $\xi \rightarrow 0$ the scattering happens as a very prompt event. If the conditions $\eta \gg 1$ and $\xi \rightarrow 0$ are fulfilled, a semi-classical treatment of the Coulomb excitation is a very good approximation. In the present work all presented experiments fulfill these conditions.

In the semiclassical approach the Coulomb excitation cross-section for the excitation of a state n can be described by

$$\left(\frac{d\sigma}{d\Omega} \right) = P_n \cdot \left(\frac{d\sigma}{d\Omega} \right)_{\text{Rutherford}} , \quad (3.5)$$

where P_n denotes the excitation probability of the state n . It can be written in terms of excitation amplitudes a_n as

$$P_n = \frac{1}{2J_i + 1} \sum_{m_i m_n} |a_n|^2 , \quad (3.6)$$

where J_i denotes the angular momentum of the initial state i , m_i and m_n denote the angular momentum projections of initial and final states i and n , respectively.

For the calculation of the excitation amplitudes, a perturbation calculation can be performed. A state $|\psi\rangle$ of a nucleus is subject to the Schrödinger equation

$$i\hbar \frac{\partial}{\partial t} |\psi\rangle = (H_0 + H_E(t)) |\psi\rangle, \quad (3.7)$$

with the Hamilton operator of the free nucleus, H_0 . $H_E(t)$ is the time-dependent Hamilton operator of the electric field. It can be written in terms of a multipole-expansion as

$$H_E(t) = \sum_{\lambda,\mu} \frac{4\pi Z_p e}{2\lambda + 1} r_p^{-\lambda-1}(t) Y_{\lambda\mu}(\theta_p(t), \phi_p(t)) M^*(E\lambda, \mu). \quad (3.8)$$

Here, $Y_{\lambda\mu}$ denotes the spherical harmonics and $r_p(t)$, $\theta_p(t)$, and $\phi_p(t)$ describe the time-dependent position of the projectile nucleus of atomic number Z_p expressed in spherical coordinates. The electric multipole operator M is defined as

$$M(E\lambda, \mu) = \int d^3r r^\lambda Y_{\lambda\mu}(\theta, \phi) \rho(\mathbf{r}), \quad (3.9)$$

with the charge density ρ .

The state $|\psi\rangle$ of (3.7) can be written as

$$|\psi\rangle = e^{-\frac{i}{\hbar} H_0 t} |\phi\rangle. \quad (3.10)$$

Then, the excitation amplitude can be defined as

$$a_n(t) = \langle n | \phi \rangle, \quad (3.11)$$

where $|n\rangle$ is the eigenvalue for the eigenstate E_n of the free Hamiltonian H_0 . In the semiclassical approach of the Coulomb excitation, the Hamiltonian H_E can be treated as a perturbation. It follows that the excitation amplitudes can be computed from

$$i\hbar \dot{a}_n = \sum_m \langle n | H_E(t) | m \rangle e^{-\frac{i}{\hbar}(E_n - E_m)t} a_m(t). \quad (3.12)$$

To solve this system of coupled differential equations of Eq. (3.12) the excitation and de-excitation processes have to be assumed to be infinitely separated in time. For the solution the boundary condition

$$a_n(t = -\infty) = \delta_{0n} \quad (3.13)$$

applies, i.e. that the nucleus is in its ground state prior to the scattering. The solution of the excitation amplitude is given by $a_n(t = \infty)$.

For the limit of pure one-step excitations, the solutions of (3.12) can be calculated analytically. The Coulex cross section for an electromagnetic excitation of a state is then given by

$$\sigma_{E\lambda} = \left(\frac{Z_p e}{\hbar v} \right)^2 a^{-2\lambda+2} B(E\lambda) f_{E\lambda}(\xi), \quad (3.14a)$$

$$\sigma_{M\lambda} = \left(\frac{Z_p e}{\hbar c} \right)^2 a^{-2\lambda+2} B(M\lambda) f_{M\lambda}(\xi). \quad (3.14b)$$

Here, a is again the half-distance of closest approach of (3.2). The values B are the reduced transition probabilities that are connected with the multipole operators via

$$\begin{aligned} B(E\lambda; J_i \rightarrow J_f) &= \sum_{m_f \mu} |\langle J_f m_f | M(E\lambda, \mu) | J_i m_i \rangle|^2 \\ &= \frac{1}{2J_i + 1} |\langle J_f || M(E\lambda) || J_i \rangle|^2. \end{aligned} \quad (3.15)$$

The values of the functions $f_{\sigma\lambda}(\xi)$ are tabulated in Ref. [Ald56]. With increasing multipolarity, the Coulomb excitation cross sections theoretically decrease by approximately two orders of magnitude. In practice, however, the low-lying levels of collective nuclei are connected by strong $E2$ transitions while $E1$ strengths usually are negligible. Therefore, Coulomb excitation can be used for the selective excitation of collective states and is, thus, the ideal tool for the investigation of nuclear collectivity.

In reality, also higher order effects play an increasing role in the excitation process with increasingly heavier target nuclei. In the case of the present experiments, in which only light carbon targets were used, these effects are only secondary effects. For a correct treatment of these effects, however, the coupled-channel code CLX [Owe, Owe80] has been used for the calculations of the Coulomb excitation cross sections.

In the previous discussion the excitation due to the magnetic field has been neglected. In fact, the cross-sections for magnetic excitations are suppressed compared to electric excitations by a factor of β^2 , which can be inferred from the first factors in the expressions of (3.14). The derivation of the cross section for magnetic excitations is, however, analog to the derivation for the electric case shown above.

The relation of Eq. (3.15) gives a good impression why the Coulex technique is particularly suited for the investigation of collective phenomena in nuclei. Collective nuclei usually exhibit strong $E2$ transitions connecting the excited states. The Coulomb excitation cross sections are very sensitive to these transitions and allow for strong excitations of nuclear collective states.

3.2 Experimental Principle

3.2.1 Basic Concept

The underlying idea of the experiments performed in the course of this work is the excitation of collective states via the electromagnetic excitation mechanism – Coulex – and the detection of deexcitation γ rays with a Germanium-detector array. Coulex is a well-established experimental method; the theoretical framework has already been outlined in section 3.1.

For the reactions studied in this work, ion beams of the nuclei of interest have been impinging on thin carbon targets; in the experiments presented in this work, targets with a thickness of 1 mg/cm² have been used (only in the ¹⁹⁶Pt experiment a target with a thickness of 0.585 mg/cm² has been used). For historic reasons, such a setup is usually referred to as Coulomb excitation *in inverse kinematics* or *projectile Coulex*, respectively. Besides the trivial fact that some isotopes are not practical to be prepared as a target with reasonable effort – e.g. gaseous elements or rare isotopes such as ^{130,132}Ba with a natural abundance of $\approx 0.1\%$ – inverse kinematics Coulex on carbon targets features several experimental advantages that shall be discussed in the following.

Natural carbon consists of 98.9% ¹²C isotopes and 1.1% ¹³C isotopes. The first excited states of these isotopes reside at energies of 4.44 MeV and at 3.09 MeV, respectively. Both of these energies are well above the sensitivity limit of approximately 2.5 MeV for γ rays from projectile excitations and, thus, will not appear in the spectra.

Secondly, the choice of a low-Z target material like carbon favors one-step excitations. This facilitates the calculations for the Coulomb excitation cross-sections, in particular for nuclei that bare a complicated level scheme of excited states as it has been the case for the Pt experiments in the present work.

The underlying kinematics of heavy projectiles scattering off light target nuclei lead to a very small deflection angle of the projectile ions. In the case of the Barium nuclei, the maximum scattering angle in the lab frame θ_{sc} can be calculated to $\theta_{sc}^{\max}({}^{130,132}\text{Ba}) \approx 5.3^\circ$, in the cases of ¹⁵⁴Sm and the Pt isotopes $\theta_{sc}^{\max}({}^{154}\text{Sm}) \approx 4.5^\circ$ and $\theta_{sc}^{\max}({}^{194,196}\text{Pt}) \approx 3.5^\circ$, respectively. A plot of the scattering angles of projectile and recoil target nuclei in the lab frame is shown in Fig. 3.1 for the ¹³⁰Ba beam. In the analysis of the data, for instance for the correction of the Doppler shift (cf. 4.1) or the angular distribution analysis (cf. 4.2), an event-by-event determination of the polar angle θ_γ between the γ ray and the trajectory of the emitting nucleus is necessary. In principle, θ_γ can be deduced from the polar and azimuthal scattering angles (θ_{sc}, ϕ_{sc}) and the polar and azimuthal angles of the γ rays with respect to

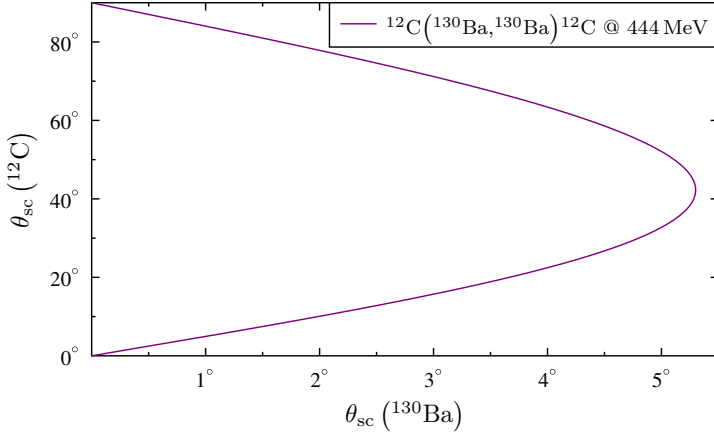


Figure 3.1.: Plot of the scattering angles θ_{sc} of projectile and recoil target nuclei in the lab frame on the example of the ^{130}Ba experiment, which features the largest projectile scattering angle of the experiments in this work.

the beam axis, $(\theta_{\text{Ge}}, \phi_{\text{Ge}})$, determined by the positions of the Ge detectors in the spectrometer, cf. table 3.1. Yet, the opening angle of the Ge detectors is 14.8° and, hence, nearly entirely determines the resolution to which θ_γ can be deduced. Therefore, the angles (θ_{sc}, ϕ_{sc}) can be neglected, so that $\theta_\gamma \approx \theta_{\text{Ge}}$ can be used as a very good approximation during the data analysis. Consequently, a separate particle detection of scattered particles, e.g. with a DSSSD detector, is not necessary and a high-statistics experiment is feasible.

In order to exclude contributions of nuclear forces to the excitation processes, one has to ensure that the distance of closest approach of projectile and target nuclei is large enough. The nuclear interaction is very short ranged. Hence, it will not contribute to the excitation until the matter distributions of the colliding nuclei overlap. This can be prevented by keeping the kinetic energy of the projectiles E_{beam} below the threshold necessary to overcome the Coulomb repulsion of the nuclei. This threshold is usually referred to as the *Coulomb barrier* E_{Coul} and can be calculated by

$$E_{\text{Coul}}^{\text{CMS}} = \frac{e^2}{4\pi\epsilon_0} \cdot \frac{Z_p Z_t}{r_p + r_t + r_{\text{extra}}} \quad (3.16)$$

with the proton numbers of projectile and target Z_p and Z_t , the nuclear radii r_p and r_t , and a safety distance r_{extra} , which takes into account the non-spherical density

distribution of atomic nuclei. The radii r_i can be expressed as $r_i \approx r_0 \sqrt[3]{A_i}$, with $r_0 = 1.25$ fm and the atomic mass numbers A_i . Equation (3.16) applies to the kinetic energy in the center of mass system $E_{\text{Coul}}^{\text{CMS}}$. It can be transferred to the energy of the Coulomb barrier in the lab frame $E_{\text{Coul}}^{\text{lab}}$ using the relation

$$E_{\text{Coul}}^{\text{lab}} = \frac{A_p + A_t}{A_t} \cdot E_{\text{Coul}}^{\text{CMS}} \quad (3.17)$$

with the atomic mass numbers A_p and A_t of projectile and target. For a given projectile ${}^Z_p A_p$ the value of $E_{\text{Coul}}^{\text{lab}}$ increases for heavier target elements. In the experimental setup surrounding the target, however, only elements heavier than carbon are being used, in particular Aluminum and steel (Fe). Consequently, choosing a beam energy $E_{\text{beam}} < E_{\text{Coul}}^{\text{lab}}(A_t Z_t = {}^{12}\text{C})$ also guarantees the prevention of nuclear reactions of the projectiles with other materials in the setup. This assures experimental γ -ray spectra free of background from nuclear reactions and is an inherent feature of projectile Coulex of heavy nuclei on a light carbon target. This has been demonstrated in an initial projectile-Coulex experiment on the nucleus ${}^{96}\text{Ru}$ [Pie01].

For the successful execution of the experiment, the choice of proper values for the experimental parameters is important. The most crucial parameter certainly is the beam energy E_{beam} . On the one hand, the Coulex cross-sections increase strongly with increasing E_{beam} . On the other hand the beam energy is limited by the Coulomb barrier of the reaction. Finding a suitable value, thus, is always a trade-off between those limits. In the experiments presented in this work, E_{beam} was chosen to $\approx 85\%$ of the Coulomb barrier.

Another crucial experimental parameter is the beam intensity I_{beam} , often also referred to as *beam current*. It is a measure of how many projectile nuclei collide onto the target per unit of time. Most of the time it is given in units of pA. In general, I_{beam} is best chosen as large as possible, since the reaction rate is proportional to the number of projectile ions. On the other hand, the maximum possible beam intensity $I_{\text{beam}}^{\text{max}}$ is also subject to different constraints. One possible limiting factor might be the ion source. For the experiments using Barium beams, the ion current was limited due to the low abundance of the isotopes ${}^{130}\text{Ba}$ and ${}^{132}\text{Ba}$ in the source, even though it had been enriched. This limited the achievable average beam intensity to $I_{\text{beam}}({}^{130}\text{Ba}) = 0.25$ pA and $I_{\text{beam}}({}^{132}\text{Ba}) = 0.5$ pA, respectively. Another limit is imposed by the maximal count rate the data acquisition (DAQ) can handle. The count rate is nearly entirely determined by the decay of the 2_1^+ state. The limit of the data acquisition is usually on the order of 10-20 kHz. With the usual cross sections for the excitation of the 2_1^+ state, this results in a maximal beam intensity of ≈ 1 pA.

3.2.2 Connection to nuclear structure observables

The experimentally accessible quantity in the present Coulex experiments is the deexcitation γ radiation detected by the HPGe detectors surrounding the reaction point. Both, the gamma decay and the Coulomb excitation process, can be described using the same electromagnetic nuclear matrix elements. Their relevance in the Coulomb excitation process has been outlined in 3.1. The objective of the data analysis is the connection of the prime observable – the γ -ray intensities from the depopulation of the excited states – with the underlying nuclear transition matrix elements. The physical relation of this connection will be discussed in the following.

The deexcitation of the states populated in the Coulex reactions happens by an electromagnetic decay, i.e. by the emission of a γ ray. Its energy E_γ is the difference between the energies of the initial and final states E_i and E_f (neglecting the small repulsion effect on the emitting nucleus). Usually the electric field of the electromagnetic decay is expanded into a multipole series. Depending on the spins and parities of the connected states J_i^π and J_f^π the multipolarity λ of the emitted radiation is limited to certain values which are given by the selection rules

$$|J_f^\pi - J_i^\pi| \leq \lambda \leq J_f^\pi + J_i^\pi, \quad \pi_f \pi_i = \begin{cases} (-1)^\lambda & \text{for } E\lambda \\ (-1)^{\lambda-1} & \text{for } M\lambda \end{cases}, \quad (3.18)$$

where $\sigma = E, M$ denotes the electric or magnetic character of the radiation and π_i and π_f are the parities of initial and final states. As a consequence, transitions connecting states J^π with 0^+ states are of pure multipolarity. In cases where more than one multipolarity is allowed, as a general rule, the lowest possible multipolarity dominates in the decay. At the same time, electric transitions $\sigma = E$ dominate over magnetic transitions $\sigma = M$. However, this rule is just a rule of thumb, whereas the real composition of the multipolarities in the γ decay is dependent on the wave functions of initial and final states i and f . In collective nuclei, however, often $E2$ transitions are very strong and dominate. A measure for the composition of radiation in terms of multipolarities is the multipole mixing ratio δ defined by

$$\delta^2 = \frac{\Gamma_i(\lambda + 1)}{\Gamma_i(\lambda)}, \quad (3.19)$$

with the partial width Γ_i of the transition i . It is connected to the natural width of the state Γ via the sum over all depopulating transitions

$$\Gamma = \sum_i \Gamma_i. \quad (3.20)$$

The width of an isolated resonance is related to the lifetime of the state via

$$\tau = \frac{\hbar}{\Gamma} . \quad (3.21)$$

In γ -ray spectroscopy experiments, the measured γ -ray intensity is proportional to the partial transition width, $I_i \propto \Gamma_i$. The partial width is also closely related to the reduced transition probability of a decay $B(\sigma\lambda)$ by

$$\begin{aligned} \Gamma_i &= 8\pi \frac{\lambda + 1}{\lambda [(2\lambda + 1)!!]^2} \left(\frac{E_\gamma}{\hbar c} \right)^{2\lambda+1} \cdot B(\sigma\lambda; J_i \rightarrow J_f)_\downarrow \\ &= c_{\pi\lambda} \left(\frac{E_\gamma}{\text{MeV}} \right)^{2\lambda+1} \cdot B(\sigma\lambda; J_i \rightarrow J_f)_\downarrow . \end{aligned} \quad (3.22)$$

The coefficients $c_{\pi\lambda}$ for the most relevant multiplicities are given by

$$\begin{aligned} c_{E1} &= 1.0466609 \frac{\text{meV}}{10^{-3} e^2 \text{fm}^2} , & c_{M1} &= 11.574 \frac{\text{meV}}{\mu_N^2} , \\ c_{E2} &= 8.0638146 \frac{\text{meV}}{e^2 \text{b}^2} , \\ c_{E3} &= 3.7566888 \times 10^{-4} \frac{\text{meV}}{e^2 \text{b}^3} , \\ & & \frac{c_{E2}}{c_{M1}} &= 0.696718 \frac{\mu_N^2}{e^2 \text{b}^2} . \end{aligned}$$

The values of $B(E\lambda)$ and $B(M1)$ are given in units of $e^2 \text{b}^\lambda$ and μ_N^2 . A more commonly used way of the presentation of transition strengths, in particular for $B(E\lambda)$ values, is by the introduction of single-particle units or *Weisskopf units* (W.u.). They are estimates for a transition in which only one nucleon is involved. Large values of $B(E\lambda)$ in these units, thus, resemble transitions in which many nuclei participate. Therefore, $B(E\lambda)$ in W.u. are a good indication for the collectivity of γ transitions. The conversion between the different units can be done by the relations [Suh07]

$$\begin{aligned} B(E1; J_i \rightarrow J_f) &= 6.446 \times 10^{-4} A^{2/3} e^2 \text{b} , \\ B(E2; J_i \rightarrow J_f) &= 5.940 \times 10^{-6} A^{4/3} e^2 \text{b}^2 , \\ B(E3; J_i \rightarrow J_f) &= 5.940 \times 10^{-8} A^2 e^2 \text{b}^3 . \end{aligned}$$

The reduced transition probabilities can be computed from the nuclear transition matrix elements by

$$\begin{aligned} B(\sigma\lambda; J_i \rightarrow J_f) &= \sum_{m_f \mu} \left| \langle J_f m_f | M(E\lambda, \mu) | J_i m_i \rangle \right|^2 \\ &= \frac{1}{2J_i + 1} \left| \langle J_f || M(E\lambda) || J_i \rangle \right|^2 , \end{aligned} \quad (3.23)$$

where $M(E\lambda, \mu)$ denotes the electromagnetic multipole operator. The reduced transition probabilities are of big importance for nuclear structure research, since they provide a link between theoretical predictions and experimental observables. The relation of Eq. (3.23) has already been introduced earlier in the description of the mechanism of Coulomb excitation, cf. 3.1. The Coulomb excitation of nuclear states and their electromagnetic decay are described by the same theoretical framework. Thus, the Coulomb excitation method allows for the measurement of $B(\sigma\lambda)$ transition strengths.

3.3 Experimental Setup

The experiments performed in the course of this work have been performed at the Argonne National Laboratory (ANL). Ion beams of the investigated isotopes have been provided by the ATLAS accelerator. γ radiation has been detected using the Gammasphere array.

3.3.1 ATLAS accelerator

The Argonne Tandem Linac Accelerator System (ATLAS) is a superconducting ion accelerator and is capable of providing and accelerating beams of nearly all stable isotopes across the nuclear chart to energies up to 17 MeV/u. Its layout is depicted in figure 3.2 and outlined in [Bol93]. The ions are provided by the so-called Positive-Ion Injector (PII), which consists of an ECR ion source and a 12 MV injector linac. The main section of ATLAS consists of a 20 MV booster linac and the 20 MV ATLAS linac, before the beams are delivered to the different experimental setups, one of which is the Gammasphere spectrometer.

The beams produced by ATLAS are pulsed with a frequency of 12.125 MHz. This is of great use for the experimenter during the analysis process, when this feature is used to create beam-on and beam-off spectra for the subtraction of random background events (cf. 4.1).

3.3.2 Gammasphere spectrometer

For the detection of γ rays the Gammasphere spectrometer [Lee90] was used. In its full setup, this array consists of 110 high-purity Germanium detectors (HPGe). A picture of the Gammasphere array is shown in Fig. 3.3

The single HPGe detectors have an efficiency of 78% with respect to the NaI standard [Bea96]. They are placed at a distance of 25.25 cm [Lee97] to the target

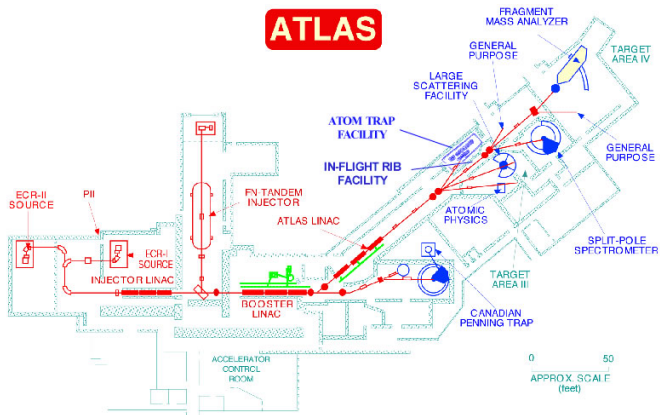


Figure 3.2.: Floorplan of the ATLAS accelerator facility at the ANL. The image has been taken from the ATLAS webpage [ATL13].

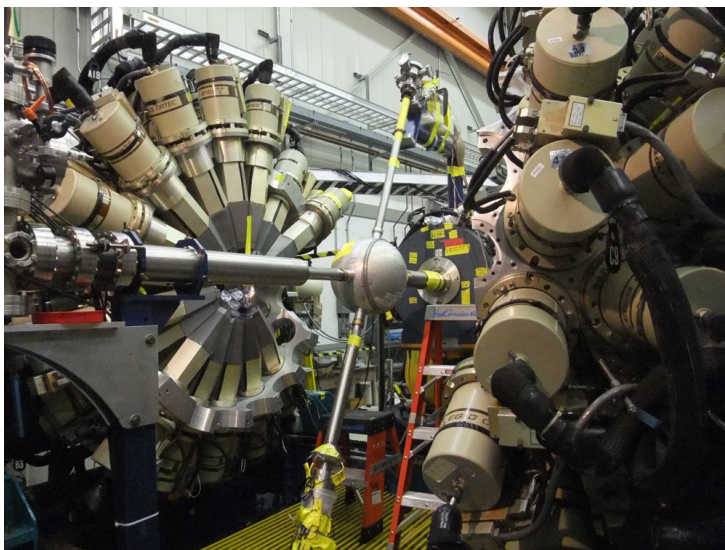


Figure 3.3.: Photograph of the Gammasphere array taken during the preparation of the experiment on the nuclei $^{130,132}\text{Ba}$. In this picture, the hemispheres of Gammasphere have been opened to allow for access to the target chamber.

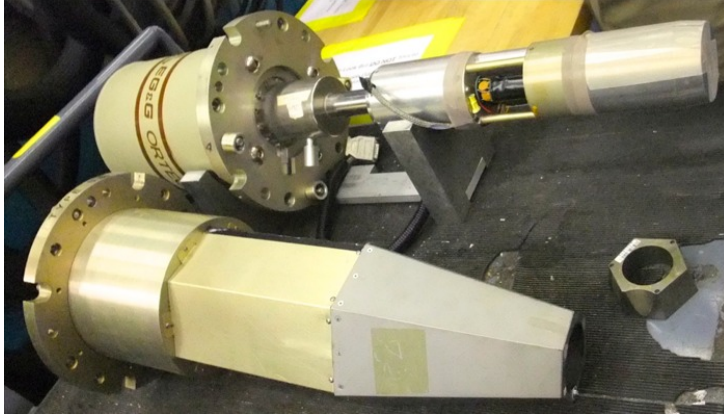


Figure 3.4.: Photograph of a partly disassembled detector module of Gammasphere. The structure in the upper part of the photo shows a capsuled Ge detector mounted to the cryostat. The BGO shielding is placed in the structure in the bottom of the picture. The hexagonal structure in the right of the picture is the Hevimet shielding of the BGO detector.

position resulting in an opening angle of 14.8° [Nol94]. Each detector is enclosed by a Bismuth-Germanate scintillator (BGO) with a large γ -ray detection efficiency. These pairs of detectors are run in an anti-coincidence mode, i.e., a γ -ray detection in a BGO will veto a coincident γ -ray detection in the corresponding HPGe detector. The BGO detectors themselves are shielded against γ rays from the target position by so-called *Hevimets* made of a tungsten-nickel-copper alloy. They ensure that the BGO detectors only detect γ rays that have been Compton scattered out of the HPGe crystals. This construction principle allows for an efficient suppression of Compton-scattered γ rays. A photograph of a partly disassembled detector module is shown in figure 3.4.

The HPGe detectors are arranged in a 4π geometry, covering up to 47% of the total solid angle [Lee97]. The detectors are grouped into 17 rings of 5 to 10 detectors of the same polar angle with respect to the beam axis. This allows for angularly resolved measurement of γ rays. The polar angles of the detector rings are summarized in table 3.1. The total γ -ray detection efficiency of Gammasphere is 9.9% at an energy of 1.33 MeV [Lee97]. In its setup at the ATLAS facility, Gammasphere is placed in close proximity to the Fragment-Mass-Analyzer (FMA). This requires the permanent removal of the first detector ring under the most forward polar angle of 17.3° . It consists of 5 detectors. In addition, not all of the remaining detectors are

Table 3.1.: Polar angles θ_{Ge} of the detector rings of the Gammasphere array. In the setup at the ATLAS facility, ring #1 is permanently removed.

Ring #	θ_{Ge}	Ring #	θ_{Ge}	Ring #	θ_{Ge}
1	17.3°	7	79.2°	13	121.7°
2	31.7°	8	80.7°	14	129.9°
3	37.4°	9	90.0°	15	142.6°
4	50.1°	10	99.3°	16	148.3°
5	58.3°	11	100.8°	17	162.7°
6	69.8°	12	110.2°		

in use for different reasons, so that, consequently, ~ 100 detectors were used in the experiments presented in this work.

Gammasphere was originally designed for experiments that yield large γ -ray multiplicities, e.g. as they occur in high-spin physics experiments. Usually, the triggers of the data acquisition (DAQ) of Gammasphere are, thus, set to a γ -ray multiplicity $\gg 1$. For the experiments presented in this work, however, the trigger of the DAQ system has been set to 1, i.e. recording every γ ray detected, regardless of any coincidence conditions. As a consequence, the present measurements yield a large number of events and therefore a large statistical basis. Still, in these experiments $\approx 2\%$ of the recorded events are of γ -ray multiplicity > 1 , allowing for the creation of $\gamma\gamma$ -coincidence matrices and coincidence analyses (cf. section 4.1).

A synopsis of the parameters of the experiments of the present work is given in table 3.2.

Table 3.2.: Overview of the basic experimental parameters in the experiments. During the Pt experiments, two different settings have been used for singles and coincidence measurements – see chapter 4.4.2 for details.

	GSFMA 282 Sept. 2011		GSFMA 218 Jul. 2008	GSFMA 265 Nov. 2010	
	¹³⁰ Ba	¹³² Ba	¹⁵⁴ Sm	¹⁹⁴ Pt	¹⁹⁶ Pt
E_{beam} (MeV)	444	444	570	850	850
I_{beam} (pA)	0.25	0.5	1	1 / 5	1 / 2
t_{duration} (h)	14.5	14.5	12	28 / 12	38 / 24
d_{target} (mg/cm ²)	1.0	1.0	1.0	1.0	0.585 / 1.0

4 Data analysis and results

Within this work some features of the analysis have been improved compared to previous experiments [Ahn09, Ahn12, Coq09, Coq10, Coq11, Rai06, Rai10], e.g. the handling of the coincidence data and the treatment of the sign-dependencies in the CLX calculations. The process of data sort and preparation will be discussed in the following section 4.1. In the subsequent sections 4.2 and 4.3, the calculations are described before their results will be presented in 4.4.

4.1 Data processing and corrections

In the beginning of the data analysis process, the data is available in its raw format. It consists of a chronological list of the events processed by the Gammasphere DAQ system. Each of the events itself is subdivided into a header containing information about the event in general – e.g. the γ -ray multiplicity of the event or a timing information of the first γ ray observed – as well as detailed information on each of the γ rays observed in this event – this information contains the ID of the observing detector, the energy of the γ ray and time information with respect to the RF signal of the ATLAS accelerator. It is the purpose of the data-sorting process to generate 1D and 2D histograms from the list mode data in order to visualize energy spectra and different types of correlations in the data. A sorting code has been written to accomplish this task. It is based on the code GSSort [Gam13] which is usually used for the online analysis of experiments using Gammasphere. It is based on the ROOT framework [Bru97]. In the following, the steps of the data analysis will be discussed.

In the beginning of the data preparation, the energy calibration for each of the ≈ 100 detectors has to be checked. Analogously, the correct alignment of the timing information with respect to the RF signal has to be checked for all detectors. This is usually done by sorting one run of the raw data using a sorting code generating only very simple spectra of energy and time information. This process and the next step, the Doppler correction, however, presuppose each other and can, thus, not be performed independently from each other.

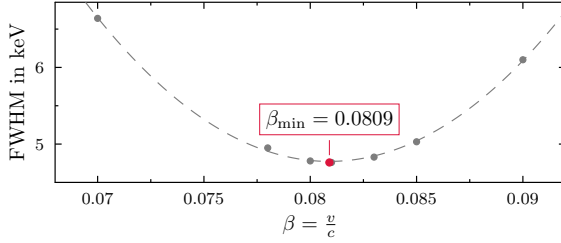


Figure 4.1.: Determination of the velocity β of the ions from minimizing the width of the $2_1^+ \rightarrow 0_1^+$ peak in the sum spectrum, shown on the example of ^{194}Pt . The uncertainties in the peak widths are too small to be seen in the figure.

Doppler correction

Gamma radiation emitted in-flight by the projectile ions is subject to the Doppler effect. The Doppler-shifted energy E_D of a γ ray emitted by an ion moving with a velocity $\beta = \frac{v}{c}$ can be expressed by

$$E_D(\theta_\gamma, \beta) = E_0 \frac{\sqrt{1 - \beta^2}}{1 - \beta \cos \theta_\gamma}, \quad (4.1)$$

with the energy of the γ ray in the frame of the nucleus E_0 and the angle θ_γ of the γ ray with respect to the trajectory of the ion. This angle can be approximated by the angle θ_{Ge} of the detector with respect to the beam axis, cf. 3.2.1. In the sorting process for each γ ray the ID of the observing HPGe detector is linked with the polar angle θ_{Ge} of the detector and a correction of the Doppler effect on the γ -ray energy according to (4.1) is performed. The effects of the Doppler correction on the sum spectrum are depicted in the overview plot in Fig. 4.8. With no Doppler correction applied (Fig 4.8(a)), the detectors in each of the 16 rings observe γ rays of the energy E_0 at different energies $E_D(\theta_\gamma)$. Consequently, the γ rays from a transition are widely distributed over a broad energy range. Applying the Doppler correction leads to distinct peaks in the spectra (Fig 4.8(b)).

A necessity for a proper Doppler correction is the knowledge of the velocity β of the projectile ions. The value of β , however, can be extracted from the experimental data: For a proper Doppler correction, the peaks of a transition reside at the same energies for all rings. In the sum spectrum, this results in a minimum peak width in case of a proper Doppler correction. In practice, one measures the resulting

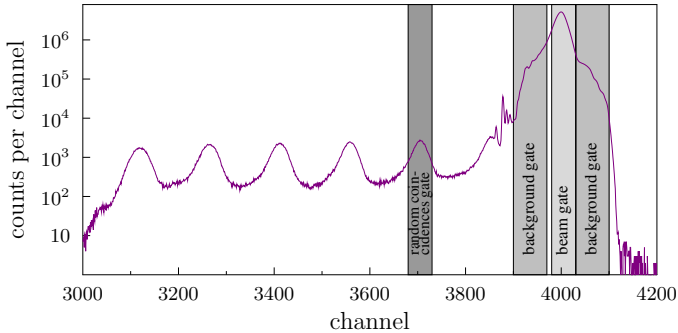


Figure 4.2.: Time spectrum of the ^{130}Ba experiment. Time conditions on γ rays are indicated by the shaded areas. The abscissa of the spectrum represents the time difference between the detection of a γ ray and the RF signal preceding the detection of the first γ ray of an event. The direction of the abscissa is reversed, i.e. time evolves from right to left.

peak widths for different sorting processes using different values of β . This is visualized in Fig. 4.1. In close proximity to the correct value β_{\min} the peak widths approximately follow a parabola, whose vertex can be adopted as the value to be used for the Doppler correction.

Background subtraction

One drawback of the Doppler correction, however, stems from the fact that the correction is inevitably also applied on γ rays of the room background radiation. For these, the assumption of in-flight emission does not hold true and, therefore, incorrectly Doppler-corrected background peaks in the spectra are distributed over a wide energy range. This can be observed very well on the example of the well-known 1461 keV line of the decay of ^{40}K in Fig. 4.8(a) and (b).

The emission of background radiation is randomly distributed in time, while γ rays from Coulex reactions can only occur in the moment when a beam bunch is colliding with the target. This fact can be made use of to discriminate γ rays from background radiation against those following Coulex.

Figure 4.2 shows a time spectrum. The abscissa of the spectrum represents the time difference between the detection of a γ ray and the RF signal preceding the detection of the first γ ray of an event. In the DAQ system an electronic coincidence window is opened by this first γ ray which is larger than the time difference

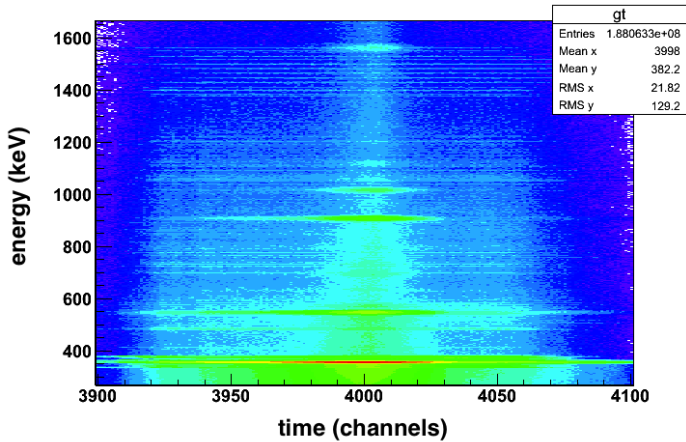


Figure 4.3.: Time-energy matrix of the ^{130}Ba experiment. The time is shown on the abscissa, the energy is shown on the ordinate.

between successive beam bursts. Therefore, several spikes are present in the time spectrum that are due to γ rays induced by several different beam bursts within the coincidence window. γ rays, either following Coulex or originating from background radiation, however, are expected to occur only in a very small fraction of beam bursts, so that in the coincidence window contributions from consecutive beam bursts are negligible. Consequently, the time spectrum is dominated by a single peak which surmounts the other structures by more than three orders of magnitude. In Fig. 4.2 this peak resides between the channels 3900 and 4100, approximately. The large peak itself exhibits a substructure, that becomes visible in the time-energy matrix, which is depicted in Fig. 4.3 on the example of the ^{130}Ba experiment. γ rays following the beam-induced Coulex reactions all occur at times corresponding to a few channels around channel 4000 while γ rays from background radiation are distributed over the whole width of the peak.

For the background subtraction new types of spectra are created for which different time conditions are imposed on the gamma rays. These so-called *gates* are indicated in the time spectrum of Fig. 4.2. The *beam-gated* spectrum only contains gamma rays for which the time condition of the beam gate is fulfilled. Such a spectrum is shown in Fig. 4.8(c). The *background-gated* spectrum contains gamma rays in the background gate. A third spectrum is then created in which the background spectrum is subtracted from the beam-gated spectrum. The subtraction is normal-

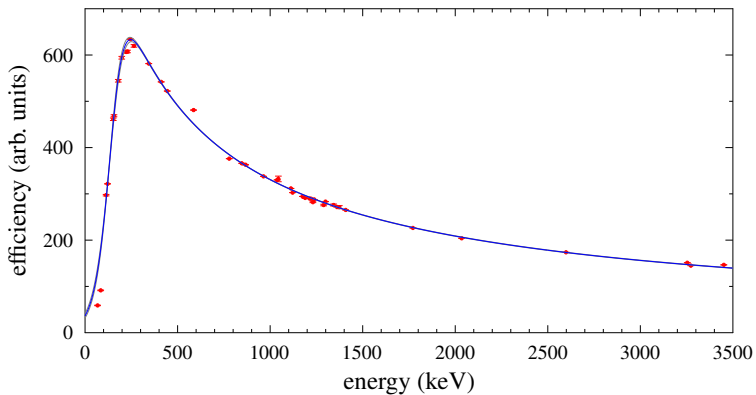


Figure 4.4.: Relative efficiency curve for the Pt experiment. Due to the use of ^{152}Eu , ^{56}Co , and ^{182}Ta calibration sources, a very precise efficiency calibration was possible over the energy range of ≈ 100 keV – 3500 keV

ized on the 1461 keV line. The result is a *background-subtracted* spectrum as it can be seen in Fig. 4.8(d).

Efficiency calibration

One of the most influential and most important corrections is to correct the measured transition intensities for the relative detection efficiency. This is important for two reasons. First, the detector rings are made up by different numbers of individual detectors and, consequently, their detection efficiency differs. A correction, thus, is needed for the inter-comparability of intensities measured in different rings. Second, the detection efficiency is strongly E_γ dependent. An efficiency calibration thus guarantees comparability of γ intensities at different energies. For the determination of the efficiency $\varepsilon(E_\gamma)$, measurements with calibration sources have been performed in each experimental campaign using sources of the isotopes ^{182}Ta , ^{152}Eu , and ^{56}Co . The advantage of this combination of sources is their different energy coverage. ^{182}Ta , for instance, covers the low-energy branch $E_\gamma < 250$ keV and ^{56}Co provides gamma rays up to an energy of $E_\gamma \approx 3.5$ MeV. However, not all sources have been available in all experiments, in particular an ^{182}Ta source could not be used in all experiments because of its small half-life of only $T_{1/2} \approx 115$ days.

The relative intensities of the decays of the sources are known with large precision. The efficiencies ε for each of the transitions is determined by $\varepsilon = A/I$, with the experimentally determined peak area A and the literature value of the

relative intensity I . An absolute determination of ε is not necessary since the analysis (cf. sec. 4.3) is carried out relative to the intensity of the 2_1^+ state. A fit was then performed to the data points from the measurement of $\varepsilon(E_\gamma)$ to the empiric formula

$$\varepsilon(E_\gamma) = a \cdot \exp\left(-b \cdot \ln\left(E_\gamma - c + d \cdot \exp\left(e \cdot E_\gamma\right)\right)\right), \quad (4.2)$$

with the fit parameters $a \dots e$. As an example, a fit to the data from the Pt experiment is shown in Fig. 4.4. For experiments where the ^{182}Ta source was not available, a simplified version of eq. (4.2) was applied, in which the parameters d and e were set to $d = e = 0$:

$$\varepsilon(E_\gamma) = a \cdot \exp\left(-b \cdot \ln\left(E_\gamma - c\right)\right). \quad (4.3)$$

This formula does not describe the behavior of the efficiency curve for the low-energy branch below the maximum at $E \approx 250$ keV. In most experiments, however, only transitions at energies $E > 300$ keV are of significance, so that the simplified formula of eq. (4.3) is sufficient for the correction of the detection efficiency. An exception has been the analysis of the experiment on ^{154}Sm , where the 2_1^+ state resides at an energy of 82 keV. See 4.4.1 for details.

Coincidence data

In the experiments, the DAQ was set to singles mode, i.e. every γ ray detected by one of the HPGe detectors was also recorded to disk. For a large majority of the events, the γ -ray multiplicity is one. In 1-2% of the data, depending on the actual experiment, however, more than one γ ray has been recorded. A plot of the multiplicity distribution is shown in Fig. 4.5. This data is of special interest during the analysis as it allows to reveal coincidence relations between the γ rays of different energies. Such information is used for the reconstruction of the level scheme of a nucleus and for the determination of transition intensities of weak transitions not visible in the singles spectra.

In practice, this data is evaluated by sorting the coincidence data into $\gamma\gamma$ matrices. Those are symmetrical 2D histograms, in which the contents of the channels $(E_{\gamma_1}, E_{\gamma_2})$ and $(E_{\gamma_2}, E_{\gamma_1})$ are incremented when two γ rays of energies E_{γ_1} and E_{γ_2} are detected during the same event. An example of such a matrix is depicted in Fig. 4.6. In the further analysis of the data, gates are set on several transitions and the content of the corresponding channel is projected and plotted as a spectrum. An example is shown in the overview plot of Fig. 4.8(d).

The bare $\gamma\gamma$ matrices usually contain random coincidences. These are transitions that seem to be coincident to other transitions or to themselves without a real physical coincidence relation. These artifacts hamper reliable coincidence analyses.

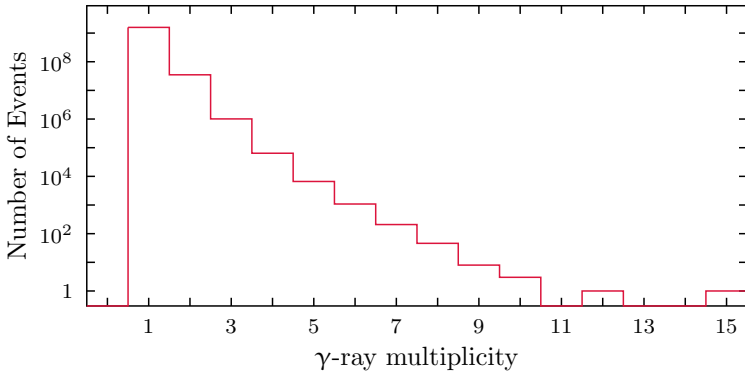


Figure 4.5.: Plot of the multiplicity distribution of the events in the ^{194}Pt experiment with the DAQ trigger set to γ -ray singles.

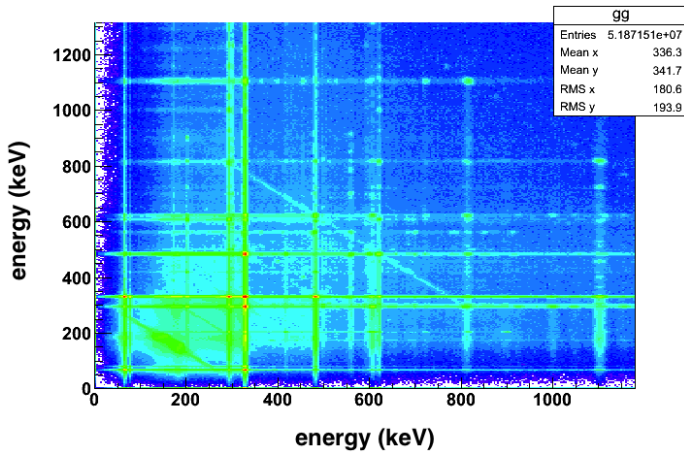


Figure 4.6.: $\gamma\gamma$ -coincidence matrix of the ^{194}Pt experiment.

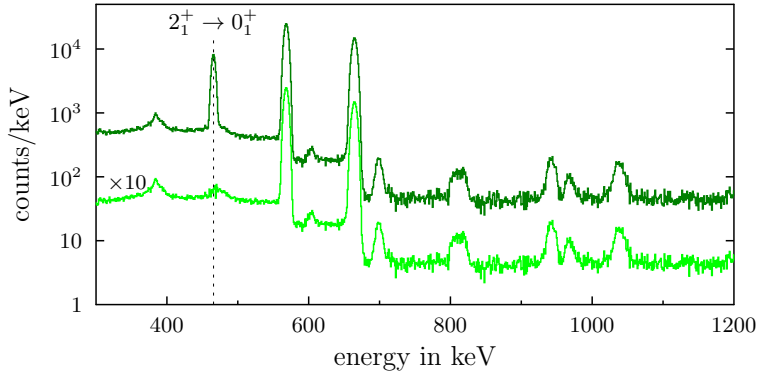


Figure 4.7.: Coincidence spectrum of the ^{132}Ba experiment gated on the $2_1^+ \rightarrow 0_1^+$ transition. The subtraction of random coincidences causes the unphysical peak of the $2_1^+ \rightarrow 0_1^+$ transition coincident to itself to vanish. The rest of the spectrum remains unaltered. For better visibility of the effect, the subtracted spectrum on the bottom has been shifted by one order of magnitude.

Within this work a subtraction of the random coincidences from the $\gamma\gamma$ coincidence matrix has been implemented, which will be described in the following. For statistical reasons more than one Coulex reaction can occur in a small number of beam bursts impinging on the target. In such a case it is possible that in the same electronic coincidence window two or more γ rays are detected without any real physical coincidence relation. The frequency of such a scenario can be expected to be approximately as large as the occurrence of Coulex-induced γ ray detections in one of the consecutive beam bursts in the same coincidence window. Therefore, another time gate is imposed for the sorting of the $\gamma\gamma$ matrix which is localized at the position of one of the surplus spikes in the time spectrum. It is indicated in Fig. 4.2 labeled as *random coincidences gate*. It is used in the sort of the data to construct a $\gamma\gamma$ matrix under the time condition of one γ ray in the beam gate and the second γ ray in the random coincidence gate. The resulting matrix is then subtracted from the bare $\gamma\gamma$ matrix. The effect of this subtraction on a coincidence spectrum gated on the $2_1^+ \rightarrow 0_1^+$ transition is depicted in Fig. 4.7. While the peak of the $2_1^+ \rightarrow 0_1^+$ transition coincident to itself vanishes almost completely, the peaks of the other transitions remain unaltered in shape and intensity.

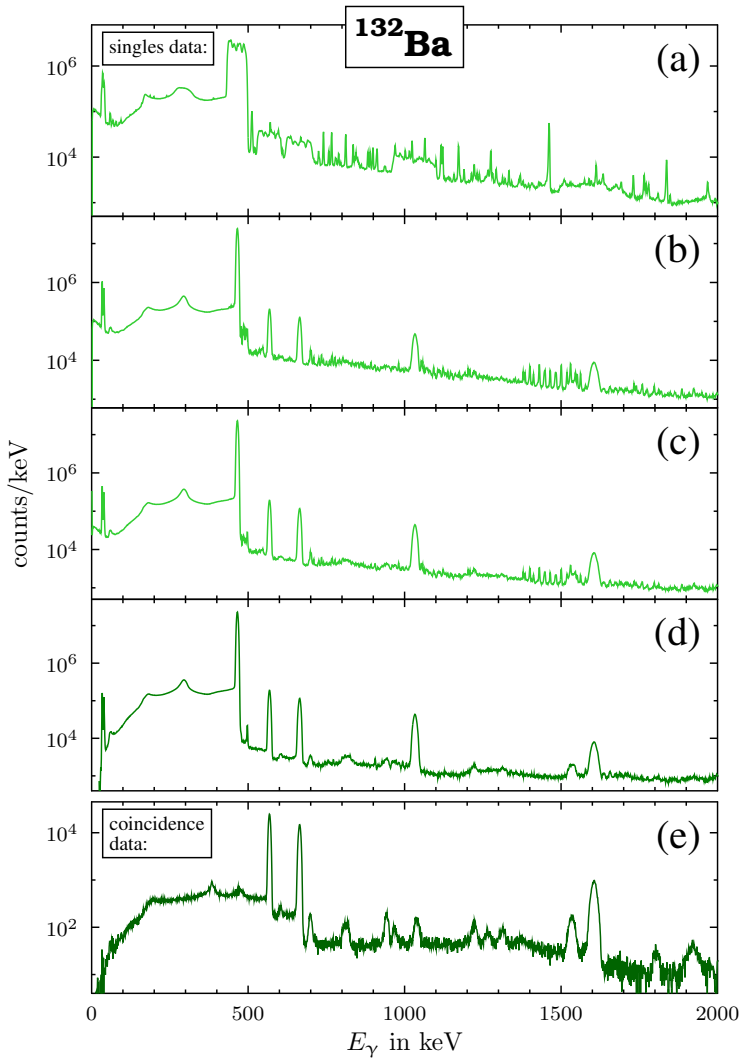


Figure 4.8.: Sum spectrum of all detectors at different stages of the data analysis: (a) raw data without any corrections applied (b) after performing the Doppler correction (c) after applying the beam-gate time condition (d) fully background-subtracted sum spectrum (e) Coincidence spectrum gated on the $2_1^+ \rightarrow 0_1^+$ transition with random-coincidences subtraction applied.

4.2 Angular distribution analysis

The investigation of the angular distribution of γ -ray intensity can yield valuable information on the spins and parities J^π of the states connected by a gamma decay and on the multiplicities involved. In this work the angular distributions are used to determine the multipole mixing ratio δ of a decay. The analysis largely follows the procedure outlined by T. Yamazaki in 1967 [Yam67] and is applied to the decays of higher lying 2^+ states to the 0_1^+ and 2_1^+ states.

The expected size of the effect is of the order of $< 10\%$, a fact that demands a high precision in the determination of the γ -ray intensities as well as of the efficiencies. This, in turn, requires a certain amount of statistics collected for the transitions, which to first order is determined by the absolute value of the ground state transition matrix element of a state and of the branching ratio of the decay channels. In the experiments of this work, however, only the data of ^{154}Sm fulfilled these requirements and allowed for an angular distribution analysis.

Angular distributions

The angular distributions are determined experimentally by the ring-wise evaluation of γ -ray intensities from the data of the ring spectra and from the ring-wise determined detection efficiencies. In their evaluation, however, relativistic effects have to be accounted for that are induced by the in-flight emission of γ rays by nuclei moving at a velocity of $\beta \approx 8\%$. For a physically sensible evaluation the angular distributions have to be determined in the frame of the emitting nucleus rather than in the laboratory frame. The necessary transformations have effects on the angles θ_{Ge} of the HPGe detectors with respect to the beam axis and on the solid angles Ω_{Ge} covered by the detectors, an effect which is usually referred to as the *Lorentz boost*. The effect on the angle is comparatively small – $\approx 1 - 2\%$. The transformation [Stu03] from the laboratory frame $\theta_{\gamma,\text{lab}}$ into the frame of the nucleus $\theta_{\gamma,\text{nuc}}$ is described by

$$\cos \theta_{\gamma,\text{nuc}} = \frac{\cos \theta_{\gamma,\text{lab}} - \beta}{1 - \beta \cos \theta_{\gamma,\text{lab}}}. \quad (4.4)$$

The Lorentz-Boost has a larger effect of the order of $\approx 10\%$ in maximum forward and backward direction. It affects the solid angles covered by the HPGe detectors in the frame of the nucleus. In forward direction they are transformed to larger values, in backward direction to smaller values. Since the detection efficiency is directly proportional to the solid angle covered by the detector, the Lorentz boost

directly affects the γ -ray intensities measured experimentally. The transformation of the Lorentz boost can be described [Stu03] by

$$d\Omega_{\text{nuc}} = \frac{1 - \beta^2}{(1 + \beta \cos \theta_{\text{nuc}})^2} d\Omega_{\text{lab}} . \quad (4.5)$$

Extraction of the multipole mixing ratio δ

The distributions of γ -ray intensities are then used to perform a fit of the standard angular distribution formula, which is an expansion in Legendre polynomials $P_k(\cos \theta)$

$$\begin{aligned} W(\theta) &= A_0 + A_2 P_2(\cos \theta) + A_4 P_4(\cos \theta) \\ &= A_0 (1 + a_2 P_2(\cos \theta) + a_4 P_4(\cos \theta)) , \end{aligned} \quad (4.6)$$

with the expansion coefficients $a_2 = A_2/A_0$ and $a_4 = A_4/A_0$. Since the experiment is a relative measurement, the coefficient A_0 is used only for normalization and is of no particular significance for the further calculations. The coefficients a_k can be written [Yam67] as

$$a_k = \frac{1}{1 + \delta^2} \rho_k(J_i) \left(F_k(J_f \lambda \lambda J_i) + 2\delta F_k(J_f \lambda \lambda' J_i) + \delta^2 F_k(J_f \lambda' \lambda' J_i) \right) , \quad (4.7)$$

where $\rho_k(J_i)$ is a statistical tensor describing the population of the magnetic sub-states m of the initial state. The geometrical factors F_k are tabulated in [Yam67]. The last two terms in Eq. (4.7) vanish in the case of a transition that is pure by definition, in particular for a $2^+ \rightarrow 0^+$ transition, resulting in

$$a_k = \rho_k(J_i) F_k(J_f \lambda \lambda J_i) . \quad (4.8)$$

It is evident from (4.8) that the ρ_k can be derived from the a_k of a ground state transition $2^+ \rightarrow 0^+$. Alternatively, the ρ_k can also be drawn from Coulex calculations [Bau09]. With the knowledge of the ρ_k , the possible combinations of the a_k for a presumably mixed transition $2^+ \rightarrow 2^+$ can be calculated for different values of δ using (4.7). A parametric plot of a_4 against a_2 for $-\infty < \delta < \infty$ results in an angular distribution ellipse of the theoretical expansion coefficients for the $2^+ \rightarrow 2^+$ transition. The values of δ can then be deduced by a comparison of the points of the ellipse with the experimental expansion coefficients a_2 and a_4 of the $2^+ \rightarrow 2^+$ transition. More details of the analysis are given for the analysis of the ^{154}Sm data, cf. 4.4.1.

4.3 Coulex calculations

Other observables in γ ray spectroscopy experiments are transition intensities. Those are extracted in the form of peak areas from the spectra and then corrected for the detection efficiency. Coulomb excitation theory (cf. 3.1) is applied to link these observables with the reduced transition probabilities. The calculations as well as the underlying considerations will be discussed in the following.

General procedure

The Coulomb excitation theory is capable of the description of cross sections $\sigma_{\text{CLX}}(J_i^\pi)$ for the excitation of states J_i^π . An equivalent to the Coulex cross section that is experimentally accessible in γ -ray spectroscopy experiments is the so-called *yield* $Y(J_i^\pi)$ of a state J_i^π . It is a measure of how often a state has been populated by means of Coulomb excitation and can be calculated from the sum of the γ -ray intensities depopulating a state subtracted by the intensities of feeding transitions. In the course of this work the yields of the observed states are normalized to $Y(2_1^+)$ of the first excited state, resulting in relative yields, which are equal to the relative Coulex cross sections of the experiment

$$Y_{\text{rel}}(J_i^\pi) = \frac{Y(J_i^\pi)}{Y(2_1^+)} = \frac{\sigma_{\text{CLX}}(J_i^\pi)}{\sigma_{\text{CLX}}(2_1^+)}. \quad (4.9)$$

An exception to this normalization to the 2_1^+ state had to be made in the analysis of the ^{154}Sm data, cf.4.4.1. It is the purpose of the Coulex calculations to find a set of electromagnetic transition matrix elements that will result in the experimentally observed relative Coulex cross sections. Several codes are on the market that are capable thereof. For this work, the standard Coulex code CLX [Owe, Owe80] has been used. It is based on the original code presented by Winther and deBoer [Win66].

For the execution of the code, an input file has to be prepared containing the information on the states and the transitions. An example of an input file can be found in appendix A. The input file is divided into three main parts. In the first section of the file, general information on the calculation to be performed is given, e.g. input and output specifications, the desired accuracy and the nuclei involved. The code originally was designed for experiments in ordinary kinematics. To be able to compute also Coulex reactions in inverse kinematics, the proton numbers Z_p and Z_t of projectile and target nuclei have to be interchanged in the file. The second part of the file contains a numbered list of the states to be calculated. The states have to be specified with their excitation energy, spin, and parity. The numbering of the states is again used in the third part of the file for the specification of

the transition matrix elements in terms of their value and the multipolarity of the transition. In practice, only electric transitions play a role for the sub-Coulomb barrier excitation process. The ratio of matrix elements describing the depopulation of the same initial state J_i is constrained by the branching ratio of the γ decays via the relation

$$\begin{aligned} \frac{I_1}{I_2} &= \frac{\Gamma_1}{\Gamma_2} = \frac{c_{\sigma_1 \lambda_1} \left(\frac{E_{\gamma 1}}{\text{MeV}} \right)^{2\lambda_1+1} \cdot B(\sigma_1 \lambda_1; J_i \rightarrow J_{f,1})_{\downarrow}}{c_{\sigma_2 \lambda_2} \left(\frac{E_{\gamma 2}}{\text{MeV}} \right)^{2\lambda_2+1} \cdot B(\sigma_2 \lambda_2; J_i \rightarrow J_{f,2})_{\downarrow}} \\ &= \frac{c_{\sigma_1 \lambda_1} \left(\frac{E_{\gamma 1}}{\text{MeV}} \right)^{2\lambda_1+1} \cdot |\langle J_{f,1} \| M(\sigma_1 \lambda_1) \| J_i \rangle|^2}{c_{\sigma_2 \lambda_2} \left(\frac{E_{\gamma 2}}{\text{MeV}} \right)^{2\lambda_2+1} \cdot |\langle J_{f,2} \| M(\sigma_2 \lambda_2) \| J_i \rangle|^2}, \end{aligned} \quad (4.10)$$

which can be inferred from $I_{\gamma} \propto \Gamma_i$ and equations (3.22) and (3.23), cf. 3.2.2.

The code CLX is capable of the calculation of Coulex cross sections for a given set of transition matrix elements. For the determination of a set of matrix elements from the cross sections, i.e. the inverse calculation, a fit of the matrix elements has to be performed that reproduces the experimental relative cross sections. This fit has been done manually. The decision not to have the fit performed by a computer program has been made in order to have as much control and insight over the calculations in this key step of the analysis as possible.

Among the nuclear matrix elements, the diagonal matrix elements have to be treated separately. Those correspond to the electric quadrupole moment of the nucleus in the state. In the calculations, quadrupole moments that have been known from previous experiments have been taken from the literature. For the rest of the states the rotational limits of (2.18), i.e. $Q_0^2 < 16\pi/5 \cdot B(E2; 2_1^+ \rightarrow 0_1^+)/e^2$, have been used to estimate the uncertainty induced by the value of Q . In the setup of inverse kinematics on a light target material this is a second order effect and induces uncertainties on the order of $\leq 3\%$.

As a consequence of the choice of the light target material of Carbon, the Coulomb excitation of the projectile nuclei is almost entirely dominated by one-step excitations. This fact significantly facilitates the analysis in several ways. First, it assures that the interference between states that are predominantly excited directly from the ground state is only a second order effect or even less. This allows to perform the fits of the decay matrix elements for each state individually without significant influence on the results of the other states. It turned out during the calculations that this holds true for those states that are connected to the ground state via a non vanishing matrix element, such as the 2^+ states, unless they are connected by a strongly collective $E2$ transition to, e.g., an excited 0^+ state. However,

the matrix elements of states that are not (predominantly) excited directly from the ground state are strongly affected by transitions to other states in the calculation and by the choice of the signs of the matrix elements, e.g. the 3_1^+ and 4_2^+ states. For those states, no reliable results can be obtained, although it is important to include those in the CLX calculations. Second, the nearly complete independence of the results on the treatment of other states in the calculation allowed for a treatment of only a subset of the observed states in the calculations without significant effects on the results. It is only due to this feature of the calculations that an analysis of the Pt isotopes with their extensive level scheme has been possible using the present method. Over the course of the calculations this independence had been tested and verified. All states that do have a significant impact on the results of the other states have been included in the calculations, in particular the afore-mentioned 3_1^+ states, since they are an important part of the low-lying collective structures.

Signs of matrix elements

The results on the matrix elements for the depopulation of certain states depend very sensitively on the choice of the relative signs of the matrix elements, in particular for those states that are not connected directly to the ground state by a ground state transition, and, thus, can only be populated by multiple Coulex reactions. This applies especially to 4^+ and 0^+ states, but it can also occur in the case of individual 2^+ states for which the ground state transition matrix element is a lot smaller than the matrix element to the 2_1^+ state, for instance. Nevertheless, not all possible combinations of signs result in different values for the matrix elements. The effect rather depends on the sign of a closed loop of transitions, e.g. in the case of the 2_2^+ state the product $\text{sgn}(\langle 2_2^+ | E2 | 2_1^+ \rangle) \times \text{sgn}(\langle 2_1^+ | E2 | 0_1^+ \rangle) \times \text{sgn}(\langle 0_1^+ | E2 | 2_2^+ \rangle)$. This also implies that for states that predominantly are depopulated via a single decay channel, a sign change does not affect the results, which is of particular importance for the states of the ground state band. The effect induced by sign changes on the resulting absolute values of the matrix elements can have a huge impact on the results, as it was observed in the case of the 0_2^+ state in ^{194}Pt , for instance (cf. Table 4.2).

In the analyses this problem has been attacked by two different approaches. The first possibility is to find a set of physically motivated signs. One possibility, though not chosen in the course of this work, might be the adoption of signs from a theoretical calculation, e.g. from the IBM. In the analysis of the ^{154}Sm experiment, the deduction of relative signs from the Alaga rule (Eq. (2.21)) was applied instead, an ansatz that is only applicable in rotational nuclei, where the Alaga rule is valid. Details of this analysis are described in chapter 4.4.1 and in the corresponding publication [Möl12].

For the other nuclei, a new approach for the treatment of the signs has been developed in this work. It was tried to find a valuable estimate of the influence of sign changes on the results for the matrix elements. For this purpose, numerous different CLX calculations have been performed in which the absolute values of all matrix elements have been kept constant while the signs have been varied using different combinations. The results on the Coulomb excitation yields in these test-calculations have been compared. The sign-combinations for minimal and maximal results on the yield of a given state have been taken to perform the Coulex fits. It has been found that in some cases the minimal and maximal results for the matrix elements of the depopulation of a given state have been obtained from sign combinations that in the test-calculations led to extremal values of the yield of the 2_2^+ state instead of the investigated state itself.

The results of the CLX calculations using those sign combinations that led to extremal values in the test-calculations have been assumed to represent the upper and lower limits for the systematic uncertainty induced by the sign effect. They have been, thus, adopted as the limits of the systematic uncertainty statement in the results. The mean value of these two limits has been adopted as the result for the matrix element. Not until then the determination of the statistical uncertainty was performed, which comprises the uncertainty induced from the uncertainties in the relative yields, the normalizing matrix element of the $2_1^+ \rightarrow 0_1^+$ transition, and the effect of the quadrupole moments. This treatment of the uncertainties results in a mean value with specifications of the systematic uncertainty and the statistical uncertainty, cf. Tables 4.2, 4.3, 4.4, and 4.5.

Energy loss in the target

The calculations of the Coulex cross sections are highly sensitive on the kinetic energy of the projectile ions. However, in the passage through the target they are object to several interactions and, thus, to an energy loss that can sum up to a total of 70 MeV. As a consequence, a discrete kinetic energy for which the excitation occurs, can not be determined. For the calculation of the energy loss in the target it is important to take into account that in some experiments the target had been mounted on the Gammasphere target ladder, which is tilted at an angle of 37° . This increases the effective thickness of the target by a factor $\cos^{-1}(37^\circ) = 1.252$.

There are different ways to deal with the energy loss of the ions in the target. For the analysis of the ^{154}Sm data an average beam energy in combination with a standard deviation has been deduced and used in the CLX calculations. The big disadvantage of this method is the large uncertainty in the results, that could

be tolerated in this case because of other sources of large uncertainties, like the normalization to a higher lying state, for instance, cf. 4.4.1.

For the $^{130,132}\text{Ba}$ and $^{194,196}\text{Pt}$ analyses the energy loss was dealt with by a virtual segmentation of the target depth into 10 layers, for which the kinetic energies of the projectile ions have been calculated. For each of the virtual layers individual CLX calculations have been performed using the respective kinetic energies of the projectiles in the layers. The final result was derived from the average cross section of the 10 layers. This is a good approximation since the Coulex cross sections scale linear with the beam energy and the beam energy scales linear with the penetration depth in the target to first approximation. A large drawback of this method, however, is the 10-fold increase in time consumption of each calculation step. For the uncertainties of the calculations, the uncertainties in the results of a single slice have been used.

4.4 Results

The analysis of the data has been performed according to the steps outlined in the preceding sections. However, the analyses have been performed one after the other, so that certain features have been subject to progress throughout the course of the present work. In particular, this applies to the treatment of the coincidence data of the experiments and to the treatment of the signs of the matrix elements during the calculations. In the following, the analyses of the five separate experiments will be individually discussed in more detail. This discussion will follow the chronological sequence in which the data sets have been analyzed, beginning with the ^{154}Sm experiment.

4.4.1 ^{154}Sm

An analysis of this data set had previously been started in the framework of a Master's thesis [Möl09]. In that analysis, the normalization of the γ -ray intensities had been performed with respect to another state. The present work represents a re-analysis of this data set.

Chronologically, the ^{154}Sm data set has been the first data set to be analyzed in the framework of this thesis. Therefore, some of the features of the analysis discussed above and applied in the analysis of the Ba and Pt isotopes are different in ^{154}Sm .

To begin with, the sort of the data has not been performed using the GSSort framework. Instead, the MTsort package [Cre] using the MIDAS data acquisition and sort system [Dar] has been used. This sorting code had already been

utilized for the analyses of several previous experiments in the same technique [Ahn09, Coq10, Rai06]. Within the scope of this sorting code no subtraction of random coincidences from the $\gamma\gamma$ -matrix had been implemented. This feature was introduced later in the ROOT-based analysis of the data of the Pt isotopes, driven by the need of a reliable analysis based on coincidence data due to the large number of transitions in these experiments. As a consequence, the coincidence spectra of ^{154}Sm still contain peaks corresponding to random coincidences. The Doppler-corrected, background-subtracted singles sum spectrum of all detectors is shown in Fig. 4.10, and, together with an example of the coincidence data of the data set, in appendix B.3.

The coincidence data was used mostly for the reconstruction of the level scheme of excited states from the energies of the observed γ rays and the coincidence relations among them. The level scheme of the excited states is shown in appendix B.3. Among the excited states there are the states of the ground-state band up to the 10_1^+ state. In the first excited $K = 0$ band the states 0_2^+ , 2_2^+ , and 4_2^+ have been excited. The first three states of the γ band, namely the 2_4^+ , 3_1^+ , and 4_3^+ states have been identified from the data as well. Besides these states, on which the following discussion will be centered, also several other states have been populated. These include the first states of two bands on top of the 1_1^- and 1_2^- states.

Additional excited states identified from the data lie outside this band scheme and include the 2_3^+ state at 1286 keV, a 3^+ state at 1707 keV, a state assigned $J^\pi = 2^+, 3$ at 1815 keV, a $J^\pi = 1^-, 2^+$ state at 2015 keV, and a $J^\pi = 1, 2^+$ state at 2139 keV. (All J^π assignments are taken from [Rei09].)

The quantitative analysis of the data, namely the derivation of the transition intensities, was to a large extent performed based on the data of the singles spectrum. In cases where the intensity of a transition had to be determined from the coincidence data, the uncertainty was chosen appropriately large enough to compensate for the random coincidences that remained in the spectra.

Unlike previous experiments performed by our group, e.g. [Ahn09, Coq10, Rai06], and different from the Pt and Ba analyses (4.4.2 and 4.4.3) as well, in the ^{154}Sm analysis a normalization of the γ -ray intensities and of the yields of the states to the 2_1^+ state has not been possible. This was mainly due to the small excitation energy of the 2_1^+ state of only 82 keV. In this energy region, the Gammasphere detection efficiency usually exhibits a sharp decrease due to the use of filters for low-energy γ rays and X-rays. At the time of the experiment, a ^{182}Ta calibration source was not available so that the description of the γ -ray detection efficiency in the energy region below its maximum at approximately 250 keV could not be performed using the data points of the ^{152}Eu and ^{56}Co calibration sources. It should be noted, however, that even an efficiency calibration comprising ^{182}Ta

data, as it has been done for the Pt experimental campaign, does not allow for an accuracy in the determination of the efficiency in this energy region comparable to the accuracy achieved for the normalization in the Pt and Ba analyses.

In order to perform an analysis of the ^{154}Sm data, the 2_4^+ state at 1440 keV has been chosen to serve as a normalization during the analysis. Details on the γ -ray intensities and on the yields of the states in this experiment relative to $Y(2_4^+)$ are tabulated in Tables B.5 and B.6.

The lifetime of the 2_4^+ state had been measured previously using the DSAM technique [Krü99] to $\tau(2_4^+) = 0.61(4)$ ps. The state predominantly decays via three transitions of 1440, 1358, and 1173 keV to the 0_1^+ , 2_1^+ , and 4_1^+ states, respectively. The use of this state as normalization required exact knowledge of the properties of its γ decays. Since the 2_4^+ state is one of the states populated most strongly in the experiment, the intensities of the decays and, hence, the branching ratios of the decay channels, have been determined with high accuracy. The relative intensities of the transitions determined from the data are tabulated in Table 4.1. For the determination of the intensity of the $2_4^+ \rightarrow 0_1^+$ transition, the $3^+(1707 \text{ keV}) \rightarrow 4_1^+$ transition, residing at the same energy of 1440 keV, had to be taken into account. The intensity of this transition has been estimated from the peak area of the 1440-keV peak in the spectrum coincident to the $4_1^+ \rightarrow 2_1^+$ transition and subtracted from the intensity of the 1440-keV peak in the singles data. For the calculation of the Coulex yield of the state, the only feeding from higher-lying states has been identified as the $1815 \rightarrow 2_4^+$ transition at an energy of 375 keV and has been taken into account.

An angular distribution analysis, outlined in 4.2, has been performed to determine the multipole mixing ratio δ of the 1358 keV $2_4^+ \rightarrow 2_1^+$ transition. Due to low sensitivity on the expansion coefficient a_4 , two possible resulting values for the mixing ratio have been $\delta = -19(10)$, which corresponds to a nearly pure $E2$ transition, or $\delta = -0.51(7)$, which corresponds to a 21(5)% $E2$ contribution to the transition. A figure of the angular distributions and of the angular distribution ellipse is shown in Figs. 4.9 and B.10b. The ambiguity of the results has been solved by a comparison of the resulting $B(E2)$ values with the predictions of the Alaga rule [Ala55], which can be expected to apply in the nucleus ^{154}Sm regarding its rigid-rotor properties. According to the Alaga rule, the ratio

$$\frac{B(E2; 2_K^+ \rightarrow 2_1^+)}{B(E2; 2_K^+ \rightarrow 0_1^+)} = 1.43, \quad \text{for } K = 0, 2, \quad (4.11)$$

where K denotes the K -quantum number of the initial state. For the decay of the 2_4^+ state with $K = 2$, this ratio calculated from the experimental values is either 1.66(2) for $\delta = -19(10)$ or 0.34(3) for $\delta = -0.51(7)$. The first value is closer

to the prediction of the Alaga rule and therefore $\delta = -19(10)$ is adopted for the further calculation. Analogous to this, the multipole mixing ratio δ of the $2_2^+ \rightarrow 2_1^+$ transition has been determined. Again, two possible values resulted from the angular distribution analysis, namely $\delta = -30(21)$ and $\delta = -0.48(2)$. The angular distributions and the angular distribution ellipse leading to these results are depicted in Fig. B.10a. The relation of (4.11) also applies to the $K = 0$ 2_2^+ state. The ratio of experimental transition strengths for the decays of this state are either 2.25(40) for $\delta = -30(21)$ or 0.47(9) for $\delta = -0.48(2)$. The value for the nearly pure $E2$ transition is closer to the value of the Alaga rule and, thus, for the $2_2^+ \rightarrow 2_1^+$ transition $\delta = -30(21)$ is adopted for the further calculations.

In the CLX calculation of the electromagnetic transition matrix elements, the high sensitivity of the results on the signs of the matrix elements of the transitions had to be addressed. Unlike in the Ba and Pt analyses, in ^{154}Sm this issue also applied for the normalizing state 2_4^+ . Again, the Alaga rule was utilized. Using it in its square rooted version,

$$\text{sgn} \left(\frac{\langle J_f || E2 || J_i \rangle}{\langle J_{f'} || E2 || J_i \rangle} \right) = \text{sgn} \left(\frac{\langle J_i K_i 2 \Delta K | J_f K_f \rangle}{\langle J_i K_i 2 \Delta K | J_{f'} K_{f'} \rangle} \right), \quad (4.12)$$

it can be used to deduce the relative signs of inter-band transitions from a state J_{i,K_i}^π into different states J_{f,K_f}^π and $J_{f',K_{f'}}^\pi$ of the same band with $K_f = K_{f'}$. In (4.12), the coefficients in angle brackets on the right-hand side denote Clebsch-Gordan coefficients. The ground state transition matrix elements of each state have been chosen to be positive, the relative signs of the other decay matrix elements have been deduced from (4.12).

In conclusion, the exact knowledge of the branching ratios of the decays of the 2_4^+ state, the mixing ratio of the $2_4^+ \rightarrow 2_1^+$ transition, the signs of the matrix elements, and the previously deduced lifetime allowed for the calculation of the transition strengths of the decays of the 2_4^+ state, cf. Table 4.1. In the CLX calculations these result in a Coulex cross-section of $\sigma(2_4^+) = 2.8(3)$ mb that defines the absolute scale for the calculation of the other states using CLX.

Using this setup the matrix elements for the states of the ground band and of the $K = 0$ band have been included into the CLX calculation, cf. 4.3. Since the yields of the 2_1^+ and 4_1^+ states in the ground-state band could not be determined experimentally, the adopted values for the intra-band transition strengths from the Nuclear Data Sheets [Rei09] have been used. Also adopted values for the quadrupole moments $Q(2_1^+) = -1.87(4)$ eb and $Q(4_1^+) = -2.2(8)$ eb have been included into the calculations. For the rest of the states the quadrupole moment of the 2_1^+ state has been used as a first approximation. The intra-band matrix elements for transitions within the beta band do not have a significant impact on the

results of the calculations. This has been checked by performing CLX calculations using different values for these transitions. For the final calculations, these values have been chosen according to the predictions of the calculations in [Pie04] as $B(E2; 4_2^+ \rightarrow 2_2^+) = 234$ W.u. and $B(E2; 2_2^+ \rightarrow 0_2^+) = 165$ W.u.. The results of the calculations are tabulated in Table 4.1.

The CLX calculations (cf. Appenix A) resulted in a set of transition matrix elements for the decays of the states of the $K = 0$ band, namely of the 0_2^+ state at 1099 keV, the 2_3^+ state at 1178 keV, and the 4_2^+ state at 1338 keV. These results and their implications on the assignment of the $K = 0$ band as a β band will be discussed in the framework of the confined- β -soft rotor model (CBS, cf. 2.4.3) in chapter 5.3.

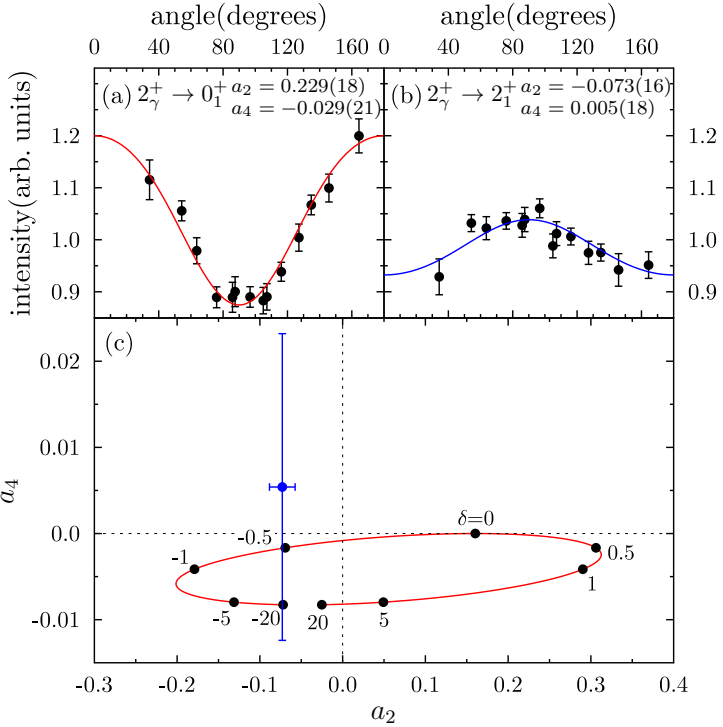


Figure 4.9.: Angular distribution analysis of the $2_4^+ \rightarrow 2_1^+$ transition in ^{154}Sm . The expansion coefficients of the ground-state transition (a) are used to calculate the statistical tensors of the population of m -substates of the 2_4^+ state. From those, the angular distribution ellipse (c) is calculated. The value of δ results from a comparison to the expansion coefficients of the angular distribution of the $2_4^+ \rightarrow 2_1^+$ transition (b).

Table 4.1.: Results of the analysis of the ^{154}Sm data

E_{level} (keV)	J_i^{π}	J_f^{π}	E_{γ} (keV)	I_{γ}	Y_{rel}	δ	sgn	$B(E2)_{\downarrow}$ (W.u.)	Lit. [Rei09] (W.u.)
82	2_1^+	0_1^+	82	^a	^a		+	176(1) ^d	176(1)
267	4_1^+	2_1^+	185	^a	^a		+	245(6) ^d	245(6)
	0_1^+		267	not observed			+	79(3) ^d	79(3)
544	6_1^+	4_1^+	277	$3.1(2) \times 10^3$	$6.19(55) \times 10^{-1}$		+	289(8) ^d	289(8)
903	8_1^+	6_1^+	359	144(8)	$2.54(22) \times 10^{-2}$		+	319(17) ^d	319(17)
1099	0_2^+	2_1^+	1017	911(15)	$1.89(5) \times 10^{-1}$		+	11.2(21)	12(3)
1178	2_2^+	4_1^+	911	627(16) ^b	$4.33(9) \times 10^{-1}$	-30(21)	+	1.32(15)	<2.4
		2_1^+	1096	870(16)		-0.48(2) ^c	-	0.72(9)	<1.3
1338		0_1^+	1178	557(16)			+	0.32(4)	<0.58
		6_1^+	795	34(3)	$6.93(26) \times 10^{-2}$		+	0.66(21)	
		4_1^+	1071	131(9)			-	0.57(18)	
		2_1^+	1256	164(6)			+	0.32(11)	
1440	2_4^+	4_1^+	1173	139(10)	$1.00(2) \times 10^0$		+	0.36(5)	0.48(7)
		2_1^+	1358	2582(61)		-19(10)	+	3.2(3)	
		0_1^+	1440	2076(53)		-0.51(7) ^c	+	0.65(6) ^c	
							+	1.9(2)	2.13(16)

^aThe intensity could not be determined with sufficiently high accuracy.

^btransition could not be resolved from transitions nearby; value calculated with branching ratio from Nuclear Data Sheets [Rei09].

^cdisfavored alternative due to Alaga-rule constraint (see text).

^dAdopted values from Nuclear Data Sheets have been used in the calculation.

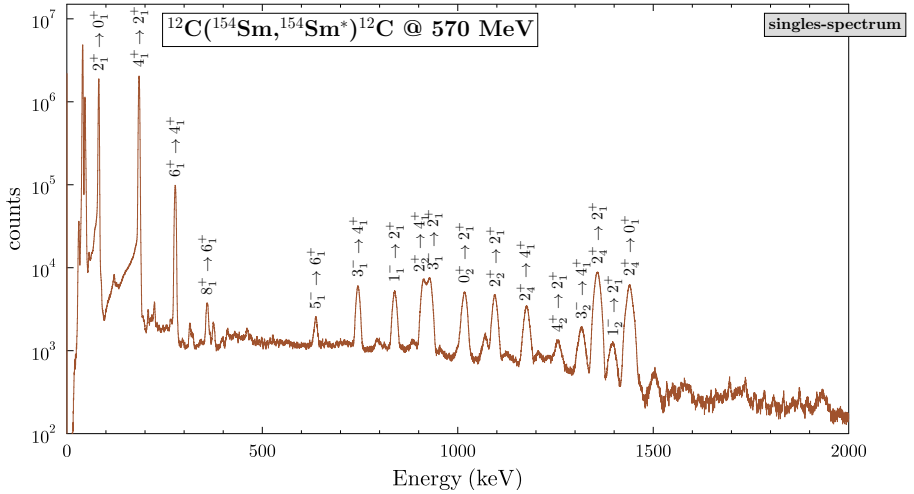


Figure 4.10.: Singles spectrum of the ^{154}Sm experiment. A more detailed image and coincidence data is shown in appendix B.3.

4.4.2 $^{194,196}\text{Pt}$

The analysis of the Pt data has been complicated by a large number of excited states and, thus, a large density of transitions in the spectra. Given the limited resolution in the spectra, an analysis based on the singles data of the experiment would have been a hopeless endeavor. Therefore it had been an urgent necessity to be able to perform an analysis based on the coincidence data of the experiment also in terms of quantitative measures. An issue that hindered such an approach in previous experimental analyses had always been the presence of random coincidences in the spectra. In order to overcome this obstacle, the sorting process of the raw data was extended by a mechanism to subtract these artifacts from the coincidence data. The method is described in 4.1.

^{194}Pt analysis

The Doppler-corrected, background-subtracted sum spectrum of the ^{194}Pt experiment and the coincidence spectrum gated on the $2_1^+ \rightarrow 0_1^+$ transition are shown in Fig. 4.11. Images of the spectra in more detail as well as more examples of the coincidence spectra are depicted in appendix B.4. Under the given circumstances the reconstruction of the level scheme of ^{194}Pt based on the observed transitions had been the biggest challenge in the analysis of the data set. To maximize the statistics for this qualitative part of the analysis the coincidence data of both experimental runs (- γ -ray singles and multiplicity ≥ 2) have been used. The list of observed transitions as well as a complete level scheme of the identified transitions and the excited states in this experiment are shown in appendix B.4.

The identified excited states in the ^{194}Pt experiment comprise the states of the ground-state band up to the 6_1^+ state at 1411 keV. The low-lying states also contain a band-like structure based on the 2_2^+ state including the 3_1^+ and 4_2^+ states. The excitation of the 0_2^+ state at 1267 keV and the 0_4^+ state at 1547 keV has been observed. The third 0^+ state at 1479 keV, however, has not been observed in the experimental data. This state has previously been reported in several experiments, e.g. in ^{194}Ir β decay [Cle76], in (n, n' γ) [Fil81], (p, d) [Ber81], and (p, t) [Dea79] reactions. Also its $E0$ ground-state transition is given [Kib05]. The data comprise several states with $J^\pi = 2^+$ assignment, e.g. states at 1622 keV and 1670 keV as well as states with a possible $J^\pi = 2^+$ assignment, e.g. the states at 1816 keV, 2004 keV, and 2287 keV. A state at 2072 keV excitation energy has been populated. For this state, no J^π assignment has been made previously [Sin06]. In the course of this work, this state is referred to with the label J^π and will be treated during the analysis like a 2^+ state. The decays of five states with a $J^\pi = 3^-$ assignment

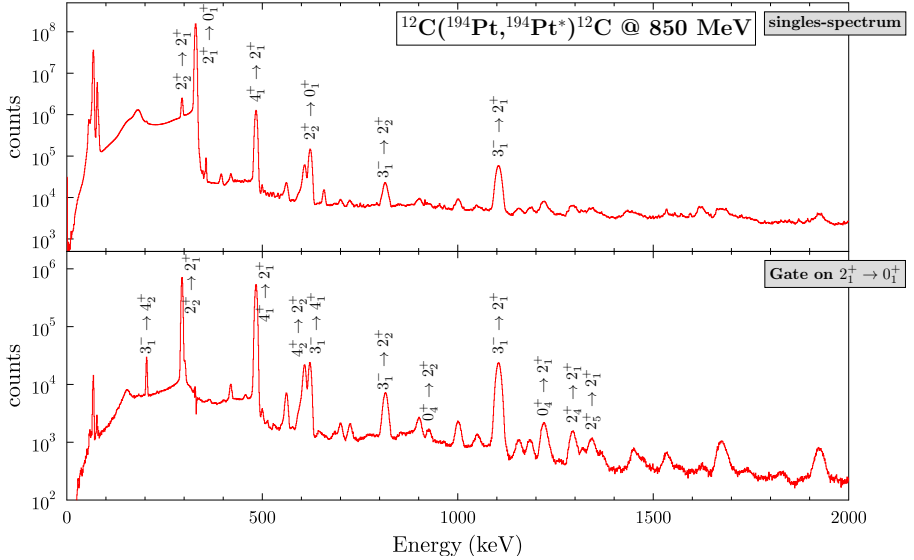


Figure 4.11.: Singles spectrum and spectrum gated on the $2_1^+ \rightarrow 0_1^+$ transition of the ^{194}Pt experiment. More detailed images of the spectra are depicted in appendix B.4.

have been observed, namely the states at energies of 1432 keV, 1737 keV, 2154 keV, 2246 keV, and 2546 keV.

Several additional states have been identified, see Fig. B.14 for details.

Some peaks in the spectra could not be assigned. In the singles spectrum, the peaks at 394 keV and 657 keV could not be identified. The 394-keV peak shows no coincidence relation to other transitions in the data. The 657-keV peak appears again in the gate on the $4_1^+ \rightarrow 2_1^+$ transition. It exhibits a smaller width than expected. It was concluded that these two peaks do not stem from the excitation of ^{194}Pt . Their origin, however, could not be resolved. Some peaks observed in the coincidence data could not be identified either due to a general limitation in the analysis of the coincidence data: Imposing a gate in the $\gamma\gamma$ -coincidence matrix on a transition with a relatively small intensity (compared to the $2_1^+ \rightarrow 0_1^+$ transition) can result in very small peaks in the resulting coincidence spectrum. The usual way to identify the placement of one of these transitions within the level scheme is, in return, to set a gate on the transition in question. If the respective transition,

however, is only of very small intensity, the resulting coincidence spectrum is highly unlikely to contain conclusive information. This can be attributed to the high density of transitions throughout the entire energy range of the experiment. A gate on a very weak transition will almost inevitably also contain further – presumably stronger – transitions.

The γ -ray intensities of the identified transitions have been determined from the singles spectrum and in most cases from the coincidence spectra. For this quantitative part of the data analysis, the singles and coincidence data only from the first experimental run using a γ -ray singles trigger has been used. The peak areas deduced from the coincidence spectra have been normalized to the values from the singles spectrum by using large peaks as normalization. From the γ -ray intensities of the transitions the yields Y of the states have been deduced and then normalized to the yield $Y(2_1^+)$. The intensities of the transitions and the deduced yields of the states are tabulated in detail in appendix B.4.

Based on the yields determined from the spectra a CLX calculation has been performed as it is outlined in 4.3. The absolute scale of this calculation has been set by the adopted value of $B(E2; 2_1^+ \rightarrow 0_1^+) = 49.2(8)$ W.u. [Sin06]. In this calculation, the states of the ground state band, the 2_2^+ , 3_1^+ , 4_2^+ , 0_2^+ , 2_3^+ , 0_4^+ , 2_4^+ , and 2_5^+ states have been included. The results for the 3_1^+ and 4_2^+ states are highly sensitive to the choice of signs of matrix elements. The results for their transition matrix elements are not conclusive and are, thus, not given. The 0_3^+ state has also been included even though based on an upper-limit estimate of its yield. For the CLX calculation of the excitation process of the 4_1^+ state, an $E4$ transition of $B(E4; 4_1^+ \rightarrow 0_1^+) = 4.07 \times 10^{-3} e^2b^4$ [Set91] has been included into the calculation. However, its effect on the result is only small. The results of the CLX calculations on the ^{194}Pt experiment are given in Table 4.2 and are shown in Fig. 5.9.

The uncertainties of the resulting transition strengths are given as statistical uncertainty and, if a second uncertainty is given, systematic uncertainty. The systematic uncertainty results from the sensitivity of the resulting matrix elements on the choice of the signs of the matrix elements, cf. 4.3. For the decays of the 0_2^+ state, the systematic uncertainty is too large to be subsumed in one value. Therefore, the range of the possible values is given.

The results of the other states will be discussed with respect to the $O(6)$ symmetry of the Interacting Boson Model in 5.2.2.

Table 4.2.: Results of the analysis of the ^{194}Pt data

E_{level} (keV)	J_i^{π}	J_f^{π}	E_{γ} (keV)	I_{γ}	Y_{rel}	δ	$B(E2)_{\downarrow}$ (W.u.) ^a	Lit. [Sin06] (W.u.)
328	2_1^+	0_1^+	328	100000(2742)	1.0000(28)		$49.2(8)^b$	$49.2(8)$
622	2_2^+	2_1^+	294	9307(51)	$9.13(7) \times 10^{-3}$	$+15(2)^f$	$65.0(30)_{\text{stat}}(40)_{\text{sys}}$	$89(11)^g$
		0_1^+	622	1274(26) ^c			$0.21(1)_{\text{stat}}(1)_{\text{sys}}$	$0.29(4)^g$
811	4_1^+	2_1^+	483	12993(62)	$1.153(8) \times 10^{-2}$		$68.7(29)_{\text{stat}}(20)_{\text{sys}}$	$85(5)^g$
922	3_1^+	2_1^+	301	280(7)	$9.07(98) \times 10^{-5}$			
		2_1^+	594	68(4)				
1267	0_2^+	2_1^+	645	17.0(7)	$2.44(7) \times 10^{-5}$		$2.12(30)_{\text{stat}} - 44.9(24)_{\text{stat}}^e$	$8.4(19)$
		2_1^+	938	8.4(4) ^c			$0.160(23)_{\text{stat}} - 3.40(10)_{\text{stat}}^e$	$0.63(14)$
1411	6_1^+	4_1^+	600	127(6)	$1.21(6) \times 10^{-4}$		$92.3(81)_{\text{stat}}$	$67(21)$
1432	3_1^-	4_1^+	203	243(29)	$2.66(5) \times 10^{-3}$			
		4_1^+	621	797(39)				
		2_1^+	810	165(6) ^c				
1479	0_3^+	2_1^+	1104	2039(10)			$B(E3)_{\downarrow} = 7.46(41)_{\text{stat}}(11)_{\text{sys}}$	$5.7(10)$
		0_1^+	1432	67(6) ^c				
1479	0_3^+	2_1^+	1150	< 2.3	$< 2.21 \times 10^{-6}$		< 0.12	

to be continued

Results of the analysis of the ^{194}Pt data (continued)

E_{level} (keV)	J_i^π	J_f^π	E_γ (keV)	I_γ	Y_{rel}	δ	$B(E2)_\downarrow^a$ (W.u.)	Lit. [Sin06] (W.u.)
1512	2_3^+	0_2^+	245	$1.74(15)^c$	$1.07(3) \times 10^{-4}$		$85(24)_{\text{stat}}(34)_{\text{sys}}$	
	3_1^+	3_1^+	589	28(1)			< 24	
	2_2^+	2_1^+	889	17(1)		$+1.5(4)^f$	$0.91(29)_{\text{stat}}(37)_{\text{sys}}$	
	2_1^+	2_1^+	1183	67(2)		$+1.32(9)^f$	$0.79(20)_{\text{stat}}(32)_{\text{sys}}$	
	0_1^+	0_1^+	1512	$4.5(12)^c$			$0.0244(25)_{\text{stat}}(99)_{\text{sys}}$	
1547	0_4^+	2_2^+	925	50(2)	$2.11(4) \times 10^{-4}$		$14.7(11)_{\text{stat}}(22)_{\text{sys}}$	14.3(14)
	2_1^+	2_1^+	1218	171(3)			$12.7(8)_{\text{stat}}(19)_{\text{sys}}$	14.1(12)
1622	2_4^+	3_1^+	699	14(1)	$3.74(10) \times 10^{-4}$		$0.81(11)_{\text{stat}}(8)_{\text{sys}}$	
	2_2^+	2_1^+	1000	142(4)		$+1.4(-5)^f$	$0.90(24)_{\text{stat}}(9)_{\text{sys}}$	
	2_1^+	2_1^+	1293	101(2)		$-0.9(1)^f$	$0.120(12)_{\text{stat}}(18)_{\text{sys}}$	
	0_1^+	0_1^+	1622	$135(10)^c$			$0.115(9)_{\text{stat}}(11)_{\text{sys}}$	
	2_5^+	2_2^+	1048	56(2)	$1.60(2) \times 10^{-4}$	$< 0.8^f$	< 1.0	
1670	2_1^+	2_1^+	1342	97(2)		$-0.26(6)^f$	$0.073(31)_{\text{stat}}(9)_{\text{sys}}$	
	0_1^+	0_1^+	1670	$13.5(7)^d$			$0.0515(45)_{\text{stat}}(84)_{\text{sys}}$	

^aUncertainties are given as (stat.) (sys.). Systematical uncertainties stem from sensitivity to different sets of signs.

^bAdopted value from Nuclear Data Sheets [Sin06].

^cIntensity deduced from branching ratio given in Nuclear Data Sheets.

^dIntensity deduced by subtracting the intensity of the transition $2072 \rightarrow 2_2^+$ from their common peak.

^eLarge fluctuations in the results due to strong sensitivity of the CLX result on the signs of the transition matrix elements.

^fValues for δ taken from Nuclear Data Sheets.

^gcf. Fig. 5.10

In the analysis of the data of the ¹⁹⁶Pt experiment, the complexity of the level scheme and the large number of observed transitions have been the biggest challenges. However, the know-how gained in the analysis of the ¹⁹⁴Pt experiment could also be applied in the analysis of ¹⁹⁶Pt. In the sorting of the data the previously developed tool for the subtraction of random, unphysical coincidences has also been deployed in the case of ¹⁹⁶Pt. In general, the analysis followed the procedure outlined in 4.1 and 4.3. Again, the reconstruction of the level scheme from the experimental data has been a challenge due to the large number of transitions and of the limited resolution of the setup. The Doppler-corrected, background-subtracted singles sum spectrum and a coincidence spectrum are shown in Fig. 4.12. Images of the spectra in more detail can be found in appendix B.5.

The level scheme of excited states has been reconstructed from the coincidence data. The analysis of the level scheme has been based on the coincidence data from both experimental runs, namely the run with the trigger set to singles mode and set to γ -ray multiplicity ≥ 2 .

In this experiment, the states in the ground-state band up to the 6_1^+ state at 1526 keV have been excited. Also the 2_2^+ , 3_1^+ , and 4_2^+ states have been identified from their decays. The 0_2^+ , 0_3^+ , 0_4^+ states at excitation energies of 1135 keV, 1402 keV, and 1823 keV has been identified as well. The decays of several 2^+ states have been observed, namely of the 2_3^+ , the 2_4^+ , and 2_5^+ states at energies of 1362 keV, 1604 keV, and 1677 keV, respectively. In addition, a 2^+ state at 1847 keV has been populated as well; this state will be referred to as 2_6^+ in the following. Several states have been populated that have a possible $J^\pi = 2^+$ assignment, namely at energies of 1795 keV, 1932 keV, 1984 keV, 1988 keV, 1998 keV, 2626 keV. Based on the observation of a transition at 2426 keV coincident to the $2_1^+ \rightarrow 0_1^+$ transition and another transition at 1766 keV coincident to the $3_1^+ \rightarrow 2_2^+$ transition it has been concluded that a state at an excitation energy of 2781 keV had been populated in the experiment. Near this energy the Nuclear Data Sheets [Xia07] report a state at an energy of 2779(3) keV without a known J^π assignment.

From the observation of three transitions, one at 2523 keV coincident to the $2_1^+ \rightarrow 0_1^+$ transition, another at 2004 keV coincident to the $4_1^+ \rightarrow 2_1^+$ transition, and a third at 1863 keV coincident to the $3_1^+ \rightarrow 2_2^+$ transition, the existence of a populated state at an excitation energy of 2878 keV has been concluded. Near this energy, the Nuclear Data Sheets report a state at an energy of 2875.4 keV with a $J^\pi = 1^+(2^+)$ assignment.

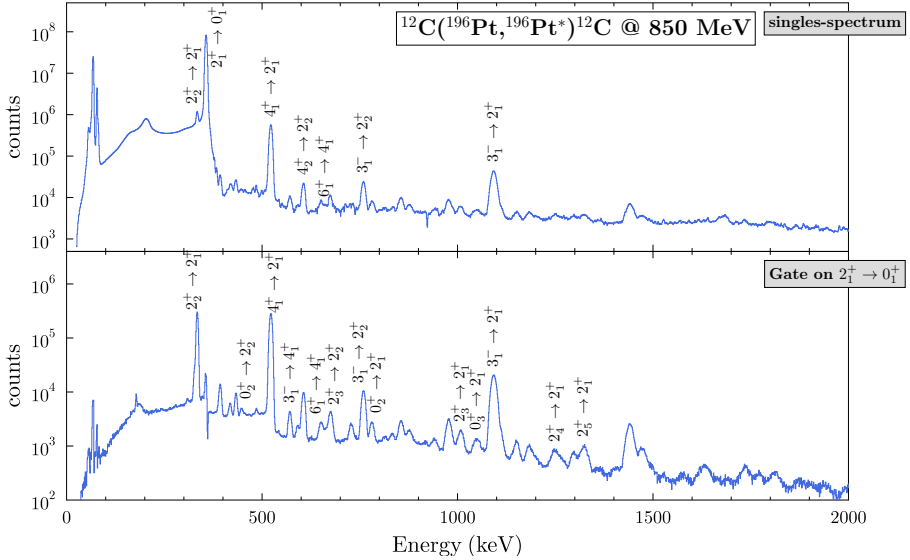


Figure 4.12.: Singles spectrum and spectrum gated on the $2_1^+ \rightarrow 0_1^+$ transition of the ^{196}Pt experiment. Images of the spectra in more detail are shown in appendix B.5.

In the spectra gated on the low-lying transitions of the level scheme, some peaks have been observed that could not be identified. The reasons hindering a placement in the level scheme have already been discussed above for the ^{194}Pt case, cf. 4.4.2.

For the quantitative part of the analysis, only the data from the runs performed with the trigger set to singles mode have been used. The intensities of the transitions have been determined from the coincidence spectra and from the singles spectra. From these, the yields Y of the states have been deduced and the normalized to the yield $Y(2_1^+)$. Detailed lists of the γ -ray intensities of the observed transitions and of the relative yields of the populated states can be found in appendix B.5.

In a CLX calculation the states of the ground-state band, the 2_2^+ , 3_1^+ , and 4_2^+ states as well the 0_2^+ , 2_3^+ , 0_3^+ , 0_4^+ , and 2_5^+ have been included. In addition, an estimate on lower limits of the decay rates of the 2_6^+ state at 1847 keV has been made. An estimate of the intensity of the decay of the 1847 keV state into the ground-state has been made based on the assumed sensitivity of a $^{195}\text{Pt}(n, \gamma)$ experiment of

Ref. [Ciz79]. The reported intensity of a decay of 1853 keV to the ground state, which is among the smallest intensities given in the reference, was used as an estimate for an upper limit for the intensity of the 1847-keV transition and has been used as a limit of the branching ratio used in the CLX calculations, assuming pure $E2$ character for the rest of the transitions depopulating the 1847-keV state.

The absolute scale of the calculation was set by the adopted value of $B(E2; 2_1^+ \rightarrow 0_1^+) = 40.6(2)$ W.u. [Xia07]. The CLX calculation followed the procedure outlined in 4.3. For the excitation process of the 4_1^+ state, an $E4$ transition $B(E4; 4_1^+ \rightarrow 0_1^+) = 3.42 \times 10^{-3} e^2b^4$ [Set91] has been included into the calculation. However, its effect on the result is only small. Due to the high sensitivity of the results on the signs of the matrix elements of the transitions, no conclusive results can be given for the decays of the 3_1^+ and 4_2^+ states. For the same reason, the uncertainties are given as a statistical uncertainty and a systematic uncertainty. The latter comprises the effects of different signs of the matrix elements in the calculations.

The results of the calculations are tabulated in Tab. 4.3 and depicted in Fig. 5.7. They will be discussed in the framework of the $O(6)$ symmetry of the Interacting Boson Model in 5.2.1.

Table 4.3.: Results of the analysis of the ^{196}Pt data

$E_{i,\text{level}}$ (keV)	J_i^π	J_f^π	E_γ (keV)	I_γ	Y_{rel}	δ	$B(E2)_i^a$ (W.u.)	Lit. [Xia07] (W.u.)
356	2_1^+	0_1^+	356	1000000(2984)	1.0000(31)		40.6(2) ^b	40.6(2)
689	2_2^+	2_1^+	333	6440(114)	$4.78(12) \times 10^{-3}$	-5.2(5)	49.2(17) _{stat} (17) _{sys}	— ^f
	0_1^+	0_1^+	622	0 ^c				
877	4_1^+	2_1^+	521	11913(29)	$1.092(5) \times 10^{-2}$		59.6(29) _{stat} (23) _{sys}	60.0(9) ^f
1015	3_1^+	2_2^+	326	415(7)	$4.3(28) \times 10^{-5}$			
	2_1^+	2_1^+	659	18.2(2) ^c				
1135	0_2^+	2_2^+	447	46.2(18)	$1.36(5) \times 10^{-4}$		31(4) _{stat} (17) _{sys}	18(10)
	2_1^+	2_1^+	780	92.2(45)			3.8(2) _{stat} (21) _{sys}	2.8(15)
1362	2_3^+	0_2^+	226	6.6(16) ^c	$2.53(7) \times 10^{-4}$		70(23) _{stat} (33) _{sys}	5(5) ^g
	3_1^+	3_1^+	347	27.4(33)			36(12) _{stat} (14) _{sys}	
	2_2^+	2_2^+	673	153.3(32)			7.0(14) _{stat} (33) _{sys}	0.26(23) ^g
	2_1^+	2_1^+	1006	101.6(44)			0.65(11) _{stat} (26) _{sys}	
	0_1^+	0_1^+	1362	27.6(50) ^c			0.037(2) _{stat} (18) _{sys}	0.0025 ^g
1402	0_3^+	2_1^+	1047	71.5(34)	$6.93(33) \times 10^{-5}$		2.7(3) _{stat} (21) _{sys}	<5.0
	2_2^+	2_2^+	714	1.7(1) ^c			0.44(5) _{stat} (34) _{sys}	<0.41
1447	3_1^-	5_1^-	177	55.3(30)	$3.76(21) \times 10^{-3}$			
	3_1^-	3_1^+	431	189(22)				
	4_1^+	4_1^+	570	137(6)				
	2_2^+	2_2^+	758	656(21)				
	2_1^+	2_1^+	1091	2588(16)				
	0_1^+	0_1^+	1447	388(82) ^c				
							$B(E3)_i = 7.86(63)$ _{stat} (4) _{sys} W.u.	5.9(21)

to be continued

Results of the analysis of the ^{196}Pt data (continued)

E_{level} (keV)	J_i^π	J_f^π	E_γ (keV)	I_γ	Y_{rel}	δ	$B(E2)_a$ (W.u.)	Lit. [Xia07] (W.u.)
1526	6_1^+	4_1^+	649	102.1(52)	$9.98(51) \times 10^{-5}$		78.0(49) _{stat} (5) _{sys}	73($^{+4}_{-73}$)
1604	2_4^+	0_3^+	202	2.8(8) ^c	$1.46(12) \times 10^{-4}$		$2.0(7)$ _{stat} (10) _{sys} $\times 10^2$	
		3_1^+	589	11.7(20)			3.9(21) _{stat} (19) _{sys}	
		4_1^+	728	40.3(28)			4.7(14) _{stat} (24) _{sys}	
		2_2^+	916	18.3(9)			0.68(17) _{stat} (34) _{sys}	
		2_1^+	1249	70.4(34)			0.56(14) _{stat} (28) _{sys}	
		0_1^+	1604	14.1(32) ^c			0.032(4) _{stat} (16) _{sys}	
1677	2_5^+	2_3^+	316	5.7(27) ^c	$3.8(14) \times 10^{-4}$		12.1(63) _{stat} (19) _{sys}	
		0_2^+	542	9.4(37) ^c			1.36(60) _{stat} (21) _{sys}	
		3_1^+	662	14.4(18)			0.76(33) _{stat} (12) _{sys}	
		4_1^+	800	9.4(37) ^c			0.195(86) _{stat} (30) _{sys}	
		2_2^+	989	26.1(12)			0.186(78) _{stat} (29) _{sys}	
		2_1^+	1321	113.1(53)			0.19(10) _{stat} (3) _{sys}	
		0_1^+	1677	189(68) ^c			0.096(36) _{stat} (19) _{sys}	
1847	2_6^+	2_1^+	243	0.38(18) ^c	$3.33(20) \times 10^{-5}$		$\geq 30(14)$ _{stat} (13) _{sys}	
		2_2^+	1159	1.73(39) ^c			$\geq 0.056(17)$ _{stat} (23) _{sys}	
		2_1^+	1492	34.5(21)			$\geq 0.31(6)$ _{stat} (13) _{sys}	
		0_1^+	1847	<3.75(72) ^e			0.0117(11) _{stat} (49) _{sys}	

^aUncertainties are given as (stat.)_{sys}. Systematical uncertainties stem from sensitivity to different sets of signs.

^bAdopted value from Nuclear Data Sheets [Xia07].

^cIntensity deduced from branching ratio given in Nuclear Data Sheets.

^dEstimate based on experimental sensitivity.

^eLimit on the intensity deduced from assumed sensitivity in an experiment in Ref. [Ciz79]. See text for details.

^fcf. Fig. 5.8

^gThe origin of these adopted values is unclear.

4.4.3 $^{130,132}\text{Ba}$

The analyses of the Ba data sets have not been as complicated in terms of the level scheme of excited states as compared to the Pt isotopes. Due to the small natural abundance of $\approx 0.1\%$ for both investigated isotopes, ^{130}Ba and ^{132}Ba , the beam intensity during the experiment, and consequently the statistics gained in the experiment has been limited. The experiences from the complicated Pt data has, however, been of great use in the analysis of the data sets.

^{130}Ba analysis

The sorting of the data of the ^{130}Ba experiment has been done using the GSSort code. The analysis of the data followed the procedure outlined in 4.1. The singles spectrum of the data is depicted in Fig. 4.13. Detailed images of the spectra can also be found in appendix B.1. From the singles and coincidence data, the level scheme of excited states has been reconstructed. A major challenge has been imposed by the close-lying energies of the 4_1^+ state at 902 keV and the 2_2^+ state at 908 keV. With the limited resolution of the experimental setup, the separation of transitions to these states has been increasingly difficult for increasing γ energies. For the same reason, also the coincidence analysis has been affected, since an exact discrimination between transitions coincident to the $4_1^+ \rightarrow 2_1^+$ and $2_2^+ \rightarrow 2_1^+$ transition was hard to achieve.

However, it has been possible to identify the transitions and the Coulomb-excited states from the data. The complete level scheme from this experiment is shown in appendix B.1. The population of the states in the ground-state band up to the 6_1^+ state at 1592 keV has been concluded. The 2_2^+ and 4_2^+ states have been populated as well. Decays of the 2_3^+ state at 1557 keV, the 3_1^- state at 1919 keV, and a 5^- state 2168 keV has been identified. (The Nuclear Data Sheets [Sin01] report a $J^\pi = 3$ assignment for the state at 1919 keV. Since it is highly unlikely to strongly excite a 3^+ state in a one-step process in Coulex it has been concluded that this state in fact can be identified as the 3_1^- state.) Additionally, three decays of a state at 2269 keV have been observed. The state had previously been observed, but no J^π assignment had been given. It will be treated like a 2^+ state in the further analysis. Besides these states, which have been assigned on the basis of the database of the Nuclear Data Sheets [Sin01], the decays of two additional states have been observed in the data.

A transition at 1463 keV coincident to the 2_1^+ ground-state decay has been observed. Except for the coincidence to the $2_1^+ \rightarrow 0_1^+$ transition no other coincident transition can be observed from the $\gamma\gamma$ -coincidence data. It has been concluded

that it originates from the decay of an excited state at 1819 keV. In the literature, no state at such an energy has been reported. In the analysis the state will be treated under the assumption of being a 2^+ state.

Another transition coincident with $2_1^+ \rightarrow 0_1^+$ transition has been observed at an energy of 2014 keV. Except for the coincidence to the $2_1^+ \rightarrow 0_1^+$ transition no other coincident transition can be observed from the $\gamma\gamma$ -coincidence data. The peak of the 2014 keV transitions contains more than twice the intensity of the 1463 keV transition. It has been assigned to a state at 2371 keV. In this energy region, no excited state has been reported except for a 2^+ state at 2361 keV [Sul08]. Regarding the large energy difference of 10 keV, it does not seem probable that the state observed in the present experiment is identical to the one reported in this previous work. In the course of the analysis, the state at 2371 keV will be treated under the $J^\pi = 2^+$ assumption.

From the spectra of the singles and coincidence data, the intensities of the transitions have been determined. From them, the yields of the states have been deduced and then normalized to the yield of the 2_1^+ state. Detailed lists of the γ -ray intensities and of the relative yields are shown in appendix B.1.

The peak of the $2_3^+ \rightarrow 0_1^+$ transition overlaps with the peak of the $3_1^- \rightarrow 2_1^+$ transition. From the intensity-difference of this peak in the singles and coincidence data an upper limit for the γ -ray intensity of the 1557 keV transition has been deduced.

The presumed ground-state transition of the 1819 keV and 2371 keV states have not been observed in the spectra. Estimates on upper limits for the intensities of the transitions have been made.

Based on the relative yields deduced from the spectra, CLX calculations have been performed. The calculations followed the procedure outlined in 4.3. The 2_1^+ , 4_1^+ , 6_1^+ , 2_2^+ , 4_2^+ , 2_3^+ , and 3_1^- states have been included into the calculations. Estimates on possible $B(M1; 2^+ \rightarrow 2_1^+)$ strengths have been made based on lower limits of the relative yields of the 1819 keV, 2269 keV, and 2371 keV states. These limits have been calculated from the γ -ray intensities of the unambiguously observed decays of the states. In the calculations, the absolute scale has been set by the adopted value of $B(E2; 2_1^+ \rightarrow 0_1^+) = 57.9(17)$ W.u. [Sin01]. As in the previous discussions for the Pt isotopes, the values are again given with a statistical and systematic uncertainty. The latter stems from the sensitivity of the results on different choices of the signs of the transition matrix elements.

The results of the calculations are summarized in Table 4.4. They will be discussed with respect to the existence of one-quadrupole phonon excitation of mixed proton-neutron symmetry ($2_{1,ms}^+$) in 5.1.1.

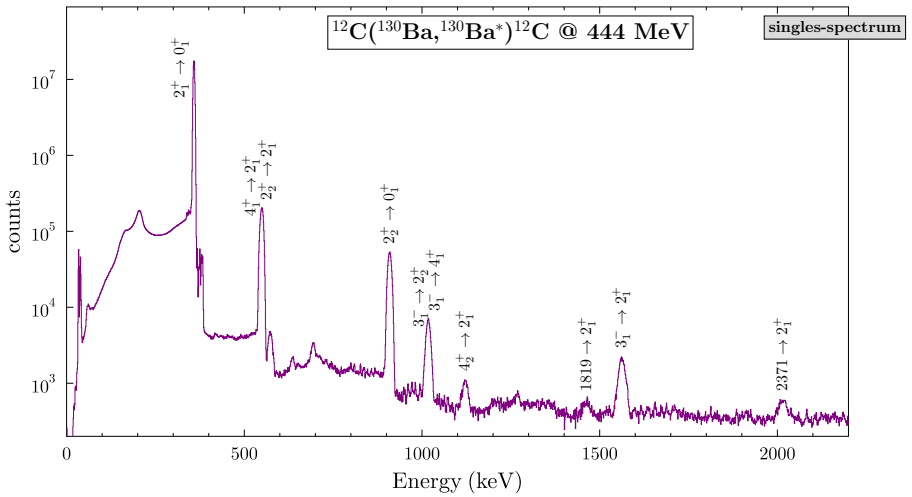


Figure 4.13.: Doppler corrected, background subtracted singles sum spectrum of ^{130}Ba . A more detailed illustration of the spectrum and coincidence data can be found in appendix B.1.

Table 4.4.: Results of the analysis of the ^{130}Ba data

E_{level} (keV)	J_i^{π}	J_f^{π}	E_{γ} (keV)	I_{γ}	Y_{rel}	δ	$B(E2)_i^a$ (W.u.)	Lit. [Sin01] (W.u.)
357	2_1^+	0_1^+	357	1000000(3655)	1.000(3)		57.9(17) ^b	57.9(17)
902	4_1^+	2_1^+	544	13663(707)	$1.176(71) \times 10^{-2}$		85.0(62) _{stat} (6) _{sys}	78.9(13)
908	2_2^+	2_1^+	551	16451(750)	$2.765(76) \times 10^{-2}$	E2	51.2(32) _{stat} (33) _{sys} 2.96(13) _{stat} (19) _{sys}	
1477	4_2^+	2_2^+	569	296(10)	$6.68(17) \times 10^{-4}$			
		4_1^+	575	172(10)				
		2_1^+	1120	197(9)				
1557	2_3^+	2_2^+	649	15.7(36)	$5.55(56) \times 10^{-5}$	-0.01(3) ^b	$\geq 2.93 \times 10^{-4}$ $B(M1) \geq 3.32 \times 10^{-3} \mu_N^2$ ≥ 2.67	
						+3.2(4) ^b	$B(M1) \geq 2.96 \times 10^{-4} \mu_N^2$ ≥ 0.0283	
		2_1^+	1200	39.5(43)		-0.31(2) ^b	$B(M1) \geq 1.20 \times 10^{-3} \mu_N^2$ ≥ 0.34	
						-23(9) ^b	$B(M1) \geq 2.49 \times 10^{-6} \mu_N^2$ $0.0218(25)$ _{stat} (94) _{sys}	
1592	6_1^+	4_1^+	692	174.9(68)	$1.759(68) \times 10^{-4}$		175(16) _{stat} (1) _{sys}	94(6)
1819	2^+ (assumed)	2_1^+	1463	86(6)	$8.70(61) \times 10^{-5}$	pure M1	$B(M1) \geq 3.5 \times 10^{-3} \mu_N^2$ ≥ 0.59	
		0_1^+	1819	≤ 25.7		pure E2	0.059(7) _{stat} (14) _{sys}	

to be continued

Results of the analysis of the ^{130}Ba data (continued)

E_{level} (keV)	J_i^π	J_f^π	E_γ (keV)	I_γ	Y_{rel}	δ	$B(E2)_\downarrow$ (W.u.)	Lit. [Sin01] (W.u.)
1919	3^-	2_2^+ 4_1^+ 2_1^+ 0_1^+	1011 1017 1561	122(11) 1540(13) 911(26)	$2.588(32) \times 10^{-3}$			
2168	5^-	6_1^+ 4_1^+	576 1266	56.5(36) 77.8(56)	$1.350(67) \times 10^{-4}$		$B(E3) = 24.2(22)_{\text{stat}}(3)_{\text{sys}}$ W.u.	
2269	$2^+(\text{assumed})$	2_2^+	1361	49.8(91)	$1.15(13) \times 10^{-4}$	M1 E2	$B(M1) \leq 0.022\mu_N^2$ ≤ 4.3	
2371	$2^+(\text{assumed})$	2_1^+ 0_1^+	1912 2269	30.3(74) 34.2(43)	$1.92(15) \times 10^{-4}$	M1 E2	$B(M1) \leq 4.76 \times 10^{-3}\mu_N^2$ ≤ 0.48 $0.229(38)_{\text{stat}}(52)_{\text{sys}}$	
			2014	191(15)		pure M1 pure E2	$B(M1) \geq 0.134\mu_N^2$ ≥ 12.0 $0.44(14)_{\text{stat}}(20)_{\text{sys}}$	
			2371	≤ 15.3				

^aUncertainties are given as (stat.) (sys.). Systematical uncertainties stem from sensitivity to different sets of signs.

^bValues from Nuclear Data Sheets [Sin01].

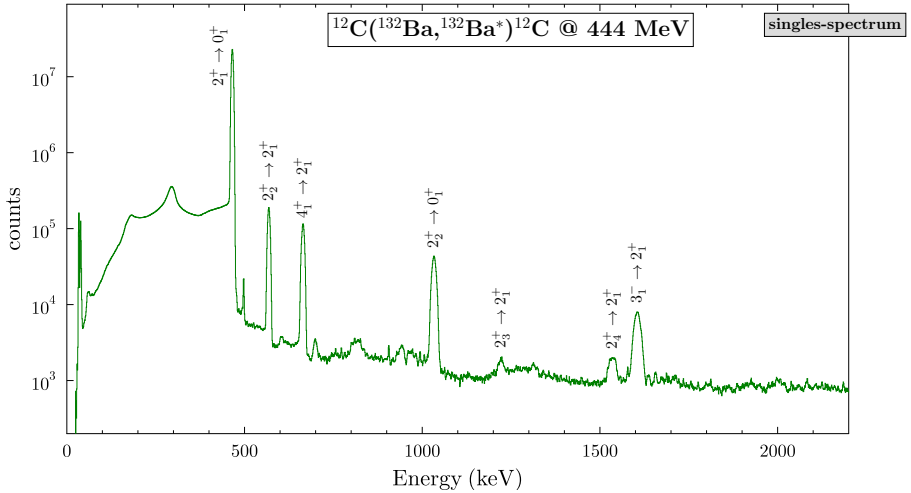


Figure 4.14.: Doppler corrected, background subtracted singles sum spectrum of ^{132}Ba . A more detailed illustration of the spectrum and coincidence data can be found in appendix B.2.

^{132}Ba analysis

The sorting of the data has been performed using the GSSort program that had also been deployed for the ^{130}Ba analysis as well as for the analysis of the Pt experiments, cf. 4.1.

The reconstruction of the level scheme of excited states of ^{132}Ba from the singles and coincidence spectra has been done without mayor problems. The singles spectrum is shown in Fig. 4.14. Images of the spectra in more detail as well as the complete level scheme of excited state in the experiment are to be found in appendix B.2. In the experiment, the ground-state band up to the 6_1^+ state at 1932 keV has been populated. Also the 2_2^+ and 4_2^+ states have been excited in the experiment. The decays of the third and fourth 2^+ state at energies of 1686 keV and 1998 keV have been observed as well. Octupole 3^- states have been excited at energies of 2069 keV and 2374 keV. Besides these states, a possible 4^+ state at 1944 keV, a possible 0_4^+ state at 2271 keV and a state with a possible $J^\pi = 2^+ - 6^+$ at 2439 keV have been populated. In addition to these states, the existence of two more states is assumed based on otherwise non-identified transitions in the data. The width and position of the peak corresponding to the $3_2^- \rightarrow 2_1^+$ transition in

the spectrum coincident to the $2_1^+ \rightarrow 0_1^+$ transition did not meet the expectations unless a second peak at an energy of ≈ 1930 keV is assumed in this alleged doublet-peak. The energy could not be determined more exactly than about 5 keV. Since this transition could not be placed into the level scheme, the excitation of a state at ≈ 2400 keV has been concluded. The Nuclear Data Sheets [Kha05] report a state with a possible 0^+ assignment at an energy of 2406(8) keV. The difference in the energy at which it was observed has been decided to be too large for an unambiguous identification. Therefore, during the analysis, this state will be treated like a 2^+ state.

At an energy of ≈ 2222 keV in the spectrum coincident to the $2_1^+ \rightarrow 0_1^+$ transition, a peak has been observed that could not be identified either. It was concluded that it stems from the decay of a state at ≈ 2686 keV. No state has been reported in the Nuclear Data Sheets in this energy region. This state will be treated as 2^+ state during the analysis.

As in the analyses for the other isotopes, the intensities of the γ -ray transitions have been determined from the singles and coincidence spectra. From these, the yields of the states have been deduced and then normalized to the yield of the 2_1^+ state. Detailed lists of the experimentally deduced intensities and relative yields can be found in appendix B.2.

Based on these data, CLX calculations have been performed including the 2_1^+ , 2_2^+ , 4_1^+ , 2_3^+ , 4_2^+ , 6_1^+ , 2_4^+ , and 3_1^- states. Under the assumptions of being 2^+ states and of pure $M1$ $2^+ \rightarrow 2_1^+$ transitions, estimates on lower limits of possible $B(M1; 2^+ \rightarrow 2_1^+)$ strengths have been included in the CLX calculations for the states at ≈ 2400 keV, 2439 keV, and 2686 keV. The calculations have been done according to the procedures introduced in 4.3.

The results of the calculations are summarized in Table 4.5. These results will be discussed with respect to the evolution of the one quadrupole-phonon states of mixed proton-neutron symmetry, $2_{1,ms}^+$, in 5.1.2.

Table 4.5.: Results of the analysis of the ^{132}Ba data

E_{level} (keV)	J_i^{π}	J_f^{π}	E_{γ} (keV)	I_{γ}	Y_{rel}	δ	$B(F2)_{\gamma}$ ^a (W.u.)	Lit. [Kha05] (W.u.)
465	2_1^+	0_1^+	465	100000(2902)	1.000(3)		43(4) ^c	43(4)
1032	2_2^+	2_1^+	567	10823(31)	$1.678(7) \times 10^{-2}$	$+14 \begin{smallmatrix} +3 \\ -2 \end{smallmatrix}$ ^c	$51.4(44)_{\text{stat}}(37)_{\text{sys}}$ $B(M1) = 0.00022(2)_{\text{stat}}(1)_{\text{sys}} \mu_N^2$ $1.42(12)_{\text{stat}}(7)_{\text{sys}}$	$144(14)^f$ $3.9(4)^f$
1128	4_1^+	2_1^+	663	8362(24)	$8.101(36) \times 10^{-3}$		$69.4(48)_{\text{stat}}(3)_{\text{sys}}$	
1686	2_3^+	2_2^+	654	$13.0(5)^b$	$8.67(41) \times 10^{-5}$	$+0.28(8)^c$	$1.9(11)_{\text{stat}}(5)_{\text{sys}}$ $B(M1) = 0.029(17)_{\text{stat}}(8)_{\text{sys}} \mu_N^2$ $0.57(10)_{\text{stat}}(15)_{\text{sys}}$	
		2_1^+	1221	109(4)		$-0.25(2)^c$	$B(M1) = 0.038(6)_{\text{stat}}(10)_{\text{sys}} \mu_N^2$ $0.0326(36)_{\text{stat}}(87)_{\text{sys}}$	
		0_1^+	1686	$1.85(8)^b$				
1729	4_2^+	4_1^+	602	53(6)	$2.40(11) \times 10^{-4}$			
		2_2^+	698	134(8)				
		2_1^+	1265	56(6)				
1932	6_1^+	4_1^+	805	53(3)	$5.34(35) \times 10^{-5}$		$95(11)_{\text{stat}}(1)_{\text{sys}}$	
1998	2_4^+	2_2^+	966	80(6)	$5.02(13) \times 10^{-4}$	$+0.11(6)^c$	$0.14(16)_{\text{stat}}(1)_{\text{sys}}$ $B(M1) = 0.030(4)_{\text{stat}}(1)_{\text{sys}} \mu_N^2$ $0.0018(18)_{\text{stat}}(1)_{\text{sys}}$	
		2_1^+	1534	310(7)		$+0.02(2)^c$	$B(M1) = 0.030(4)_{\text{stat}}(1)_{\text{sys}} \mu_N^2$ $0.397(49)_{\text{stat}}(9)_{\text{sys}}$	
		0_1^+	1998	101(2) ^b				

to be continued

Results of the analysis of the ^{132}Ba data (continued)

E_{level} (keV)	J_i^π	J_f^π	E_γ (keV)	I_γ	Y_{rel}	δ	$B(E2)_j^a$ (W.u.)	Lit. [Kha05] (W.u.)
2069	3_1^-	2_3^+ 4_1^+	383 941	37.7(19) 138(5)	$2.408(18) \times 10^{-3}$			
		2_2^+ 2_1^+	1037 1604	171(9) 1977(24)				
~ 2400	^d	2_1^+ 0_1^+	~ 1930 ~ 2400	79.2(54) <15.4	$8.00(54) \times 10^{-5}$	M1	$B(M1) \geq 0.026\mu_N^2$ 0.168(26) _{stat} (2) _{sys}	$B(E3) = 21.2(25)$ _{stat} (2) _{sys} W.u. 24.3(30) ^g
2439	$2^+ - 6^+$	4_1^+ 2_1^+ 0_1^+	1311 1974 2439	80.8(58) 20.4(28) <12.6	$1.02(7) \times 10^{-4}$	E2 M1	≥ 33.4 $B(M1) \geq 0.012\mu_N^2$ 0.234(37) _{stat} (32) _{sys}	
~ 2686	^e	2_1^+ 0_1^+	~ 2221 ~ 2686	49.4(41) <30.3	$4.99(41) \times 10^{-5}$	M1	$B(M1) \geq 0.012\mu_N^2$ 0.215(37) _{stat} (3) _{sys}	

^aUncertainties are given as (stat.) (sys.). Systematical uncertainties stem from sensitivity to different sets of signs.

^bIntensity deduced from branching ratio given in Nuclear Data Sheets [Kha05].

^cValues from Nuclear Data Sheets.

^dThe position of the transitions is hard to determine. No assignment to a previously known state was possible. A state at 2406(8) keV has been reported with $J^\pi = 0^+$ assignment.

^eNo transition could be assigned to the observed peak at ~ 2221 keV in spectrum coincident to $2_1^+ \rightarrow 0_1^+$ transition. A estimate of a possible MSS character has been done assuming 2^+ character of this possible state.

^fValues are from [Bur85]; reported $B(E2)$ values do not match decay branching ratio.

^gValue from [Bur85].

5 Discussion

5.1 Mixed-symmetry states of $^{130,132}\text{Ba}$

The experimental campaign for the investigation of the Ba isotopes had been motivated by the search for one quadrupole-phonon states of mixed proton-neutron symmetry ($2_{1,\text{ms}}^+$) in these nuclei. This collective excitation has already been introduced in the framework of the proton-neutron version of the interacting boson model in 2.3.3. Unlike the lowest-lying collective states of atomic nuclei, in particular unlike the 2_1^+ state, the wave function of the $2_{1,\text{ms}}^+$ is not symmetric under the exchange of proton and neutron labels. It has been demonstrated in the nucleus ^{94}Mo that this class of excitations is a fundamental building block of nuclear collectivity [Pie00]. The unique experimental signature of mixed-symmetric states (MSS) is a strong $M1$ decay to the corresponding fully-symmetric state. For the identification of the $2_{1,\text{ms}}^+$ state, this corresponds to a strong $B(M1; 2_{1,\text{ms}}^+ \rightarrow 2_1^+)$ decay rate of $\approx 0.2 \mu_N^2$. The $E2$ transition strength of its ground-state transition is expected to be on the order of 1 W.u. . These values result in a very short lifetime of the state on the order of 100 fs.

$2_{1,\text{ms}}^+$ states are the lowest-lying states of mixed-symmetry in vibrational nuclei. Therefore, examples of these states have been predominantly observed in nuclei in the proximity to closed shells, for example in the nucleus ^{94}Mo , which may be considered the best-investigated nucleus with respect to mixed-symmetric excitations [Pie99, Pie00, Fra01, Fra03], or ^{138}Ce , which was the second nucleus in which a MSS was identified using the present experimental technique [Rai06]. The method of investigating the $2_{1,\text{ms}}^+$ state of vibrational nuclei by γ -ray spectroscopy in projectile Coulomb excitation reactions on a carbon target has previously been pioneered in an experiment [Pie01] on ^{96}Ru , isotone of ^{94}Mo . In a recent experimental campaign using this technique, the stable even-even isotopes of the Xe isotopic chain have been investigated with respect to the existence of a $2_{1,\text{ms}}^+$ state [Coq10]. It was observed that the energy of the $2_{1,\text{ms}}^+$ excitation increases from 1947 keV in the nucleus ^{134}Xe to 2150 keV and 2127 keV in the isotopes ^{130}Xe and ^{128}Xe , while, simultaneously, the strength $B(M1; 2_{1,\text{ms}}^+ \rightarrow 2_1^+)$ decreases from $0.3 \mu_N^2$ in ^{134}Xe to $0.04 \mu_N^2$ in ^{128}Xe . In the nuclei ^{126}Xe and ^{124}Xe , no mixed-symmetry state could be identified from the experiments below the experimental sensitivity thresholds

of approximately 2.1 and 2.3 MeV, respectively. These observations have been puzzling, in particular the decrease of the $B(M1)$ strength on the path to mid-shell nuclei. A possible explanation of this behavior might be an increase of the fragmentation of the $2_{1,\text{ms}}^+$ state over several 2^+ states. The experimental observation in the Xe isotopes would then only include those fragments that reside below the limit of the experimental sensitivity. In fact, the phenomenon of fragmentation of the $2_{1,\text{ms}}^+$ state has previously been observed in this mass region, e.g. in ^{138}Ce [Rai06] and ^{134}Ba [Mol88, Faz92].

It was the goal of the present experiments on the nuclei $^{130,132}\text{Ba}$ to extend the database on the $2_{1,\text{ms}}^+$ state in the Ba chain and in the even-even isotopes of the $A = 130$ mass region, which will allow for a systematic investigation of the behavior that had been observed in the neighboring Xe isotopic chain. The results of the two experiments on the nuclei $^{130,132}\text{Ba}$ (cf. Tables 4.4 and 4.5) contain decay rates of several 2^+ states of these nuclei. This information shows that the method of projectile Coulomb excitation using a large HPGe detector array like Gammasphere is a very successful technique for the determination of observables that serve as crucial signatures for nuclear collectivity.

5.1.1 ^{130}Ba

The experimental results on the nucleus ^{130}Ba are summarized in Tab. 4.4. A plot of the strength distributions is shown in Fig. 5.1. The values of $B(E2; 2_2^+ \rightarrow 2_1^+) = 51.2(32)_{\text{stat}}(33)_{\text{sys}}$ W.u. and $B(E2; 2_2^+ \rightarrow 0_1^+) = 2.96(13)_{\text{stat}}(19)_{\text{sys}}$ W.u. correspond to a lifetime of $\tau(2_2^+) = 4.71(19)_{\text{stat}}(22)_{\text{sys}}$ ps. From an additional run of the experimental campaign using the DSAM technique, a lifetime of this state of $\tau = 6.63_{-0.39}^{+0.18}$ ps has been deduced [Bau13]. Despite the difference in the resulting values, a fairly good description of the lineshape has been reached by a fit using the present value of the lifetime, cf. [Bau13, Fig. 6.8].

In this nucleus, no absolute value for a $B(M1; 2_i^+ \rightarrow 2_1^+)$ could be deduced, because, except for the 2_3^+ state, no multipole mixing ratio has been known from previous experiments and could not be determined from the present experimental data either, due to the lack of sufficient statistics in the respective transitions. All of the results on $B(M1; 2_i^+ \rightarrow 2_1^+)$ values in this nucleus are, thus, based on assumptions of pure transitions, and, for most of the assumed 2^+ states, also on estimates of their ground-state transition intensities.

For the decay of the 2_3^+ state at 1557 keV to the 2_1^+ state two possible values for the mixing ratio δ have been given [Sin01], $\delta = -23(9)$ corresponding to a nearly pure $E2$ transition and $\delta = 0.31(2)$, corresponding to a $>90\%$ $M1$ contribution to

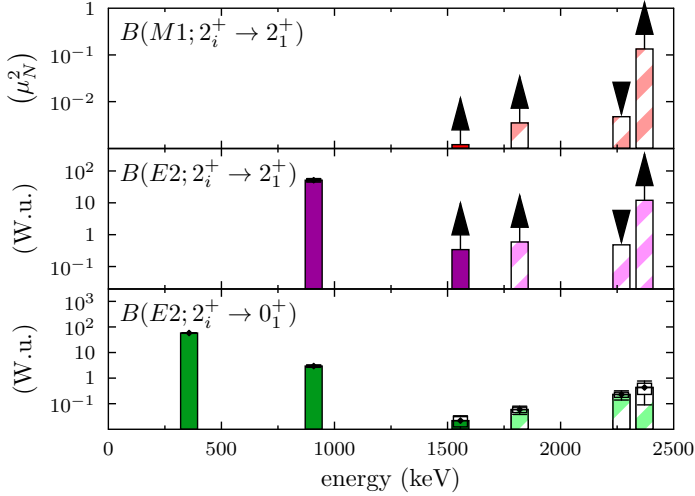


Figure 5.1.: Strength distributions from the results of ^{130}Ba .

this transition. The transition strengths have been calculated for both values. The results on the $B(M1; 2_3^+ \rightarrow 2_1^+)$ show that even for the nearly pure $M1$ transition the strength of $B(M1; 2_3^+ \rightarrow 2_1^+) \geq 1.2 \times 10^{-3} \mu_N^2$ is only quite small. The ground-state transition strength of $B(E2; 2_3^+ \rightarrow 0_1^+) = 0.0218(25)_{\text{stat}}(94)_{\text{sys}}$ W.u. is very small, too. These values are considerably smaller than what would be expected for a $2_{1,\text{ms}}^+$ state and indicate that the 2_3^+ state does not contain a considerable fraction of the $2_{1,\text{ms}}^+$ wave function.

For the states at energies of 1819 keV, 2269 keV, and 2371 keV, no clear J^π assignment has been found in the literature. Those have been treated as 2^+ states during the analysis and their possible $B(M1; 2^+ \rightarrow 2_1^+)$ values have been estimated under the additional assumption of pure $M1$ multipolarity.

The estimate of $B(M1; 1819 \rightarrow 2_1^+) \geq 3.50 \times 10^{-3} \mu_N^2$ is also quite small. Also the result of $B(E2; 1819 \rightarrow 0_1^+) = 0.059(7)_{\text{stat}}(14)_{\text{sys}}$ W.u. is small. Again, these values do not allow for the identification of a significant fragment of the $2_{1,\text{ms}}^+$ state.

The same conclusion can be drawn from the estimates for the decay rates of the 2269 keV state. The value of $B(M1; 2269 \rightarrow 2_1^+) \leq 4.76 \times 10^{-3} \mu_N^2$ is very small when compared to the expectation of an isolated $2_{1,\text{ms}}^+$ state. The value of

$B(E2; 2269 \rightarrow 0_1^+) = 0.229(38)_{\text{stat}}(52)_{\text{sys}}$ W.u. is stronger than for the 1819 keV state.

The estimate of the decay rates of the 2371 keV state has been made under the same assumptions of $J^\pi = 2^+$ and of a pure $M1$ transition to the 2_1^+ state. The result of $B(M1; 2371 \rightarrow 2_1^+) \geq 0.134 \mu_N^2$ W.u. represents the strongest $M1$ transition strength for this nucleus. Its magnitude nearly fulfills the expectations on an isolated $2_{1,\text{ms}}^+$ state. Also the result of $B(E2; 2371 \rightarrow 0_1^+) = 0.46(15)_{\text{stat}}(21)_{\text{sys}}$ W.u. meets the expectation for the order of magnitude of this transition strength. However, these numbers are based on numerous assumptions, beginning with the unknown J^π assignment. In this energy range the excitation of states can be ruled out that are not fed from above and have spin quantum numbers $J^\pi \neq 3^-$ or 2^+ . Unfortunately, the statistics in the data on this state are not sufficient for a more detailed angular distribution analysis. As estimate of a possible $B(E3; 2371 \text{ keV} \rightarrow 0_1^+)$ value for an assumed $J^\pi = 3^-$ assignment resulted in an approximate value of ≈ 4 W.u., which does not seem unlikely in the light of the value of $B(E3; 3_1^- \rightarrow 0_1^+) = 24.2(22)_{\text{stat}}(3)_{\text{sys}}$ W.u. . In addition, a 3^- state in the level scheme of ^{132}Ba at 2374 keV is reported in the Nuclear Data Sheets [Kha05] and has been excited in the experiment discussed below. An estimate of its $B(E3; 2374 \text{ keV} \rightarrow 0_1^+)$ value resulted in ≈ 1.2 W.u., and is, thus, of the same order of magnitude of the estimate for the 2371 keV state of ^{130}Ba . Therefore, a $J^\pi = 3^-$ assignment of the 2371 keV state of ^{130}Ba cannot be ruled out based on these data.

Consequently, based on the given data the state at 2371 keV can be assigned a *candidate* of an isolated $2_{1,\text{ms}}^+$ state in ^{130}Ba – provided the underlying assumptions of $J^\pi = 2^+$ and of a predominant $M1$ transition to the 2_1^+ state are valid. The other 2^+ states at 1557 keV, 1819 keV, and 2269 keV exhibit nearly vanishing $B(M1; 2_i^+ \rightarrow 2_1^+)$ values and can, thus, be identified at most as weak fragments of the $2_{1,\text{ms}}^+$ state.

5.1.2 ^{132}Ba

The experimental results on the nucleus ^{132}Ba are summarized in Tab. 4.5. A plot of the strength distributions is shown in Fig. 5.2.

The results show two 2^+ states for which absolute values of the $B(M1; 2^+ \rightarrow 2_1^+)$ transition strengths have been deduced, namely the states at 1686 keV and 1998 keV. For the 1686 keV state a transition strength of $B(M1; 2^+ \rightarrow 2_1^+) = 0.038(6)_{\text{stat}}(10)_{\text{sys}} \mu_N^2$ has been deduced. This value lies well below the expected value for the decay of an isolated $2_{1,\text{ms}}^+$ state. The value of $B(E2; 2_3^+ \rightarrow 0_1^+) = 0.0326(36)_{\text{stat}}(87)_{\text{sys}}$ W.u. is considerably smaller than the expected value of about 1 W.u., too. From these numbers an identification of the 1686 keV state as an iso-

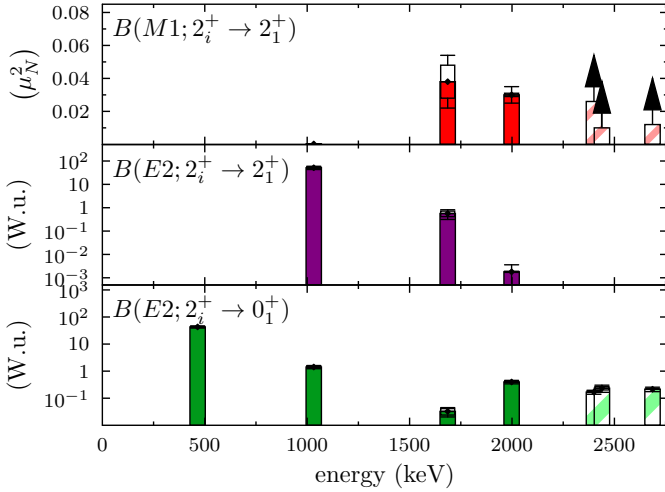


Figure 5.2.: Strength distributions from the results of ^{132}Ba .

lated $2_{1,\text{ms}}^+$ state can be ruled out. However, the results justify the assignment of the 1686 keV as a *fragment* of the $2_{1,\text{ms}}^+$ state. This assignment is further supported by the observation of the $3_1^- \rightarrow 2_3^+$ transition at 383 keV. A strong $E1$ transition connecting the 3_1^- and the $2_{1,\text{ms}}^+$ states has been suggested as additional signature of the $2_{1,\text{ms}}^+$ state [Pie03]. From the γ -ray intensities of the present experimental data, a ratio

$$R_{E1} = \frac{B(E1; 3_1^- \rightarrow 2_3^+)}{B(E1; 3_1^- \rightarrow 2_1^+)} = 1.40(7) \quad (5.1)$$

can be deduced under the quite safe assumption of the 383 keV transition being an $E1$ transition. This value of R_{E1} is smaller than it has previously been observed for other nuclei [Pie03], but still shows an enhanced strength in the decay to the 2_3^+ state. Both facts, the $B(E1; 3_1^- \rightarrow 2_3^+)$ being larger than the $B(E1; 3_1^- \rightarrow 2_1^+)$ value on one hand, and on the other hand the fact that R_{E1} is not much larger than one, may support the assignment of the 2_3^+ state as a *fragment* of the $2_{1,\text{ms}}^+$ state of ^{132}Ba .

The result on the $B(M1)$ transition strength of the decay of the 1998 keV state of $B(M1; 2^+ \rightarrow 2_1^+) = 0.030(4)_{\text{stat}}(1)_{\text{sys}} \mu_N^2$ is slightly smaller than for the

1686 keV state, but still on the same order of magnitude. The $B(E2; 2_4^+ \rightarrow 0_1^+) = 0.397(49)_{\text{stat}}(9)_{\text{sys}}$ W.u. is considerably larger than for the 1686 keV state. Also for this state the identification of the state as a fragment of the $2_{1,\text{ms}}^+$ can be drawn on the basis of the experimental results, although no decay of the 3_1^- state into the 2_4^+ state could be observed.

For three higher-lying states the spin and parity assignment $J^\pi = 2^+$ has been assumed. Under the additional assumption of pure $M1$ decays into the 2_1^+ state, estimates on lower limits on their possible $M1$ decay rates have been made.

The values of $B(M1; 2400 \rightarrow 2_1^+) \geq 0.026 \mu_N^2$, $B(M1; 2439 \rightarrow 2_1^+) \geq 0.012 \mu_N^2$, and $B(M1; 2686 \rightarrow 2_1^+) \geq 0.012 \mu_N^2$ do not exhibit a pronounced $M1$ strength. The corresponding ground-state transition strengths are of the order of 0.2 W.u. to 0.35 W.u. . Based on these data, the three states at 2400 keV, 2439 keV, and 2686 keV can at most be interpreted as *candidates* for fragments of the $2_{1,\text{ms}}^+$ state, provided that the assumptions made in the calculations could be confirmed.

On the basis of the present results it can be concluded that no prominent, isolated $2_{1,\text{ms}}^+$ state has been observed in the nucleus ^{132}Ba below an energy of ≈ 2.7 MeV. From the $B(M1)$ strength distributions only weak fragments of the MSS could possibly be identified in this nucleus.

5.1.3 $2_{1,\text{ms}}^+$ states in the $A = 130$ mass region

The present results on the isotopes $^{130,132}\text{Ba}$ complete the available experimental data on $B(M1; 2_i^+ \rightarrow 2_1^+)$ transition strengths and $2_{1,\text{ms}}^+$ states in the stable even-even nuclei of the $A = 130$ mass region of the nuclear chart. An overview of the available data on the $B(M1; 2_i^+ \rightarrow 2_1^+)$ strength distributions for this mass region is shown in Fig. 5.4. The data now allows for a comparison of the evolution of the $2_{1,\text{ms}}^+$ states or its fragments throughout the isotopic and isotonic chains of the mass region. The evolution of the summed $B(M1)$ strengths and the energies of the $2_{1,\text{ms}}^+$ states of the Ba isotopic chain are depicted in Fig. 5.3.

In ^{136}Ba an isolated mixed-symmetry state at 2129 keV had been identified. In the even-even neighbor ^{134}Ba the mixed-symmetry state has been observed to fragment over two close-lying 2^+ states at 2029 keV and 2088 keV. This decrease in energy continues for the present results on ^{132}Ba . Here, a small fragment of the MSS has been identified at an energy of 1686 keV. Further candidates for $2_{1,\text{ms}}^+$ -fragments in this nucleus are the states at 1998 keV, and, based on different assumptions, at 2400 keV, 2439 keV, and 2686 keV. None of the possible $2_{1,\text{ms}}^+$ -fragments in ^{132}Ba exhibits a $B(M1; 2^+ \rightarrow 2_1^+)$ of similar strength as it has been observed in the $^{134,136}\text{Ba}$

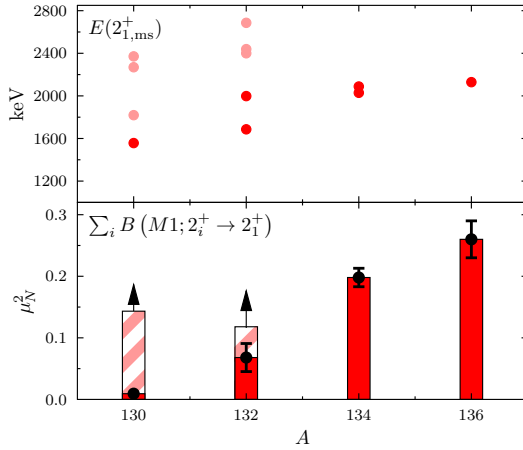


Figure 5.3.: Evolution of the fragments of the $2_{1,ms}^+$ state in the Ba isotopic chain.

The upper panel shows the energies of the fragments of the $2_{1,ms}^+$ state. The lower panel shows the $B(M1; 2_i^+ \rightarrow 2_1^+)$ strength distributions for the Ba isotopic chain. The data on the isotopes $^{134,136}\text{Ba}$ has been compiled from [Mol88, Faz92, Pie98a, Sch04, Pie08]. The present results for the isotopes $^{130,132}\text{Ba}$ seem to support the assumption of an increase in fragmentation of the $2_{1,ms}^+$ state with increasing valence space. The energetic trend of the fragments of the $2_{1,ms}^+$ is opposite to the trend observed in the neighboring Xe isotopes. However, the estimate of the very strong value of $B(M1; 2_{2371}^+ \rightarrow 2_1^+)$ completely alters this picture, provided the underlying assumptions are valid.

nuclei. A state with the expected properties of an isolated MS state can be excluded in ^{132}Ba below ≈ 2.7 MeV based on the experimental data.

For the nucleus ^{130}Ba a further decrease of the energies of possible fragments of the MSS has been observed with the 2_3^+ state at 1557 keV, but with an almost entirely vanishing $B(M1; 2_3^+ \rightarrow 2_a^+ y1)$ value. The same observation has been made for $M1$ transition strengths of the decays of the 1819 keV state and the 2269 keV state, respectively. If the discussion is limited to these states, the results seem to support the afore-mentioned assumption of an increase in the fragmentation of the $2_{1,ms}^+$ state with increasing size of the valence space. The energies of the fragments of the MS states decrease in energy, which would be an inversion of the energy trend observed in the neighboring Xe isotopes. At the same time the summed

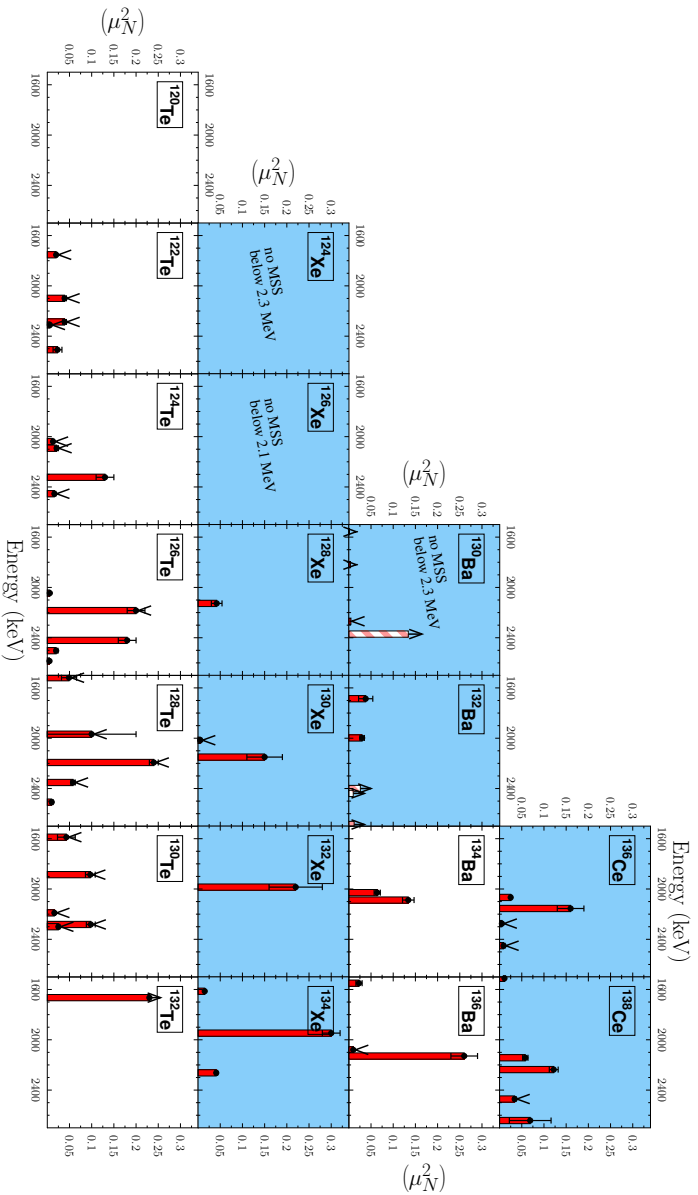


Figure 5.4: Overview on the $B(M1; 2^+ \rightarrow 2_1^+)$ strength distributions in the $A = 130$ mass region. The data for the nuclei shaded in blue stem from Coulex experiments using Gammasphere. The data for $^{130,132}\text{Ba}$ are results of the present work. The other data have been compiled from the data in [Ahn12, Rai06, Mol88, Faz92, Pie98a, Sch04, Pie08, Rai10, Coq11, Coq09, Coq10, Ahn09, Hic08, Van04, Kat02, Son02, Son04].

$B(M1; 2_i^+ \rightarrow 2_1^+)$ strength decreases almost linearly with increasing valence space, cf. Fig. 5.3.

However, the results also include the large value of the estimate on the $B(M1; 2_{2371}^+ \rightarrow 2_1^+) \geq 0.134 \mu_N^2$. If this value could be confirmed, it would clearly indicate a major fragment of the $2_{1,ms}^+$ state or even an isolated $2_{1,ms}^+$ state of ^{130}Ba . Assuming this is true, this observation changes the picture completely. Instead of a decrease in energy of the MS state, an increase of the energy of the $2_{1,ms}^+$ in the Ba isotopic chain would have been observed with the exception of ^{132}Ba , in which the lack of evidence for $B(M1)$ strengths of similar order of magnitude below excitation energies of approximately 2.7 MeV is puzzling. The further development of the discussion on the evolution of the $2_{1,ms}^+$ state in the Ba isotopic chain will, thus, depend on the verification or falsification of the assumption of a strong value of $B(M1; (2^+)_{2371} \rightarrow 2_1^+)$.

The evolution of the summed $B(M1)$ strengths and the energies of the $2_{1,ms}^+$ states of the $N = 76$ isotonic chain are depicted in Fig. 5.5. While the nucleus ^{130}Xe exhibits a large fragment or even an isolated MS state at 2150 keV, the picture changed completely for ^{132}Ba . Here, the $M1$ strength is fragmented over two states, at least, depending on the validity of the assumptions made for the higher-lying states. The energy of the lowest fragment of the MS state is located at 1686 keV. Based on these observations, an increase in fragmentation of the MS state can be concluded for the $N = 76$ isotones with increasing valence space. At the same time, the energies of the fragments of the MSS decrease in energy. This is in contrast to the neighboring $N = 78$ and $N = 80$ isotonic chains, where an increase of the energies of the MSS can be observed on the path away from the $Z = 50$ closed shell, cf. Fig. 5.4.

The evolution of the summed $B(M1)$ strengths and the energies of the $2_{1,ms}^+$ states of the $N = 74$ isotonic chain are depicted in Fig. 5.6. While the nucleus ^{128}Xe exhibits an isolated $2_{1,ms}^+$ state at 2127 keV the $B(M1)$ strength in ^{130}Ba is fragmented over several states. Again, with the energy of the lowest-lying potential fragment of the $2_{1,ms}^+$ state at 1557 keV, the energetic trend for increasing valence space is a decrease in energy of the fragments of the $2_{1,ms}^+$. At the same time the strength of the potential fragments almost vanishes. In this respect the trend observed in the $N = 76$ isotones of an increasing fragmentation with a decrease in the energies of the fragments seems to be found analogously in the $N = 74$ isotones. However, the possible $2_{1,ms}^+$ state of ^{130}Ba at an energy of 2371 keV, if confirmed, would change this picture completely and would raise the question why the $M1$ strength in the neighboring nucleus ^{128}Xe is significantly smaller and no fragment

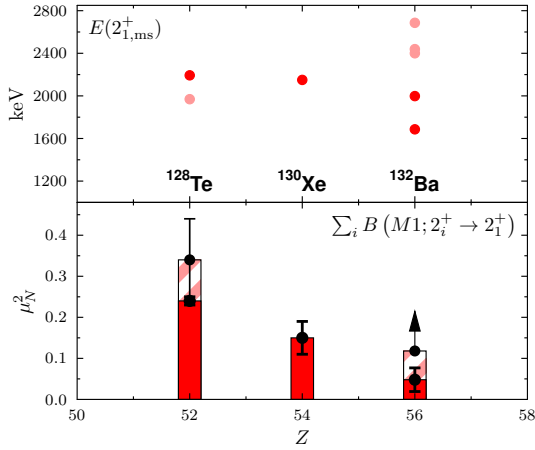


Figure 5.5.: Evolution of the fragments of the $2_{1,ms}^+$ state in the $N = 76$ isotonic chain. The upper panel shows the energies of the fragments of the $2_{1,ms}^+$ state. The lower panel shows the $B(M1; 2_i^+ \rightarrow 2_1^+)$ strength distributions for the $N = 76$ isotonic chain. The data on the nuclei ^{128}Te and ^{130}Xe has been compiled from [Hic08] and [Coq10]. The present results for the isotope ^{132}Ba seem to support the assumption of an increase in fragmentation of the $2_{1,ms}^+$ state with increasing valence space. For the $N = 76$ isotopic chain the energetic trend of the fragments of the $2_{1,ms}^+$ reverses with respect to the neighboring $N = 78$ and $N = 80$ isotonic chains.

of comparable strength has been observed.

In conclusion it has been observed that the evolutions of the energies of the $2_{1,ms}^+$ state for increasing valence spaces in the isotonic and isotopic chains of the $A = 130$ mass region follow different trends. While in the $N = 80$ and $N = 78$ isotones an increase of the energy of the MSS has been observed, this trend inverts in the $N = 76$ isotones and, unless the assignment of the 2371 keV state as a candidate is based on valid assumptions, also for the $N = 74$ isotones.

A similar picture has been observed in the isotopic chains. While an increase of the energies of the $2_{1,ms}^+$ states has been observed in the Xe isotopic chain, the energy of the MSS decreases in the Ba isotopic chain. A decrease of the energy can also be observed in the nuclei of the Ce isotopes. The behavior of the inversion of

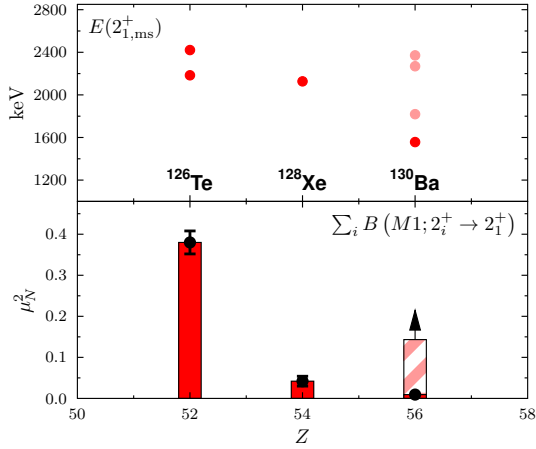


Figure 5.6.: Evolution of the fragments of the $2_{1,ms}^+$ state in the $N = 74$ isotonic chain. The upper panel shows the energies of the fragments of the $2_{1,ms}^+$ state. The lower panel shows the $B(M1; 2_i^+ \rightarrow 2_1^+)$ strength distributions for the $N = 74$ isotonic chain. The data on the nuclei ^{126}Te and ^{128}Xe has been compiled from [Coq09] and [Van04, Kat02]. The present results for the isotope ^{130}Ba seem to support the assumption of an increase in fragmentation of the $2_{1,ms}^+$ state with increasing valence space. The estimate of the $B(M1; 2_{2371}^+ \rightarrow 2_1^+)$ is a clear indication of a dominant fragment of the MSS, but the value has been determined with the caveat of several assumptions, beginning with the $J^\pi = 2^+$ assignment.

energetic trends seems to appear between $N = 78$ and $N = 76$ and between the Xe and Ba isotopes, and, thus, in direct proximity to the nucleus ^{134}Ba , which has been suggested as a realization of the E(5) shape phase-transitional point [Cas00], cf. 2.4.1. This seems to hint at a connection of the energetic trends in the empirical data to the shapes of the nuclei in the region.

A common feature observed throughout all isotopic and isotonic chains in the region is the decrease in $B(M1; 2_i^+ \rightarrow 2_1^+)$ strength on the way to mid-shell nuclei to almost vanishing values for the nucleus ^{130}Ba .

However, if the large fragment of the MSS in ^{130}Ba could be confirmed, completely new questions would arise, in particular concerning the lack of comparably enhanced $B(M1; 2_i^+ \rightarrow 2_1^+)$ strengths in the neighboring nuclei ^{128}Xe and ^{132}Ba .

This means either, that these nuclei indeed have a $2^+_{1,ms}$ state but which resides at energies beyond the experimental detection limit, or, that this observation reflects a real physical effect that is unexplained at present. The discussion strongly depends on the nature of the 2371 keV state in ^{130}Ba . For a continued discussion of the observations in the $A = 130$ mass region further investigation of this state is of utmost importance. Unfortunately, the experimental accessibility will presumably be hindered by the low natural abundance of ^{130}Ba of only $\approx 0.1\%$.

5.2 Test of the O(6) symmetry in $^{194,196}\text{Pt}$

The O(6) dynamical symmetry of the Interacting Boson Model has already been briefly introduced in 2.3.2. It is characterized by a level scheme whose patterns can be classified in terms of the quantum numbers σ and τ . An inherent feature of each theoretical model are selection rules for the decay of states. For the algebraic framework of the Interacting Boson Model, selection rules are strongly connected to the irreducible representations of each of the subchain decompositions that characterize the different dynamical symmetries, cf. 2.3.2. In the framework of the consistent-Q-formalism [War82, War83] of the O(6) dynamical symmetry $E2$ transitions are allowed and collective if the conditions $\Delta\sigma = 0$ and $\Delta\tau = \pm 1$ are fulfilled, cf. (2.44) in 2.3.2. The O(6) symmetry also makes parameter-free predictions on ratios of certain transitions strengths, cf. Eq. (2.45).

There are only few examples in nature for a manifestation of the O(6) symmetry in atomic nuclei. Among these, nuclei from the Xe-Ba-Ce region near $A = 130$ have been proposed [Cas85]. The nucleus considered the best example for a manifestation of an O(6) symmetry in nature is ^{196}Pt [Ciz78, Ciz79]. In this nucleus, the level scheme as well as the observed branching ratios in the γ decays exhibit the characteristic features inherent for the symmetry. Its neighboring nucleus ^{194}Pt shows a large similarity to ^{196}Pt concerning the level scheme as well as the properties of the γ transitions. Therefore, also this nucleus can count as a candidate for the manifestation of the O(6) symmetry.

However, in most cases such assignments have been based on data of branching ratios and level scheme patterns. These are of course necessary conditions for the identification of the symmetry in a nucleus. In fact a more significant statement would have to be based on absolute values of transition strengths, most ideally for transitions between states belonging to different representations of the O(6) quantum number σ .

This has recently been shown in the example of the nuclei ^{124}Xe [Rai10] and ^{126}Xe [Coq11]. Both nuclei had previously been identified as being good candidates for the manifestation of structure close to the O(6) symmetry [Wer01, Gad00]. In

experiments utilizing the same experimental technique as the present work these nuclei have been investigated in terms of transition strengths between the low-lying states. Unlike previous measurements the results also contained absolute values on the transition strengths of the decays of the 0_3^+ states that had been assigned the band heads of the families of states with $\sigma = N - 2$ quantum numbers in the respective nuclei. The values of $B(E2; 0_3^+ \rightarrow 2_1^+) = 12(2)$ W.u. and $B(E2; 0_3^+ \rightarrow 2_2^+) = 19(2)$ W.u. in ^{124}Xe [Rai10], and $B(E2; 0_3^+ \rightarrow 2_1^+) = 10.9(25)$ W.u. and $B(E2; 0_3^+ \rightarrow 2_2^+) = 13.4(41)$ W.u. in ^{126}Xe [Coq11] are clearly collective and, thus, violate the $\Delta\sigma = 0$ selection rule of the O(6) dynamical symmetry.

The experiments on the $^{194,196}\text{Pt}$ isotopes of the present work have been motivated by these findings. The goal of the experiments was the test of the O(6) symmetry of the nuclei $^{194,196}\text{Pt}$ based on absolute measurements of decay rates of states with $\sigma = N - 2$ quantum number assignments. The technique of projectile Coulomb excitation using a large detector array is a very powerful method to determine absolute values of these crucial signatures within single experiments.

5.2.1 ^{196}Pt

The nucleus ^{196}Pt is usually considered the best candidate for a manifestation of the O(6) symmetry in the nuclear chart. Its level scheme as well as its decay pattern in terms of branching ratios have been identified to be consistent with the predictions from the O(6) limit. The 0_3^+ state at 1402 keV has been identified as the band head of the $\sigma = 4 = N - 2$ family of states [Ciz78]. For its decay an upper limit of $B(E2; 0_3^+ \rightarrow 2_1^+) < 5.0$ W.u. [Bör90] has been previously measured. The 2_4^+ state at 1604 keV has been suggested as the $\sigma = 4, \tau = 1$ state on top of the 0_3^+ state. A transition between the two states has been reported, but apart from the branching ratio, no absolute value for its strength is known. The observation of a strongly collective $2_4^+ \rightarrow 0_3^+$ E2 transition in combination with a weak $0_3^+ \rightarrow 2_1^+$ E2 transition would be strong evidence for the $\sigma = N - 2$ assignment of both, the 0_3^+ and 2_4^+ states. The 2^+ state at 1847 keV has been suggested as the $\sigma = 4, \tau = 2$ state [Ciz78], i.e. the analog to the band head of the γ band for the $\sigma = N - 2$ family of states. This assignment would need to be confirmed by the observation of a strongly collective E2 transition to the alleged $\sigma = 4, \tau = 1$ state at 1604 keV, which would be the analog to the strongly collective $2_2^+ \rightarrow 2_1^+$ transition of the $\sigma = N$ states. A decay branching ratio for the $2^+(1847 \text{ keV}) \rightarrow 2_4^+$ transition has been given [Ciz79], but, again, no absolute value has yet been measured, i.e., while the observed γ -decay branching ratios favor the presence of states with O(6) quantum numbers $\sigma = N - 2$, a proof of their collective character is missing to date.

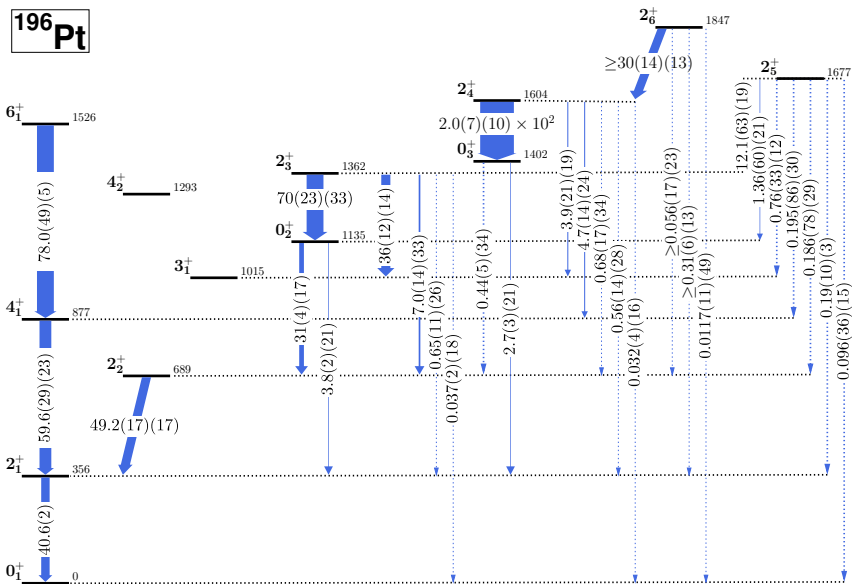


Figure 5.7.: Schematic overview of the results of the analysis of the ^{196}Pt experiment

The present results of the experimental data are tabulated in Tab. 4.2 and are shown in Fig. 5.9.

In general it can be stated that the transitions between states with $\Delta\tau > 1$ are suppressed compared to the transitions between states with $\Delta\tau = \pm 1$. This can be seen, for example, from the decays of the $\tau = 4$ 2_3^+ state. While the transitions to the $\tau = 3$ 0_2^+ and 3_1^+ states are clearly collective ($B(E2; 2_3^+ \rightarrow 0_2^+) = 70(23)(33)$ W.u. and $B(E2; 2_3^+ \rightarrow 3_1^+) = 36(12)(14)$ W.u.), the other transitions depopulating that state are significantly weaker and are all non-collective. Also the decays of the 0_2^+ and 2_4^+ states support this statement. The $\Delta\tau$ selection rule, and thus, the U(5) symmetry is fulfilled in the low-lying level scheme of ^{196}Pt .

The results contain the value of $B(E2; 2_4^+ \rightarrow 0_3^+) = 2.0(7)_{\text{stat}}(10)_{\text{sys}} \times 10^2$ W.u.. Although this value has a large uncertainty, it clearly proves a strongly collective transition between the 2_4^+ and 0_3^+ states in ^{196}Pt for the first time. The further decays of this state go to states within the $\sigma = N$ family and with different τ quantum number. According to the present results, these transitions are strongly suppressed by two or three orders of magnitude compared to the transition to the $\sigma = N - 2, \tau = 0$ state.

The result of $B(E2; 0_3^+ \rightarrow 2_1^+) = 2.7(3)_{\text{stat}}(21)_{\text{sys}}$ W.u. is about an order of magnitude smaller than expected for a collective transition. It represents the decay of the band head of the $\sigma = N - 2$ family of states into the $\sigma = N$ family. According to the $O(6)$ selection rules, this transition is forbidden in the $O(6)$ dynamical symmetry. The experimental result on its $B(E2)$ value qualitatively agrees with this prediction and, in combination with the strongly collective $2_4^+ \rightarrow 0_3^+$ transition on top of it, justifies the assignment of the 0_3^+ state being the band head of the $\sigma = N - 2$ structure within the algebraic description of ^{196}Pt by the IBM.

The results of the analysis also contain estimates on the decay rates of the 2_6^+ state at 1847 keV. While the transitions to the 0_1^+ , 2_1^+ , and 2_2^+ states can be deduced to be smaller than 1 W.u., the value of $B(E2; 2_6^+ \rightarrow 2_4^+)$ is collective. These numbers support the assignment of this state as the γ band in the $\sigma = N - 2$ representation on an absolute scale for the first time.

The present results on the decays of the 0_3^+ , 2_4^+ , and 2_6^+ states, thus, reveal the same pattern of levels and connecting collective transitions among them as for the lowest-lying 0_1^+ , 2_1^+ , and 2_2^+ states. This repetition of the level pattern is a prediction of the $O(6)$ dynamical symmetry of the IBM. Consequently, the absolute data on transition strengths between the 0_3^+ , 2_4^+ , and 2_6^+ states further support their assignment as the lowest-lying levels of the $\sigma = N - 2$ representation of the $O(6)$ and, consequently, support the assignment of the nucleus ^{196}Pt as a manifestation of the $O(6)$ symmetry for the first time based on absolute $E2$ transition strengths.

The data also allow for statements concerning the ratios $B_{4/2} = B(E2; 4_1^+ \rightarrow 2_1^+)/B(E2; 2_1^+ \rightarrow 0_1^+)$ and $B_{2/2} = B(E2; 2_2^+ \rightarrow 2_1^+)/B(E2; 2_1^+ \rightarrow 0_1^+)$. For these ratios the IBM in the $O(6)$ limit makes parameter-free predictions of $B_{4/2} = B_{2/2} = 1.310$ for $N = 6$, cf. (2.45). The present data suggest that the prediction of the $O(6)$ dynamical symmetry limit indeed agrees very well with the present results. A comparison of the present results with previous experiments and this predictions is shown in Fig. 5.8.

In conclusion, the results of the present experiment confirm that the selection rules of the $O(6)$ symmetry are reasonably well fulfilled in the nucleus ^{196}Pt . This makes ^{196}Pt the only nucleus of the entire nuclear chart for which the manifestation of the $O(6)$ symmetry has been proven on the basis of absolute values on decay rates of states with $\sigma = N - 2$ quantum number assignment.

5.2.2 ^{194}Pt

The discussion of the results of the ^{194}Pt experiment with respect to the $O(6)$ symmetry is not as obvious as in the case of ^{196}Pt . The results of the analysis of the

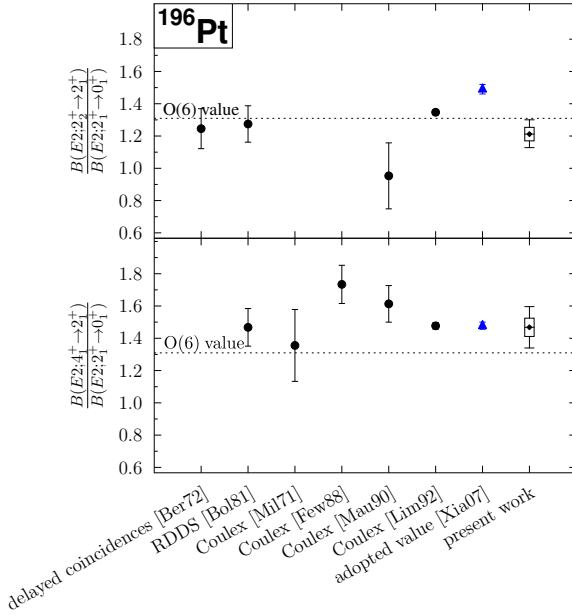


Figure 5.8.: Comparison of results from previous publications on the ratios $B_{4/2}$ and $B_{2/2}$ of ^{196}Pt . The results have been taken from [Ber72, Bol81, Mil71, Few88, Mau90, Lim92]. The nuclear data sheets [Xia07] do not give a value for $B(E2; 2_2^+ \rightarrow 2_1^+)$. The data point has been calculated from the value of the lifetime by neglecting $B(M1; 2_2^+ \rightarrow 2_1^+)$ and $B(E2; 2_2^+ \rightarrow 0_1^+)$, because the numbers given do not lead to conclusive results.

experimental data on ^{194}Pt are summarized in Tab. 4.2 and are shown in Fig. 5.9. Analogous to the observation in the neighboring nucleus ^{196}Pt , the $\Delta\tau = \pm 1$ selection rule is fulfilled. A good example for this is the decay behavior of the alleged $\tau = 4$ 2_3^+ state, that decays collectively to the $\tau = 3$ 0_2^+ and 3_1^+ states (The results are $B(E2; 2_3^+ \rightarrow 0_2^+) = 85(24)(34)$ W.u. and $B(E2; 2_3^+ \rightarrow 3_1^+) < 24$ W.u., respectively.).

In analogy to the level scheme of the nucleus ^{196}Pt , the 0_4^+ state at 1547 keV is a candidate for the $\sigma = N - 2$ band head assignment. This state has been excited in the present experiment and the strengths of its decay have been deduced to be $B(E2; 0_4^+ \rightarrow 2_1^+) = 12.7(8)_{\text{stat}}(19)_{\text{sys}}$ W.u. and $B(E2; 0_4^+ \rightarrow 2_2^+) = 14.7(11)_{\text{stat}}(22)_{\text{sys}}$ W.u.. Not only are these transitions clearly collective, and, thus, would break the O(6) selection rule if the state was indeed a member of

¹⁹⁴Pt

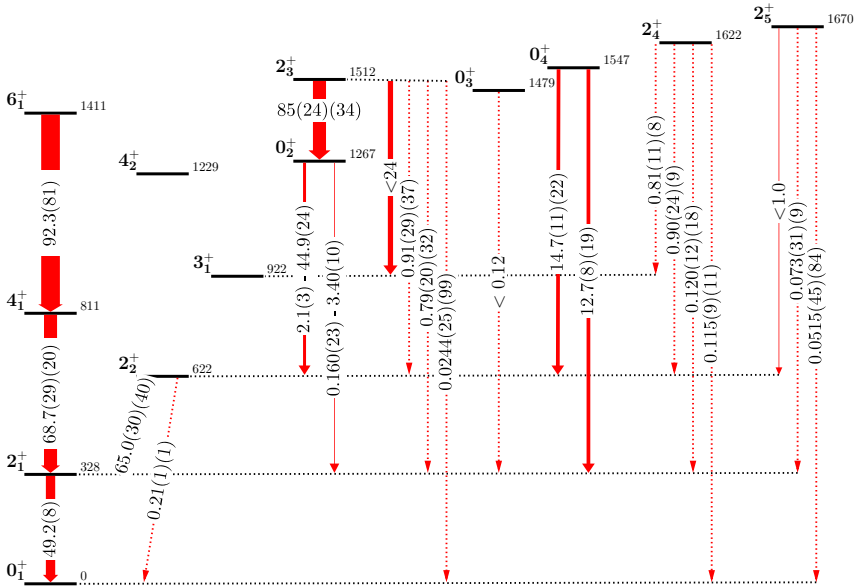


Figure 5.9.: Schematic overview of the results of the analysis of the ¹⁹⁴Pt experiment

the $\sigma = N - 2$ family. Also the similarity in both the absolute values of the decay strengths as well as the branching ratio between them to the values deduced for the ^{124,126}Xe nuclei is striking. In the Xe cases, results of $B(E2; 0_3^+ \rightarrow 2_1^+) = 12(2)$ W.u. and $B(E2; 0_3^+ \rightarrow 2_2^+) = 19(2)$ W.u. in ¹²⁴Xe [Rai10] and $B(E2; 0_3^+ \rightarrow 2_1^+) = 10.9(25)$ W.u. and $B(E2; 0_3^+ \rightarrow 2_2^+) = 13.4(41)$ W.u. in ¹²⁶Xe [Coq11] have led to the conclusion of a broken O(6) symmetry.

However, another 0⁺ state at 1479 keV has been reported in previous publications, e.g. in ¹⁹⁴Ir β decay [Cle76], in (n, n' γ) [Fil81], (p, d) [Ber81], and (p, t) [Dea79] reactions, also its E0 ground-state transition has been observed [Kib05]. In the present experiment no evidence of a Coulomb excitation of this state has been found. The data allow for an estimate of $B(E2; 0_3^+ \rightarrow 2_1^+) < 0.12$ W.u. for the decay of this state, provided an excitation had occurred. Such a weak transition strength would indeed satisfy the O(6) selection rule, if this 0₃⁺ state were to be identified as the $\sigma = N - 2$ band head.

A decision, whether and which of the two 0^+ states in question can be assigned the $\sigma = N - 2$ quantum number could be justified by the observation of a 2^+ state on top of the 0^+ state connected by a collective $E2$ transition as it has been observed in ^{196}Pt . For the two observed 2_4^+ and 2_5^+ states at 1622 keV and 1670 keV, respectively, no such transition has been observed nor reported previously. However, given the small energy difference between the two 2^+ states and the two 0^+ states in question such a connection does not seem very probable. In this respect, the interpretation of the results does not yield very conclusive results.

From the results, comparisons of the values of the ratios $B_{4/2} = B(E2; 4_1^+ \rightarrow 2_1^+)/B(E2; 2_1^+ \rightarrow 0_1^+)$ and $B_{2/2} = B(E2; 2_2^+ \rightarrow 2_1^+)/B(E2; 2_1^+ \rightarrow 0_1^+)$ to the predictions of the IBM can be made. The IBM in the $O(6)$ dynamical symmetry predicts $B_{4/2} = B_{2/2} = 1.336$ for $N = 7$, cf. (2.45). These predictions agree very well with the results of the present experiment. A plot of the comparison between the present results with previous experiments and the predictions is shown in Fig. 5.10. The agreement between the present results and the $O(6)$ prediction for the ratios $B_{4/2}$ and $B_{2/2}$ is even better than in the case of the ^{196}Pt , which is, after all, considered the best example of an $O(6)$ manifestation in nature.

It should be noted that the adopted values from the Nuclear Data Sheets [Sin06] on both, the $B(E2; 2_2^+ \rightarrow 2_1^+)$ and the $B(E2; 4_1^+ \rightarrow 2_1^+)$, only represent the largest values of the previous experimental results and do not seem to reflect an unbiased compilation of the previous experimental results.

In conclusion, the results of the ^{194}Pt experiment indeed show some interesting features predicted by the IBM in the $O(6)$ dynamical symmetry. The decay pattern of the 0_4^+ state with collective $E2$ transitions to the 2_1^+ and 2_2^+ states are clearly outside the pattern of $O(6)$ symmetry. However, a clear-cut statement on the $O(6)$ character of the nucleus based on decay strengths of a $\sigma = N - 2$ state can not be made on the basis the present results. The question whether the nucleus ^{194}Pt exhibits a manifestation of the $O(6)$ symmetry has, thus, to remain open for the moment.

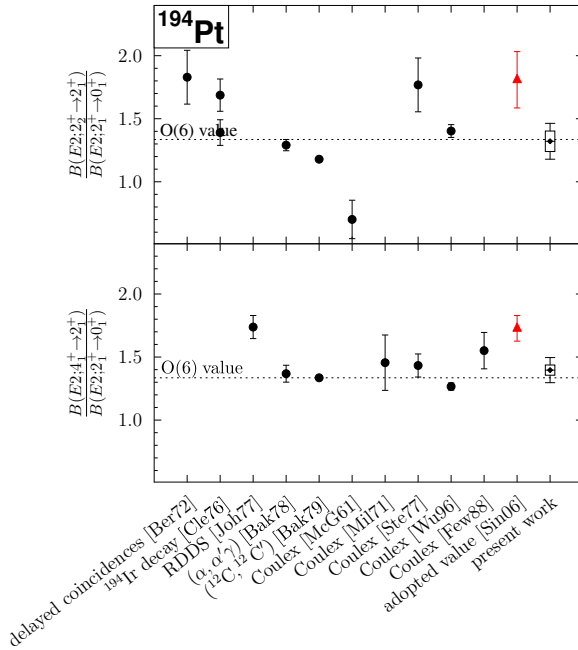


Figure 5.10.: Comparison of results from previous publications on the ratios $B_{4/2}$ and $B_{2/2}$ of ^{194}Pt . The results have been taken from [Ber72, Cle76, Joh77, Bak78, Bak79, McG61, Mil71, Ste77, Wu96, Few88]. Cleveland76 [Cle76] give their result relative to $B(E2; 4_1^+ \rightarrow 2_1^+)$ which has been calculated for the adopted value and for the present result. The present results agree very well with the prediction of the IBM in the O(6) limit [Iac87].

5.3 Investigation of the β band of ^{154}Sm

The physical motivation for the ^{154}Sm experiment can be found in the confined- β -soft rotor model (CBS), which has been introduced in 2.4.3. It describes the collective properties of nuclei on the path between the X(5) transitional point [Iac01] and the SU(3) dynamical symmetry of the Interacting Boson Model. Analog to the X(5) solution, the wave function as a function of the deformation parameter β of the first excited 0^+ state in the framework of the CBS features a node in the potential. This is the defining feature of a β -band. The models for X(5) and the CBS, thus, suggest that this type of collective excitation can occur in nuclei with a flat potential in the deformation parameter β .

The model has been introduced for the description of the nuclei ^{152}Sm and ^{154}Sm [Pie04]. Those nuclei had been chosen because the nucleus ^{152}Sm is considered as being the best example for a manifestation of the properties of the X(5) dynamical symmetry in a nucleus [Cas01b]. Its neighboring nucleus ^{154}Sm shows the typical rotor-like behavior in its level scheme as it can already be deduced from the value of $R_{4/2} = 3.26$. For ^{152}Sm the CBS description agrees very well with the experimental data on both, the excitation energies and the transition strengths for the ground-state band as well as for the $K = 0$ band. This is not a very surprising result, since the CBS is a generalization of the X(5) transitional-point description. Good agreement of the CBS predictions with the experimental data on the ground-state band of ^{154}Sm had also been achieved. However, the experimental data on the decay rates of states of the first excited $K = 0$ band has been incomplete at the time, and, hence, no definitive statement on this band could be given. The available data before the conduction of the present experiment comprised a lifetime of the 0_2^+ state of $\tau(0_2^+) = 1.3(3)$ ps [Krü99] deduced from a DSAM measurement, which also included a lower limit on the lifetime of the 2_2^+ state of $\tau(2_2^+) > 3.5$ ps. No information on the transition strengths of the decay of the 4_2^+ state had previously been known. The previous measurements of $\tau(0_2^+)$ led to an assignment of this state as a being the band head of a β band [Krü99].

The present results extend the information on the decay rates from the $K = 0$ band in ^{154}Sm . The results are tabulated in Tab. 4.1 and are displayed in Fig. 5.11. A comparison of the results to predictions of the CBS model and to the X(5) solution is shown in Tab. 5.1.

The agreement of the X(5) predictions with the present results on the transition strengths in the $K = 0$ band of ^{154}Sm is not very good. This is not a big surprise given the rotor-like level scheme of the nucleus ^{154}Sm ($R_{4/2} = 3.26$). The agreement of the data with the predictions of the CBS model ($r_\beta = 0.35$) [Pie04] is much better, cf. Tab. 5.1. Only the transition strengths for the $4_2^+ \rightarrow 6_1^+$ and $2_2^+ \rightarrow 4_1^+$

Table 5.1.: Comparison of the present results of $E2$ transition strengths for the states in the β band of ^{154}Sm with the theoretical predictions from the X(5) description [Iac01] and from the CBS rotor model ($r_\beta = 0.35$) [Pie04].

$J_i \rightarrow J_f$	$E_x(J_i)(\text{keV})$		$B(E2)(\text{W.u.})$		
	CBS	Expt.	X(5)[Iac01] ^a	CBS[Pie04]	present results
$2_1^+ \rightarrow 0_1^+$	82	82	176	174	176(1) ^b
$4_1^+ \rightarrow 2_1^+$	268	267	278	251	245(6) ^b
$6_1^+ \rightarrow 4_1^+$	546	544	348	281	289(8) ^b
$8_1^+ \rightarrow 6_1^+$	903	903	400	300	319(17) ^b
$0_\beta^+ \rightarrow 2_1^+$	1231	1099	111	8.4	11.2(21)
$2_\beta^+ \rightarrow 0_1^+$	1325	1178	3.5	0.5	0.32(4)
$2_\beta^+ \rightarrow 2_1^+$			16	1.4	0.72(9)
$2_\beta^+ \rightarrow 4_1^+$			63	7.1	1.32(15)
$4_\beta^+ \rightarrow 2_1^+$	1546	1338	1.8	0.1	0.32(11)
$4_\beta^+ \rightarrow 4_1^+$			11	1.1	0.57(18)
$4_\beta^+ \rightarrow 6_1^+$			49	8.2	0.66(21)

^aScaled to the $B(E2; 2_1^+ \rightarrow 0_1^+)$ value.

^bValue from [Rei09].

transitions are overestimated in the model by a factor of 5-12. The general agreement of the CBS predictions for the transitional nucleus ^{152}Sm obtained with a structural parameter of $r_\beta = 0.14$ and of the rotor nucleus ^{154}Sm ($r_\beta = 0.35$) with the experimental data is very good. This demonstrates the ability of the CBS model of the description of the $K = 0$ band of nuclei with varying stiffness of the potential on the path from the transitional point X(5) to the rigid rotor.

Regarding the wave function of the first excited 0^+ state in the CBS model, this state is described by the parameter $s = 2$. The wave function of this state bears a characteristic feature a node when expressed in terms of the deformation parameter β , cf. Fig. 2.10, and, thus, describes an excitation in the deformation parameter β . From the agreement of the CBS predictions with the present results, it can be concluded that the first excited $K = 0$ band of the nucleus ^{154}Sm can indeed be identified as a β band. An assignment made previously [Krü99] can, therefore, be

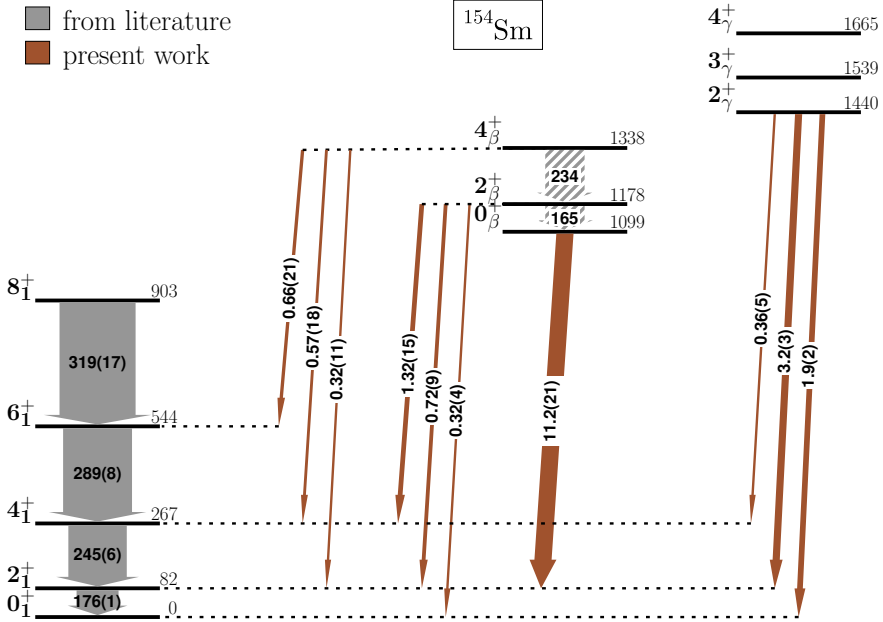


Figure 5.11.: Overview on the present results of the transition strengths in the β and γ bands of ^{154}Sm .

supported on the basis of the present experimental results.

In conclusion, the results of the present work on the decay rates in the first excited $K = 0$ band of ^{154}Sm agree very well with the predictions made in the confined- β -soft rotor model. The character of this band in that model of being a true β excitation allows for the conclusion that the nucleus ^{154}Sm is one of the rare cases where a β band can be assigned.

This analysis has previously been published in 2012 as a Rapid Communication in Physical Review C [Mö112].

6 Summary and Outlook

In the present work, the experiments on three different types of collective nuclei have been presented and their results have been discussed. It has been shown how projectile Coulomb excitation can be used to determine absolute values of decay rates of low-lying states of collective nuclei. The method has been discussed and the techniques used for the analysis have been introduced. In the course of this work, the techniques used in the analysis process could be further developed, for instance the treatment of coincidence data and the treatment of interferences in the CLX calculations induced by different signs of transition matrix elements. The results of the analyses yield absolute values of decay rates that had been predicted in the form of signatures of theoretical models and, hence, allow for interesting and important insights into several topics of current scientific interest on nuclear collectivity.

It has been shown that the nucleus ^{196}Pt indeed can be identified as a manifestation of the $O(6)$ symmetry. This statement can be soundly based on the measurement of the decay rates of three collective states that can be assigned $\sigma = N - 2$ quantum numbers, making ^{196}Pt the only nucleus for which such values have been determined on an absolute scale. However, for the neighboring nucleus ^{194}Pt the present data do not allow for a definite statement of a possible $O(6)$ symmetry, which is mainly due to the existence of two close-lying 0^+ states with different decay patterns.

For the nucleus ^{154}Sm the results on the decay rates of the states in the first excited $K = 0$ band allowed for the support of a previous assignment of a beta band, which can be established by the good agreement of the experimental data with the predictions of the CBS rotor model.

The experimental data on the $B(M1; 2_i^+ \rightarrow 2_1^+)$ strengths of the nuclei $^{130,132}\text{Ba}$ completed the experimental data on the one quadrupole-phonon state of mixed proton-neutron symmetry ($2_{1,\text{ms}}^+$) in the $A = 130$ mass region. The new data enabled a discussion of the evolution of the $2_{1,\text{ms}}^+$ state in the $N = 76$ and $N = 74$ isotonic chains as well as for the Ba isotopic chain. The results seem to support the previous observation of an increased fragmentation of the $2_{1,\text{ms}}^+$ state for mid-shell nuclei of that mass region. However, the results showed an enhanced candidate of a $2_{1,\text{ms}}^+$ state in ^{130}Ba that hampers a unified view of the results and their interpretation, but whose results are based on several assumptions during the calculations,

beginning with the $J^\pi = 2^+$ assignment. Any further discussion on the evolution of the MSS in this mass region will, therefore, depend on an independent verification or falsification of the assumptions made for the calculations on the 2371 keV state of ^{130}Ba .

Beyond that, the present results clearly show that projectile Coulomb excitation using a high-intensity ion accelerator in combination with a large multi-detector HPGe array like Gammasphere is an ideal method for the investigation of decay rates and, thus, enable experimenters to search for crucial signatures of different theoretical models of nuclear quadrupole collectivity on an absolute scale. Given the prospects of strongly increased ion intensities of future generation particle accelerators, e.g. at FAIR in Darmstadt, and on increased detection efficiency and energy resolution of next generation HPGe arrays like AGATA or GRETA, this method will certainly be able to address the afore-mentioned questions also for radioactive isotopes and can therefore be able to contribute valuable results for future nuclear-structure science.

A CLX Input file

The program CLX reads the parameters of a calculation from an input file. As an example, a file from the calculation for the nucleus ^{154}Sm is shown in the following. Since the Coulex calculations consist of many steps, this file does not represent the complete calculation process.

```
154Sm -> C @570 MeV
11101111
9 2 2.
0.      0.      0.
6      154
62     12
534.158
0.001 180.  1
1 0 0.0      1 0
2 2 0.082    1 0
3 4 0.267    1 0
4 6 0.543    1 0
5 8 0.903    1 0
6 0 1.099    1 0
7 2 1.177    1 0
8 4 1.337    1 0
9 2 1.440    1 2
1 1 0.0      0
1 2 2.0765   2
1 3 0.552    4
1 4 0.0      2
1 5 0.0      2
1 6 0.0      0
1 7 0.0890   2
1 8 0.0      4
1 9 0.2163   2
2 2 -2.466   2
2 3 3.287    2
2 4 0.0      2
```

2	5	0.0	2
2	6	0.2341	2
2	7	-0.1332	2
2	8	0.1186	2
2	9	0.2790	2
3	3	-2.917	2
3	4	4.29	2
3	5	0.0	4
3	6	0.0	2
3	7	0.1796	2
3	8	-0.1581	2
3	9	0.0935	2
4	4	-2.466	2
4	5	5.15	2
4	6	0.0	2
4	7	0.0	2
4	8	0.1706	2
5	5	-2.466	2
5	6	0.0	2
5	7	0.0	4
5	8	0.0	2
5	9	0.0	2
6	6	0.0	2
6	7	-2.01	2
6	8	0.0	2
6	9	0.0	2
7	7	-2.466	2
7	8	3.21	2
7	9	0.0	2
8	8	-2.466	2
8	9	0.0	2
9	9	-2.466	2
9	10	0.0	2
10	10	-2.466	2

B Figures and Tables on the Analyses

This section contains additional information on the data analysis. This includes sum and coincidence spectra shown in more detail and the numbers on the γ -ray intensities and the Coulex yields of the excited states. The numbers and their uncertainties in the tables represent intermediate data. Numbers have not been subject to further rounding prior to the completion of the final results.

B.1 ^{130}Ba experiment

Table B.1.: Intensities of the transitions in the ^{130}Ba experiment

E_γ	J_i^π	J_f^π	I_γ	dI_γ	$\frac{dI_\gamma}{I_\gamma}$
357	2_1^+	0_1^+	1000000.00	3654.62	0.37%
544	4_1^+	2_1^+	13663.48	707.36	5.18%
551	2_2^+	2_1^+	16450.81	750.03	4.56%
569	4_2^+	2_2^+	296.37	9.96	3.36%
575	4_2^+	4_1^+	171.51	9.61	5.60%
576	5^-	6_1^+	56.50	3.56	6.30%
649	2_3^+	2_2^+	15.65	3.56	22.76%
692	6_1^+	4_1^+	174.91	6.76	3.86%
908	2_2^+	0_1^+	11536.25	38.76	0.34%
1011	3^-	2_2^+	122.71	10.55	8.60%
1017	3^-	4_1^+	1539.70	13.01	0.85%
1120	4_2^+	2_1^+	196.64	8.66	4.40%
1200	2_3^+	2_1^+	39.52	4.29	10.86%
1266	5^-	4_1^+	77.78	5.64	7.25%
1361	2269	2_2^+	49.75	9.10	18.30%
1463	1819	2_1^+	86.49	6.10	7.06%

to be continued

Intensities of the transitions in the ^{130}Ba experiment (*continued*)

E_γ	J_i^π	J_f^π	I_γ	dI_γ	$\frac{dI_\gamma}{I_\gamma}$
357	2_1^+	0_1^+	1000000.00	3654.62	0.37%
1557	2_3^+	0_1^+	<9.41		
1561	3^-	2_1^+	911.40	25.62	2.81%
1912	2269	2_1^+	30.28	7.37	24.35%
2014	2371	2_1^+	190.76	14.73	7.72%
2269	2269	0_1^+	34.16	4.30	12.60%
1819	1819	0_1^+	<25.71		
2371	2371	0_1^+	<15.29		

^aEstimate

^bPeak appears in spectrum coincident to $2_1^+ \rightarrow 0_1^+$ transition. The transition could not be assigned. A state at an energy of 2686 keV is assumed.

Table B.2.: Yields of the states in the ^{130}Ba experiment

J^π	E_x	Y	dY	Y_{rel}	dY_{rel}	$\frac{dY_{\text{rel}}}{Y_{\text{rel}}}$
2_1^+	357	994630.63	3889.63	1.000×10^0	3.911×10^{-3}	0.39%
4_1^+	902	11699.57	707.60	1.176×10^{-2}	7.129×10^{-4}	6.06%
2_2^+	908	27502.58	751.24	2.765×10^{-2}	7.630×10^{-4}	2.76%
4_2^+	1477	664.51	16.32	6.681×10^{-4}	1.662×10^{-5}	2.49%
2_3^+	1557	64.57	5.58	5.546×10^{-5}	5.612×10^{-6}	10.12%
6_1^+	1592	174.91	6.76	1.759×10^{-4}	6.827×10^{-6}	3.88%
2^{+b}	1819	86.49	6.10	8.695×10^{-5}	6.145×10^{-6}	7.07%
5_1^-	2168	134.28	6.67	1.350×10^{-4}	6.729×10^{-6}	4.98%
2^{+b}	2269	114.20	12.48	1.148×10^{-4}	1.256×10^{-5}	10.94%
2^{+b}	2371	190.76	14.73	1.918×10^{-4}	1.483×10^{-5}	7.73%

^aUpper limit

^bAssumption used in the calculations

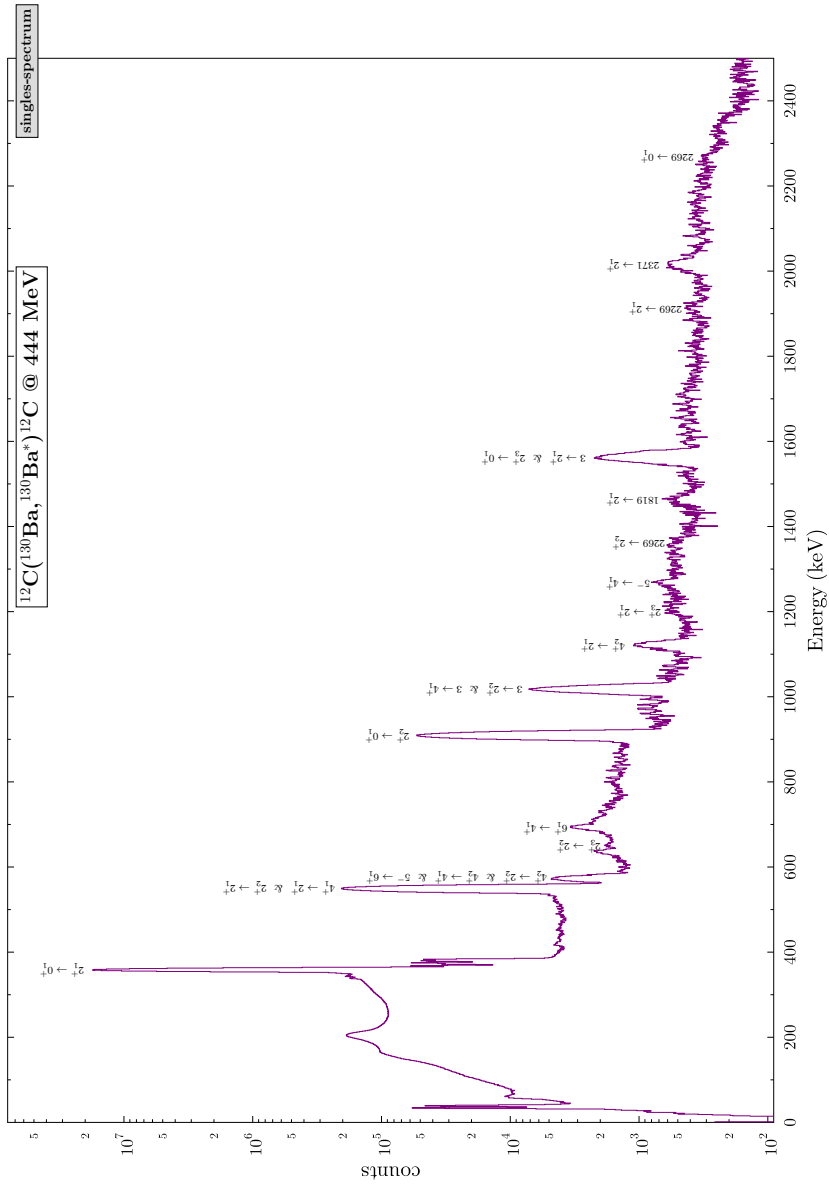


Figure B.1.: Singles Sum Spectrum of the ^{130}Ba experiment.

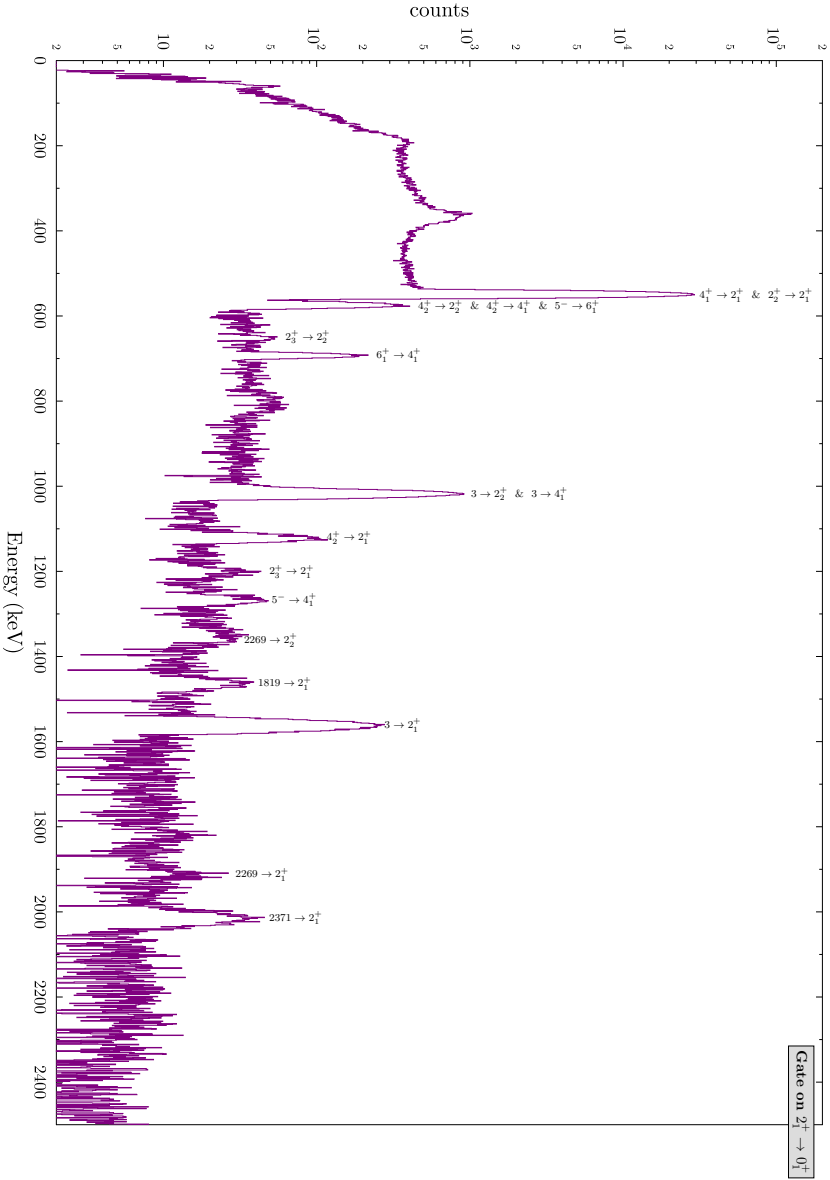


Figure B.2.: Spectrum of the ^{130}Ba experiment coincident to the $2_1^+ \rightarrow 0_1^+$ transition.

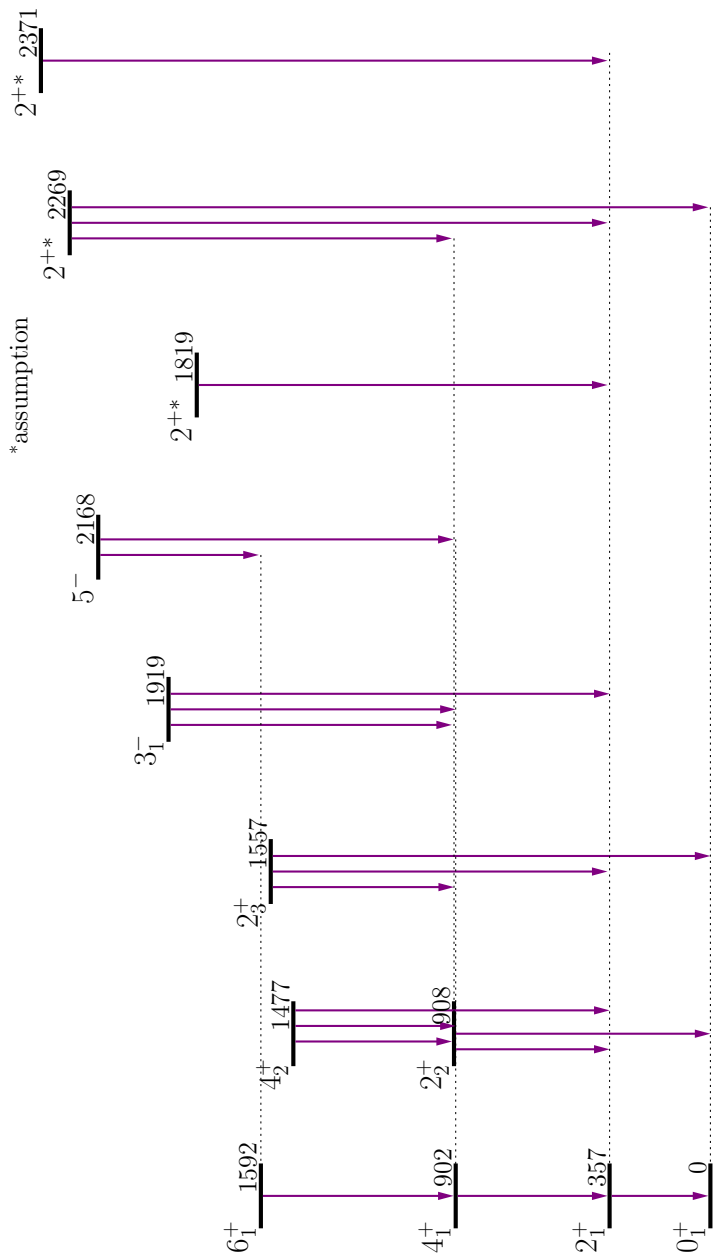


Figure B.3: Level scheme of the excited states and connecting transitions observed in the ^{130}Ba experiment.

B.2 ^{132}Ba experiment

Table B.3.: Intensities of the transitions in the ^{132}Ba experiment

E_γ	J_i^π	J_f^π	I_γ	dI_γ	$\frac{dI_\gamma}{I_\gamma}$
465	2_1^+	0_1^+	1000000.00	2902.26	0.29%
383	3_1^-	2_3^+	37.67	1.90	5.03%
567	2_2^+	2_1^+	10823.33	30.70	0.28%
602	4_2^+	4_1^+	46.63	3.78	8.11%
654	2_3^+	2_2^+	17.93	3.54	19.77%
663	4_1^+	2_1^+	8362.09	24.09	0.29%
698	4_2^+	2_2^+	134.47	7.87	5.85%
805	6_1^+	4_1^+	52.89	3.42	6.46%
817	(4_1^+)	4_1^+	57.71	3.49	6.04%
941	3_1^-	4_1^+	137.60	4.59	3.33%
966	2_4^+	2_2^+	79.57	5.67	7.12%
1032	2_2^+	0_1^+	6108.00	32.63	0.53%
1037	3_1^-	2_2^+	170.88	8.98	5.26%
1039	0_2^+	2_1^+	30.93 ^a	10.24	33.09%
1046	3_1^+	2_1^+	31.06 ^a	10.28	33.09%
1221	2_3^+	2_1^+	108.58	4.48	4.12%
1265	4_2^+	2_1^+	56.18	5.56	9.90%
1311	$2^+ - 6^+$	4_1^+	80.75	5.81	7.20%
1534	2_4^+	2_1^+	309.53	7.15	2.31%
1604	3_1^-	2_1^+	2038.08	13.29	0.65%
1686	2_3^+	0_1^+	0.90	0.10	10.88%
1804	$0_4^+?$	2_1^+	44.12	4.26	9.66%
1909	3_2^-	2_1^+	74.82	5.74	7.68%
~1930		2_1^+	79.24	5.36	6.76%
1974	$2^+ - 6^+$	2_1^+	20.41	2.84	13.93%
1998	2_4^+	0_1^+	95.92	6.58	6.86%
~2222 ^b	2686	2_1^+	49.40	4.08	8.25%
~2400		0_1^+	<15.4		
2439	$2^+ - 6^+$	0_1^+	<12.6		
2686	2686	0_1^+	<30.3		

^aEstimate

^bPeak appears in spectrum coincident to $2_1^+ \rightarrow 0_1^+$ transition. The transition could not be assigned. A state at an energy of 2686 keV is assumed.

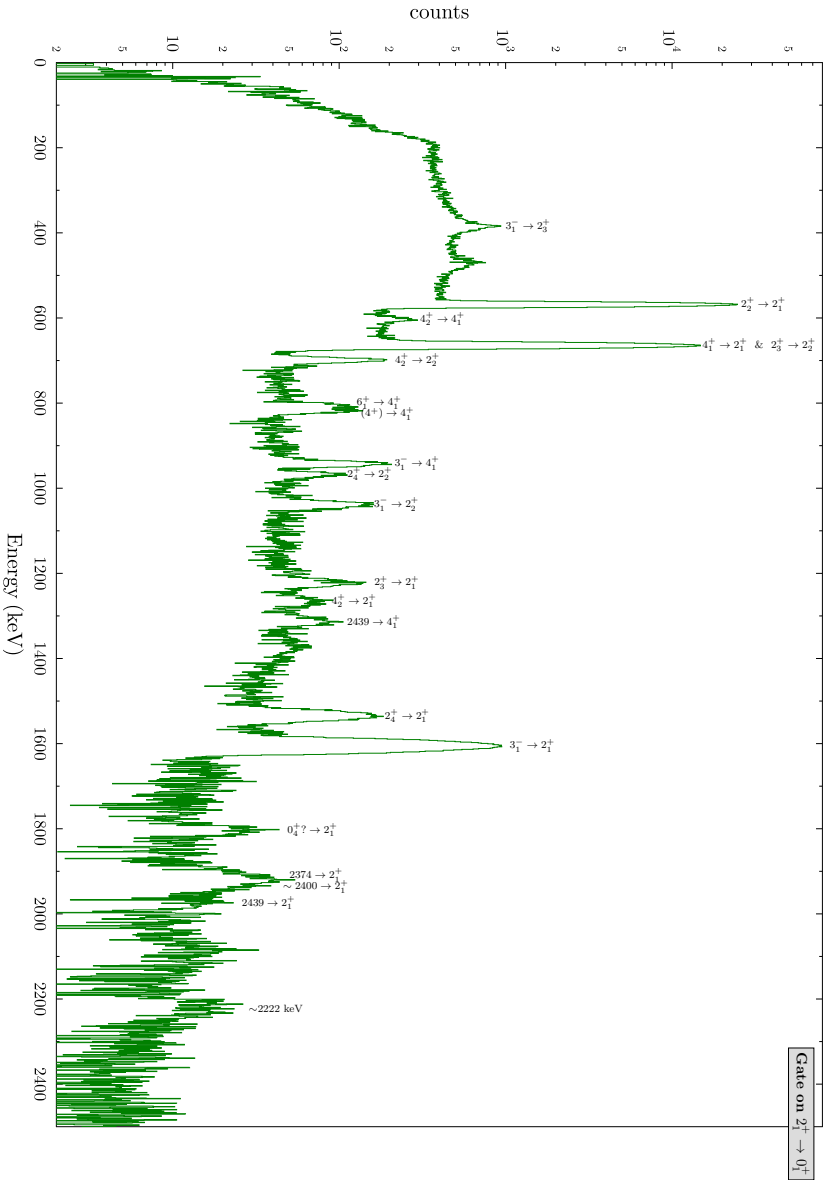


Figure B.5.: Spectrum of the ^{132}Ba experiment coincident to the $2_1^+ \rightarrow 0_1^+$ transition.

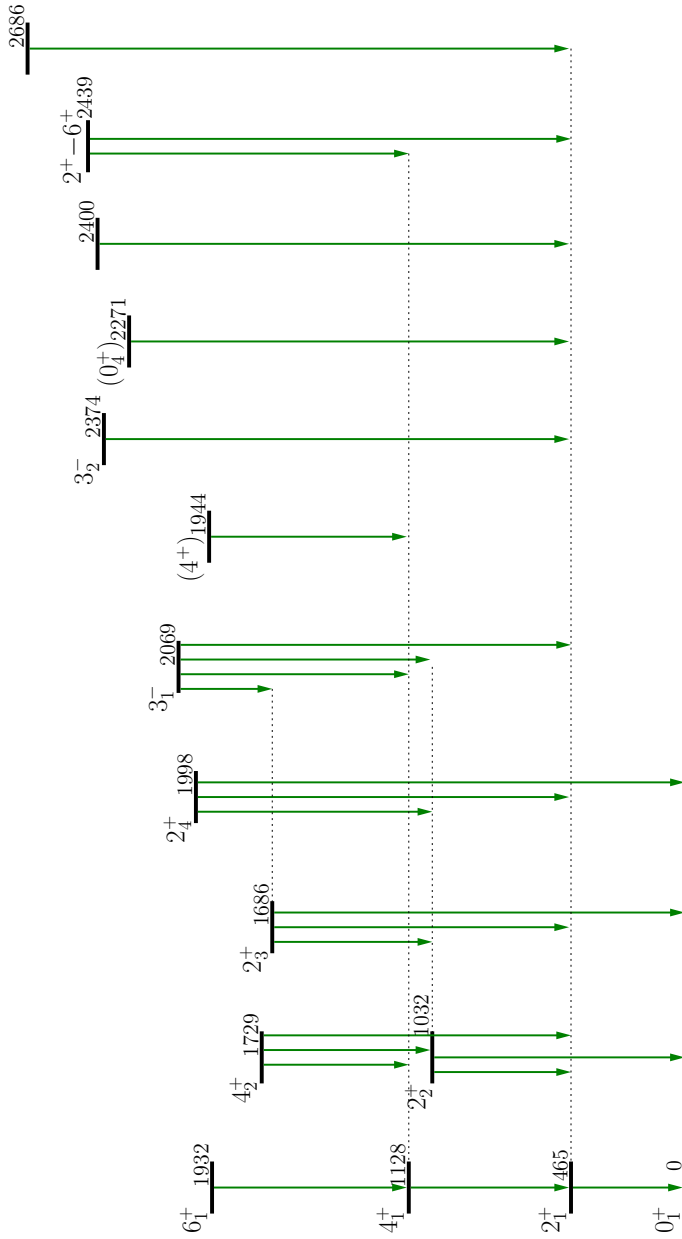


Figure B.6.: Level scheme of the excited states and connecting transitions observed in the ^{132}Ba experiment.

Table B.4.: Yields of the states in the ^{132}Ba experiment

J^π	E_x	Y	dY	Y_{rel}	dY_{rel}	$\frac{dY_{\text{rel}}}{Y_{\text{rel}}}$
2_1^+	465	990017.42	2937.70	1.000×10^0	2.967×10^{-3}	0.30%
2_2^+	1032	16614.94	47.03	1.678×10^{-2}	6.882×10^{-5}	0.41%
4_1^+	1128	8019.72	26.41	8.101×10^{-3}	3.591×10^{-5}	0.44%
0_2^+	1504	— ^c	— ^c			
2_3^+	1686	85.79	4.09	8.665×10^{-5}	4.138×10^{-6}	4.77%
4_2^+	1729	237.90	10.38	2.403×10^{-4}	1.051×10^{-5}	4.37%
6_1^+	1932	52.89	3.42	5.342×10^{-5}	3.455×10^{-6}	6.47%
(4^+)	1944	57.71	3.49	5.830×10^{-5}	3.527×10^{-6}	6.05%
2_4^+	1998	496.76	13.00	5.018×10^{-4}	1.322×10^{-5}	2.63%
3_1^-	2069	2384.22	16.79	2.408×10^{-3}	1.840×10^{-5}	0.76%
0_4^+	2271	44.12	4.26	4.457×10^{-5}	4.308×10^{-6}	9.67%
3_2^-	2374	74.82	5.74	7.558×10^{-5}	5.805×10^{-6}	7.68%
	$\sim 2400^{\text{a}}$	< 94.66	5.89	$< 9.561 \times 10^{-5}$	5.959×10^{-6}	6.23%
$2^+ - 6^+$	2439	< 113.79	6.99	$< 1.149 \times 10^{-4}$	7.702×10^{-6}	6.15%
	2686 ^b	< 79.73	4.74	8.053×10^{-5}	4.794×10^{-6}	5.95%

^aThe literature [Kha05] reports a state at 2406(8) keV with $J^\pi = 0^+$ assignment, although the excitation energy does not fit well.

^bThe transition at ~ 2221 in the spectrum gated on $2_1^+ \rightarrow 0_1^+$ transition could not be assigned. An estimate of a possible 2^+ state at 2686 keV has been done.

^cThe reported decays of the 0_2^+ state of 472 keV and 1039 keV have been hidden in the peaks of the strong transitions $2_1^+ \rightarrow 0_1^+$ and $3_1^- \rightarrow 2_2^+$, respectively. The yield of the 0_2^+ state could not be determined.

B.3 ^{154}Sm experiment

Table B.5.: Intensities of the transitions in the ^{154}Sm experiment

E_γ	J_i^π	J_f^π	I_γ	dI_γ	$\frac{dI_\gamma}{I_\gamma}$
82	2_1^+	0_1^+	- ^a	-	-
159	4_2^+	2_2^+	- ^a	-	-
185	4_1^+	2_1^+	- ^a	-	-
257	2_2^+	1_1^-			
276	6_1^+	4_1^+	31380.29	2540.99	8.10%
359	8_1^+	6_1^+	1324.37	81.42	6.15%
375	1815	2_4^+	460.08	25.53	5.55%
431	10_1^+	8_1^+	67.67	10.69	15.79%
529	7_1^-	8_1^+	94.75	8.59	9.06%
555	1_2^-	1_1^-			
638	5_1^-	6_1^+	1304.45	31.74	2.43%
745	3_1^-	4_1^+	6206.11	107.16	1.73%
794	4_2^+	6_1^+	343.60	24.63	7.17%
839	1_1^-	2_1^+	6133.71	94.35	1.54%
888	7_1^-	6_1^+	401.85	28.55	7.10%
911	2_2^+	4_1^+	6270.39	159.50	2.54%
914	5_1^-	4_1^+	5388.98	152.45	2.83%
921	1_1^-	0_1^+	4764.48	187.46	3.93%
930	3_1^-	2_1^+	9848.64	197.98	2.01%
1003	2015	3_1^-	259.65	23.08	8.89%
1017	0_2^+	2_1^+	9106.33	150.64	1.65%
1070	4_2^+	4_1^+	1309.79	88.67	6.77%
1096	2_2^+	2_1^+	8698.12	156.98	1.80%
1122	4_3^+	6_1^+	150.30	12.85	8.55%
1173	2_4^+	4_1^+	1388.38	96.92	6.98%
1178	2_2^+	0_1^+	5568.18	160.95	2.89%
1204	1286	2_1^+	272.31	13.21	4.85%
1231	5_2^-	6_1^+	620.71	44.29	7.14%
1255	4_2^+	2_1^+	1635.56	63.20	3.86%
1272	3_1^+	4_1^+	86.48	8.61	9.96%
1318	3_2^-	4_1^+	4221.64	97.71	2.31%
1358	2_4^+	2_1^+	25818.44	606.67	2.35%
1394	1_2^-	2_1^+	2533.66	63.77	2.52%
1398	4_3^+	4_1^+	1062.77	25.78	2.43%
1433	1515	2_1^+	2675.20	69.17	2.59%

to be continued

Intensities of the transitions in the ^{154}Sm experiment (*continued*)

E_γ	J_i^π	J_f^π	I_γ	dI_γ	$\frac{dI_\gamma}{I_\gamma}$
1440	2_4^+	0_1^+	20760.67	525.66	2.53%
1440	1707	4_1^+	418.37	41.74	9.98%
1457	3_1^+	2_1^+	219.04	17.92	8.18%
1503	3_2^-	2_1^+	1128.71	32.68	2.90%
1507	5_2^-	4_1^+	317.68	25.94	8.16%
1549	1815	4_1^+	418.04	32.93	7.88%
1583	4_3^+	2_1^+			
1933	2015	2_1^+	712.23	87.48	12.28%
2057	2139	2_1^+	507.25	29.71	5.86%
2139	2139	0_1^+	288 ^b	17 ^b	5.90%

^aIn this energy range the efficiency could not be determined with sufficient accuracy.

^bIntensity deduced from branching ratio given in Nuclear Data Sheets [Rei09].

Table B.6.: Yields of the states in the ^{154}Sm experiment

J^π	E_x	Y	dY	Y_{rel}	dY_{rel}
2_4^+	1440.05	47507.40	808.01	1.00×10^0	2.41×10^{-2}
2_1^+	82	- ^a	-	- ^a	-
4_1^+	267	- ^a	-	- ^a	-
6_1^+	543	29367.74	2543.20	6.18×10^{-1}	5.46×10^{-2}
8_1^+	902.6	1205.25	100.70	2.54×10^{-2}	2.16×10^{-3}
1_1^-	921.4	10697.49	210.54	2.25×10^{-1}	5.86×10^{-3}
3_1^-	1012.4	15795.10	226.30	3.32×10^{-1}	7.39×10^{-3}
0_2^+	1099.3	9106.33	150.64	1.92×10^{-1}	5.59×10^{-3}
2_2^+	1177.8	20536.68	275.66	4.32×10^{-1}	9.37×10^{-3}
5_1^-	1180.7	6693.43	184.19	1.41×10^{-1}	4.56×10^{-3}
2_3^+	1286.4	272.31	13.21	5.75×10^{-3}	2.96×10^{-4}
10_1^+	1332.8	67.67	10.69	1.42×10^{-3}	2.26×10^{-4}
4_2^+	1337.6	3288.95	111.64	6.92×10^{-2}	2.63×10^{-3}
7_1^-	1431	401.85	28.55	8.46×10^{-3}	6.18×10^{-4}
1_2^-	1475.7	2533.66	63.77	5.33×10^{-2}	1.62×10^{-3}
3_1^+	1539.3	305.52	19.89	6.43×10^{-3}	4.33×10^{-4}
3_2^-	1584.6	5350.34	103.03	1.13×10^{-1}	2.89×10^{-3}
4_3^+	1664.9	1413.49	29.89	2.98×10^{-2}	8.07×10^{-4}

to be continued

Yields of the states in the ^{154}Sm experiment (*continued*)

J^π	E_x	Y	dY	Y_{rel}	dY_{rel}
2_4^+	1440.05	47507.40	808.01	1.00×10^0	2.41×10^{-2}
3^+	1706.8	418.37	41.74	8.81×10^{-3}	8.91×10^{-4}
5_2^-	1774.2	938.39	51.33	1.98×10^{-2}	1.13×10^{-3}
$2^+, 3$	1815.1	875.12	41.55	1.84×10^{-2}	8.74×10^{-4}
$1^-, 2^+$	2015.2	971.88	90.47	2.05×10^{-2}	1.90×10^{-3}
$1, 2^+$	2139	795.25	34.23	1.67×10^{-2}	2.50×10^{-3}

^aThe yields of these states could not be determined with sufficient accuracy due to the large uncertainty of the efficiency in the respective energy region.

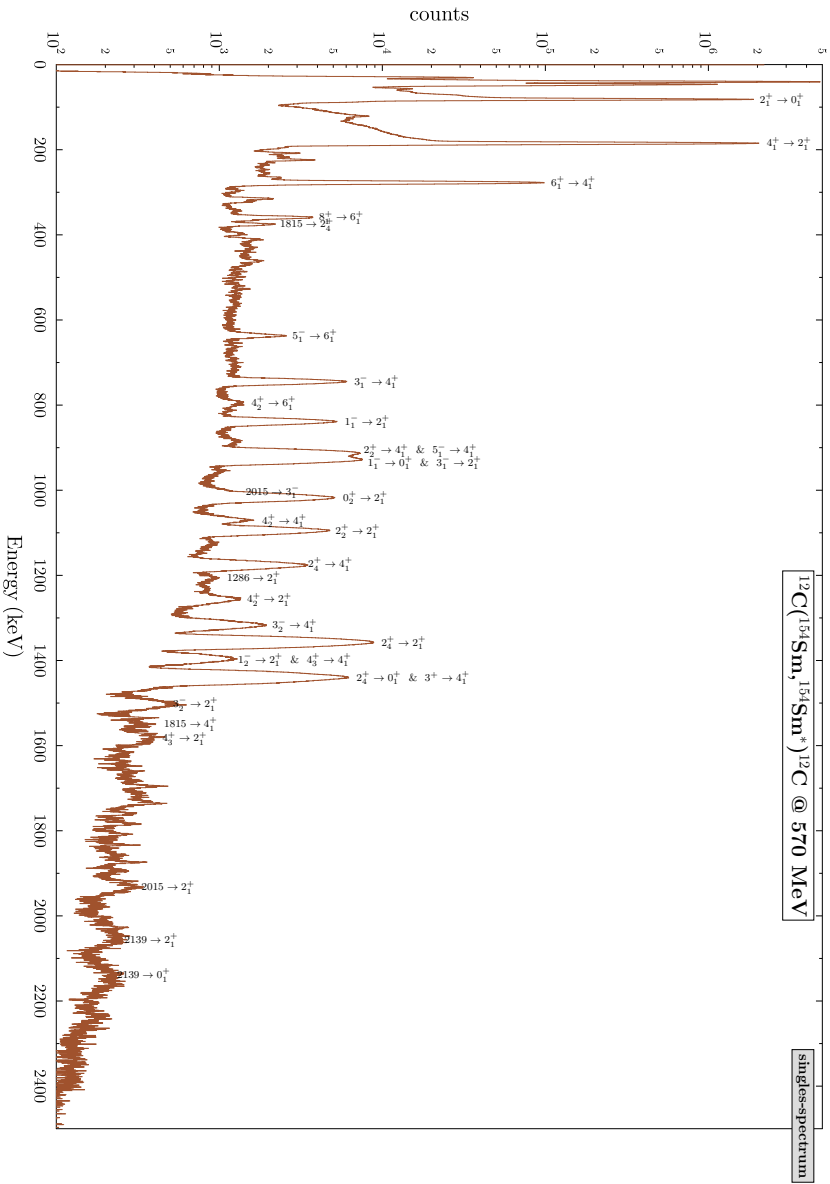


Figure B.7.: Singles Sum Spectrum of the ^{154}Sm experiment.

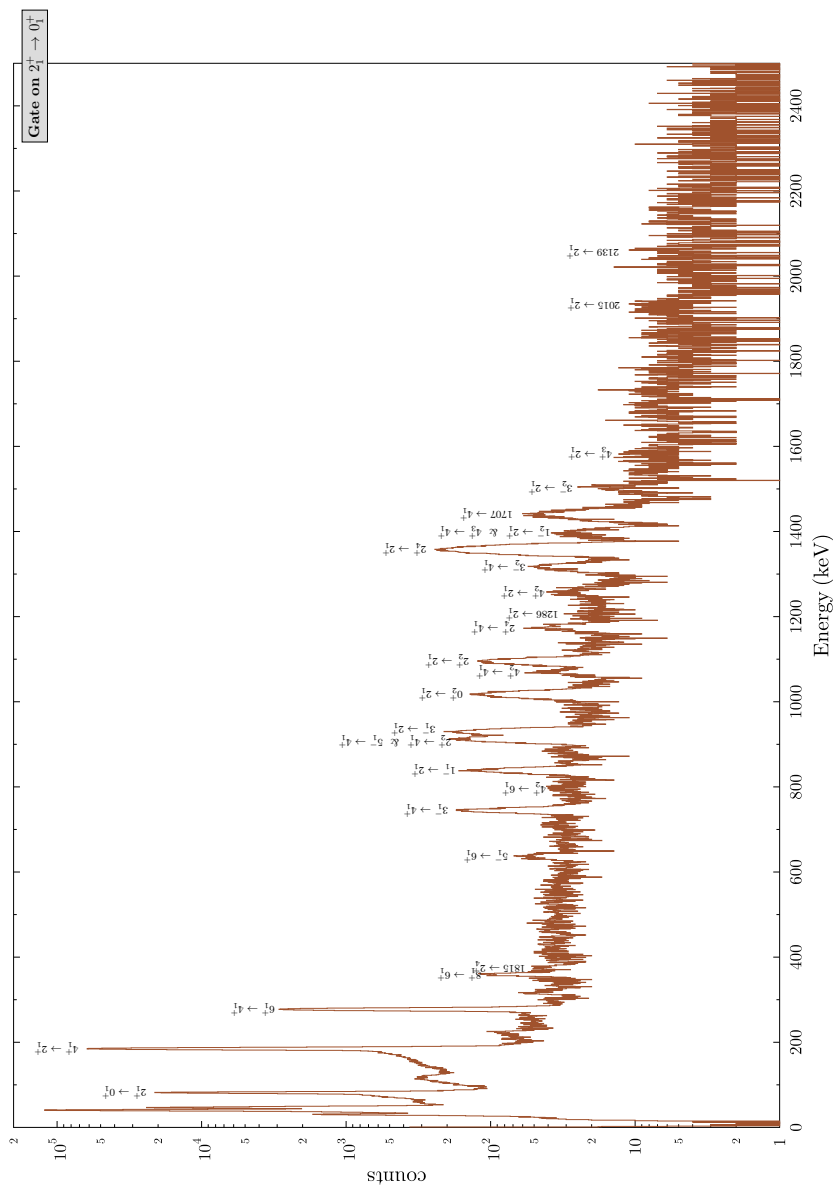


Figure B.8.: Spectrum of the ^{154}Sm experiment coincident to the $2_1^+ \rightarrow 0_1^+$ transition.

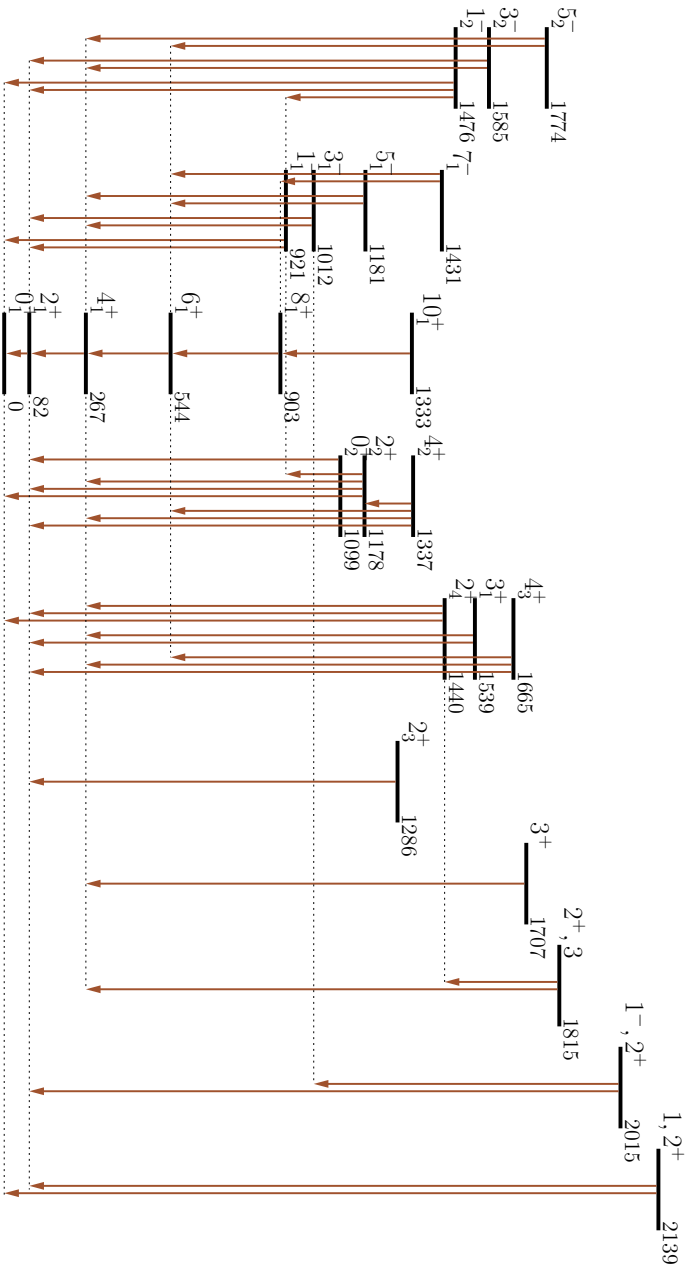
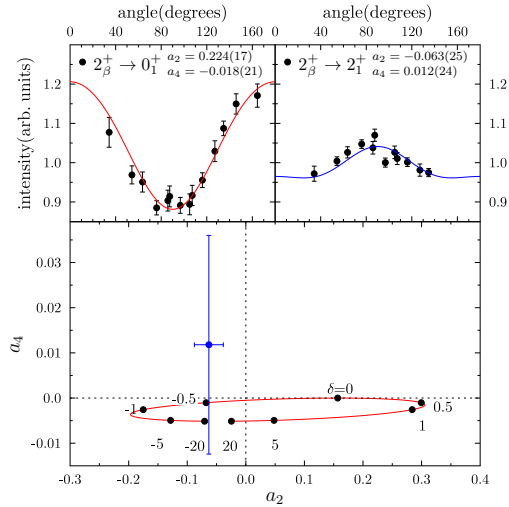
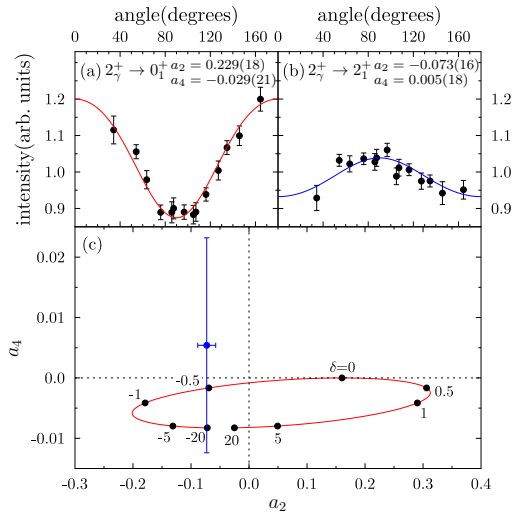


Figure B.9.: Level scheme of the excited states and connecting transitions observed in the ^{154}Sm experiment..



(a) Angular distributions of the $2_2^+ \rightarrow 0_1^+$ and $2_2^+ \rightarrow 2_1^+$ transitions and angular distribution ellipse for $2_2^+ \rightarrow 2_1^+$ transition in ^{154}Sm .



(b) Angular distributions of the $2_4^+ \rightarrow 0_1^+$ and $2_4^+ \rightarrow 2_1^+$ transitions and angular distribution ellipse for $2_4^+ \rightarrow 2_1^+$ transition in ^{154}Sm .

Figure B.10.: Analysis of the angular distributions for the deduction of the mixing ratio δ for the $2_2^+ \rightarrow 2_1^+$ and $2_4^+ \rightarrow 2_1^+$ transitions in ^{154}Sm .

B.4 ¹⁹⁴Pt experiment

Table B.7.: Intensities of the transitions in the ¹⁹⁴t experiment

E_γ	J_i^π	J_f^π	I_γ	dI_γ	$\frac{dI_\gamma}{I_\gamma}$
328	2^+_1	0^+_1	1000000,00	2742,40	0,27%
172	3^-_4	J^π	47.73	4.41	9.24%
203	3^-_1	4^+_2	242.63	28.55	11.77%
294	2^+_2	2^+_1	9307.08	51.22	0.55%
301	3^+_1	2^+_2	279.69	7.07	2.53%
305	3^-_2	3^-_1	24.48	1.77	7.22%
364	3^-_2	5^-_1	6.14	0.57	9.23%
365	1^-_1	3^-_1	6.19	0.68	10.96%
399	$(1^+, 2^+)_2$	$(2, 3^-, 4)$	9.59	0.63	6.59%
418	4^+_2	4^+_1	89.06	4.40	4.94%
456	$(2, 3^-, 4)$	3^-_1	34.55	1.59	4.59%
482	(4^+)	3^-_1	37.1	1.7	4.52%
499	$(3, 4)^+$	3^+_1	60.24	2.66	4.42%
509	3^-_4	3^-_2	19.35	2.77	14.33%
510	3^-_1	3^+_1			
562	$(5^-)_1$	4^+_1	187.31	9.15	4.88%
589	2^+_3	3^+_1	27.68	1.31	4.72%
594	3^+_1	2^+_1	67.98	3.74	5.50%
600	6^+_1	4^+_1	127.20	6.24	4.90%
607	4^+_2	2^+_2	876.99	20.95	2.39%
621	3^-_1	4^+_1	796.96	38.74	4.86%
622	2^+_2	0^+_1	1274.10 ^a	28.67 ^a	2.25%
645	0^+_2	2^+_2	16.98	0.66	3.89%
699	2^+_4	3^+_1	14.13	0.75	5.33%
724	3^-_3	3^-_1	51.66	2.39	4.62%
769	3^-_5	$(1)^+$			
782	3^-_3	$(5^-)_1$	8.30	0.52	6.23%
810	3^-_1	2^+_2	165.15 ^a	6.36 ^a	3.85%
815	3^-_2	3^+_1	9.80 ^{ac}	2.12 ^{ac}	21.64%
816	3^-_4	3^-_1	302.92	12.36	4.08%
855	$(1)^+_1$	3^+_1	9.73 ^{ac}	0.73 ^{ac}	7.52%
889	2^+_3	2^+_2	17.25	1.11	6.45%
894	$(2)^+$	3^+_1	10.57	0.80	7.56%
901	4^+_2	2^+_1	80.93	2.67	3.30%
914	$(1^+, 2^+)_2$	$(5^-)_1$	8.76	0.57	6.48%

to be continued

Intensities of the transitions in the ^{194}Pt experiment (*continued*)

E_γ	J_i^π	J_f^π	I_γ	dI_γ	$\frac{dI_\gamma}{I_\gamma}$
328	2_1^+	0_1^+	1000000,00	2742,40	0,27%
925	0_4^+	2_2^+	50.22	1.70	3.38%
938	0_2^+	2_1^+	8.37 ^a	0.36 ^a	4.28%
990	(4^+)	3_1^+	5.2	0.5	8.71%
1000	2_4^+	2_2^+	141.69	3.56	2.51%
1048	2_5^+	2_2^+	56.29	1.87	3.32%
1058	$(1^+, 2^+)_2$	4_2^+	71.34	8.28	11.61%
1080	$(1^+, 2^+)_1$	3_1^+	10.14	0.62	6.07%
1102	(4^+)	4_1^+	8.3	0.7	8.30%
1104	3_1^-	2_1^+	2039.47	10.08	0.49%
1005	$(2)_1^+$	4_1^+	<3.7		
1114	3_5^-	3_1^-	113.47	5.17	4.55%
1150	J^π	3_1^+	12.22	0.76	6.20%
1150	0_3^+	2_1^+	<2.29		
1156	$(1)_1^+$	2_2^+	67.08	2.63	3.91%
1183	2_3^+	2_1^+	66.89	2.07	3.09%
1194	$(2)_1^+$	2_2^-	<10.0		
1218	0_4^+	2_1^+	171.49	3.31	1.93%
1232	3_3^-	3_1^+	51.30	2.37	4.62%
1261	J^π	4_1^+	9.82	0.68	6.90%
1292	(4^+)	2_2^+	33.2	1.5	4.60%
1314	3_5^-	4_2^+	98.73	11.25	11.40%
1324	3_4^-	3_1^+	22.77	1.40	6.14%
1342	2_5^+	2_1^+	97.21	1.57	1.61%
1343	3_3^-	4_1^+	23.79	1.27	5.34%
1365	$(1^+, 2^+)_2$	3_1^+	53.15	2.74	5.15%
1432	3_1^-	0_1^+	67.29 ^a	6.14 ^a	9.13%
1451	J^π	2_2^+	18.31	1.15	6.29%
1468	1_1^-	2_1^+	27.35	1.64	5.98%
1488	$(2)_1^+$	2_1^+	6.83	0.96	14.036%
1512	2_3^+	0_1^+	4.48 ^a	1.15 ^a	25.62%
1532	3_3^-	2_2^+	61.29	1.78	2.91%
1622	2_4^+	0_1^+	135 ^a	10 ^a	8.16%
1624	3_4^-	2_2^+	27.70	1.17	4.22%
1624	3_5^-	3_1^+	9.34	0.74	7.96%
1665	$(1^+, 2^+)_2$	2_2^-	40.60	1.49	3.66%
1670	2_5^+	0_1^+	13.51 ^a	0.74 ^a	5.47%
1675	$(1^+, 2^+)_1$	2_1^+	129.93	7.60	5.85%

to be continued

Intensities of the transitions in the ^{194}Pt experiment (*continued*)

E_γ	J_i^π	J_f^π	I_γ	dI_γ	$\frac{dI_\gamma}{I_\gamma}$
328	2_1^+	0_1^+	1000000,00	2742,40	0,27%
1744	J^π	2_1^+	18.85	1.80	9.56%
1816	$(2)^+$	0_1^+	<16.5		
1826	3_3^-	2_1^+	18.99	1.33	7.02%
1924	3_5^-	2_2^+	154.35	4.20	2.72%
1959	$(1^+, 2^+)_2$	2_1^+	13.70	1.7	12.440%
2004	$(1^+, 2^+)_1$	0_1^+	<21.0		
2072	J^π	0_1^+	35.17	4.06	11.531%
2218	3_5^-	2_1^+	116.54	3.41	2.92%
2287	$(1^+, 2^+)_2$	0_1^+	<7.7		

^aIntensity deduced from branching ratio given in Nuclear Data Sheets

^bIntensity deduced by subtraction of doublet-peak areas in different coincidence spectra.

^cDoublet peaks are assumed, although no transition can be assigned to second peak. Treated as direct decay into 3_1^+ , yield unchanged within uncertainties.

^dThis peak does not seem to originate from ^{194}Pt . It shows no conclusive coincidence relation to transitions of ^{194}Pt . The origin of this peak could not be determined.

^eThis peak does not seem to originate from ^{194}Pt . Peak appears in spectrum coincident to $4_1^+ \rightarrow 2_1^+$ transition, but not in spectrum coincident to $2_1^+ \rightarrow 0_1^+$. The width of the peak does not meet the expectations. The origin of this peak could not be determined.

^fPeak appears in spectrum coincident to $2_1^+ \rightarrow 0_1^+$ transition. The transition could not be assigned.

^gPeak appears in spectrum coincident to $2_2^+ \rightarrow 2_1^+$ transition. The transition could not be assigned.

^hPeak appears in spectrum coincident to $4_1^+ \rightarrow 2_1^+$ transition. The transition could not be assigned.

ⁱThe number of transitions represented by this peak could not be determined conclusively.

^jPeak appears in spectrum coincident to $3_1^- \rightarrow 2_1^+$ transition. The transition could not be assigned.

^kPeak appears in spectrum coincident to $3_1^+ \rightarrow 2_2^+$ transition. The transition could not be assigned.

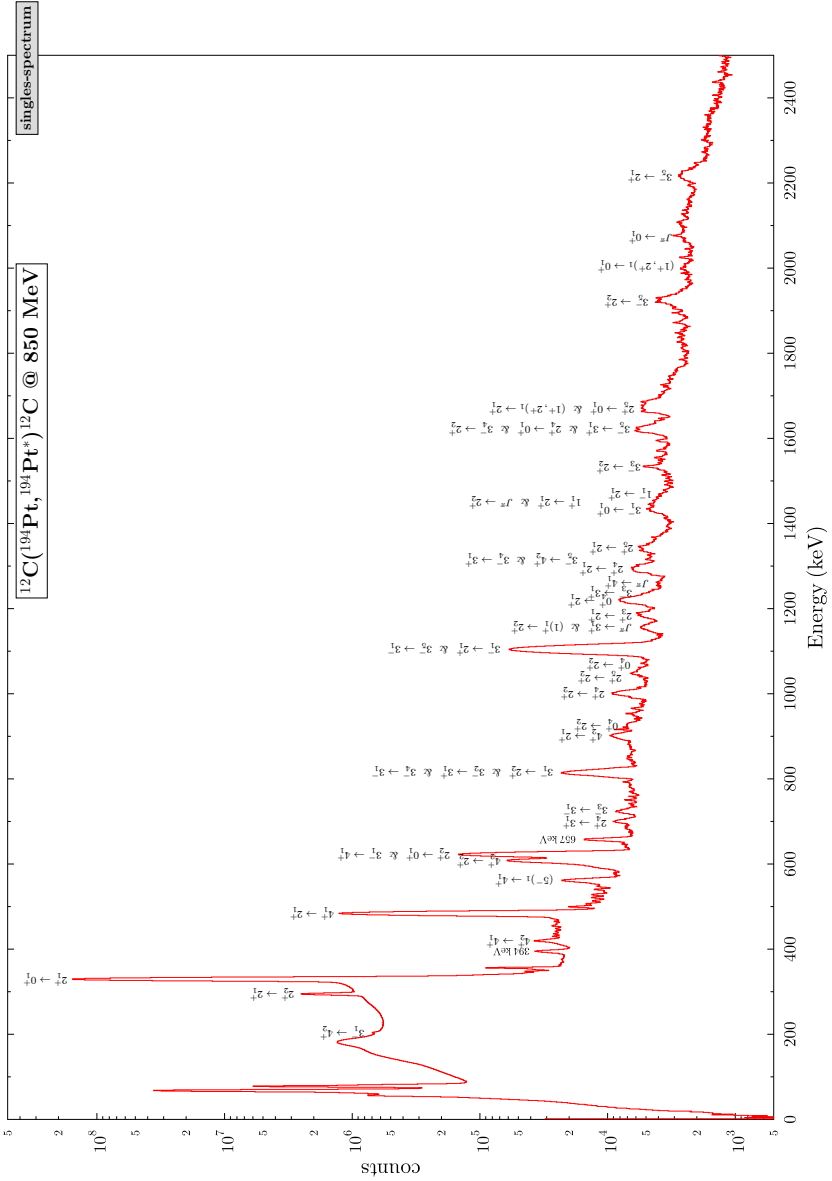


Figure B.11.: Singles Sum Spectrum of the ^{194}Pt experiment.

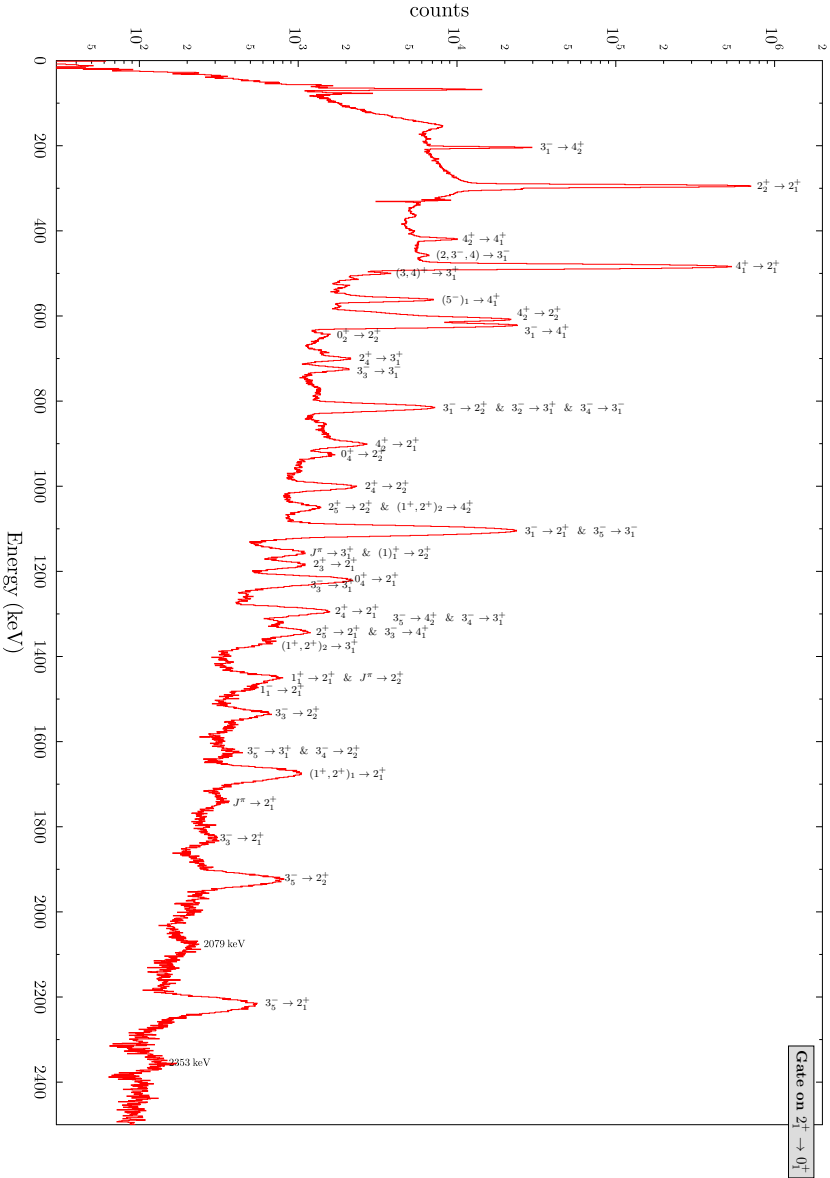


Figure B.12.: Spectrum of the ^{194}Pt experiment coincident to the $2_1^+ \rightarrow 0_1^+$ transition.

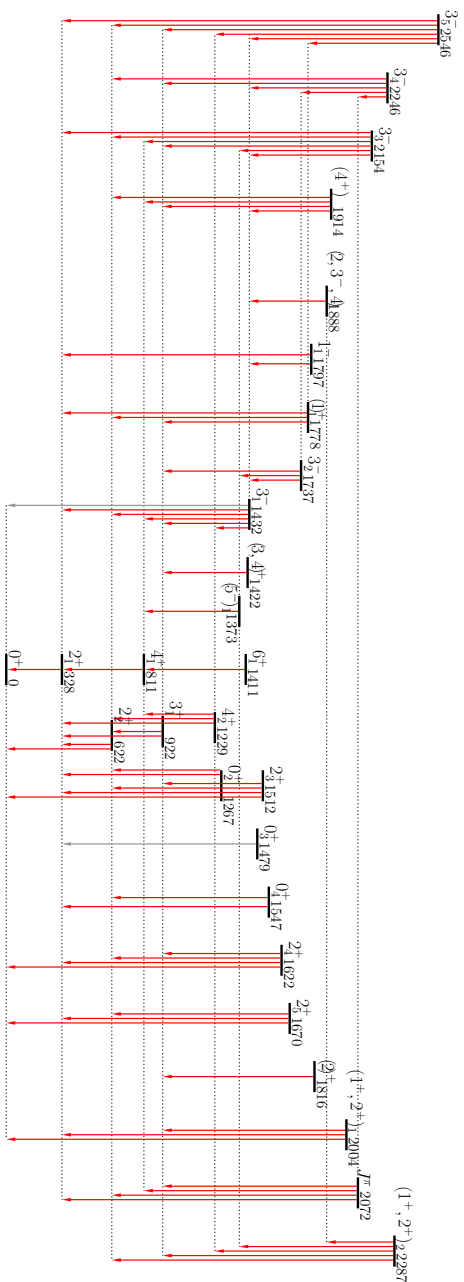


Figure B. 14.: Level scheme of the excited states and connecting transitions observed in the ^{194}Pt experiment.

Table B.8.: Yields of the states in the ^{194}Pt experiment

J^π	E_x (keV)	Y	dY	Y_{rel}	dY_{rel}	$\frac{dY_{\text{rel}}}{Y_{\text{rel}}}$ (%)
2_1^+	328	1049631.21	2743.62	1.00×10^0	2.61×10^{-3}	0.26
2_2^+	622	9578.86	68.33	9.13×10^{-3}	6.93×10^{-5}	0.76
4_1^+	811	12096	76	1.150×10^{-2}	7.80×10^{-5}	0.68
3_1^+	922	95.19	10.31	9.07×10^{-5}	9.83×10^{-6}	10.84
4_2^+	1229	705.62	37.51	6.72×10^{-4}	3.58×10^{-5}	5.32
0_2^+	1267	25.58	0.76	2.44×10^{-5}	7.26×10^{-7}	2.98
5_1^-	1373	164.11	9.20	1.56×10^{-4}	8.77×10^{-6}	5.61
6_1^+	1411	127.20	6.24	1.21×10^{-4}	5.95×10^{-6}	4.91
$(3, 4)^+$	1422	60.24	2.66	5.74×10^{-5}	2.54×10^{-6}	4.42
3_1^-	1432	2794.73	52.93	2.66×10^{-3}	5.09×10^{-5}	1.91
0_3^+	1479	<2.32		$<2.21 \times 10^{-6}$		
2_3^+	1512	112.63	2.71	1.07×10^{-4}	2.59×10^{-6}	2.42
0_4^+	1547	221.71	3.72	2.11×10^{-4}	3.59×10^{-6}	1.70
2_4^+	1622	436.45	15.27	3.74×10^{-4}	1.04×10^{-5}	2.80
2_5^+	1670	167.62	2.56	1.60×10^{-4}	2.48×10^{-6}	1.55
3_2^-	1737	40.42	2.82	3.85×10^{-5}	2.69×10^{-6}	6.98
$(1)_1^+$	1778	124.75	4.85	1.19×10^{-4}	4.63×10^{-6}	3.89
1_1^-	1797	33.53	1.77	3.19×10^{-5}	1.69×10^{-6}	5.29
$(2)^+$	1816	17.40	1.25	1.66×10^{-5}	1.19×10^{-6}	7.17
$(2, 3^-, 4)$	1888	34.55	1.59	3.29×10^{-5}	1.51×10^{-6}	4.60
(4^+)	1914(1)	83.77	2.41	7.98×10^{-5}	2.30×10^{-6}	2.88
$(1^+, 2^+)_1$	2004	140.07	7.63	1.33×10^{-4}	7.28×10^{-6}	5.45
J^π	2072	49.38	2.27	8.05×10^{-5}	2.16×10^{-6}	4.60
3_3^-	2154	215.33	4.26	2.05×10^{-4}	4.43×10^{-6}	5.50
3_4^-	2246	420.47	13.54	4.01×10^{-4}	1.29×10^{-5}	3.23
$(1^+, 2^+)_2$	2287	125.80	3.65	1.20×10^{-4}	3.49×10^{-6}	2.91
3_5^-	2546(2)	492.43	13.53	4.69×10^{-4}	1.29×10^{-5}	2.76

B.5 ¹⁹⁶Pt experiment

Table B.9.: Intensities of the transitions in the ¹⁹⁶Pt experiment

E_γ	J_i^π	J_f^π	I_γ	dI_γ	$\frac{dI_\gamma}{I_\gamma}$
356	2^+_1	0^+_1	1000000.00	2984.43	0.30%
177	3^-_1	5^-_1	55.26	2.97	5.38%
202	2^+_4	0^+_3	2.8 ^a	0.8 ^a	28.57%
226	2^+_3	0^+_2	6.6 ^a	1.6 ^a	24.24%
278	4^+_2	3^+_1	3.86	0.77	19.91%
308	$(3^-, 4^+)_1$	3^-_1	32.43	1.32	4.06%
326	3^+_1	2^+_2	414.61	7.36	1.77%
333	2^+_2	2^+_1	6439.84	113.58	1.76%
347	2^+_3	3^+_1	27.44	3.28	11.97%
379	2174	$2^+(1^-)$	7.01	1.11	15.87%
393	5^-_1	4^+_1	361.16	15.91	4.40%
416	4^+_2	4^+_1	87.40	3.98	4.56%
419	2174	$3^-, 4^+$	12.34	1.20	9.70%
432	3^-_1	3^+_1	188.51	21.91	11.62%
447	0^+_2	2^+_2	46.17	1.78	3.86%
485	$(3^-, 4^+)_1$	5^-_1	44.81	2.12	4.74%
521	4^+_3	3^+_1	43.86 ^b	5.11	11.65%
521	4^+_1	2^+_1	11913.31 ^b	28.59	0.24%
542	2^+_5	0^+_2	9.4 ^a	3.7 ^a	39.36%
570	3^-_1	4^+_1	136.65	5.60	4.10%
589	2^+_4	3^+_1	11.71 ^b	1.97	16.83%
591	$3^+, 4^+$	4^+_2	38.38 ^b	5.97	15.56%
605	4^+_2	2^+_2	463.82	8.32	1.79%
649	6^+_1	4^+_1	102.14	5.17	5.06%
659	3^+_1	2^+_1	18.24 ^a	0.21 ^a	1.13%
662	2^+_5	3^+_1	14.39	1.75	12.18%
673	2^+_3	2^+_2	153.34	3.17	2.06%
677	$(3^-, 4^+)_2$	3^-_1	93.82	3.22	3.43%
727	2174	3^-_1	154.74	20.32	13.13%
728	2^+_4	4^+_1	40.33	2.77	6.86%
758	3^-_1	2^+_2	655.84	20.51	3.13%
780	$2^+(1^-)$	3^+_1	16.45 ^b	2.22	13.52%
780	0^+_2	2^+_1	92.20 ^b	4.52	4.90%
800	2^+_5	4^+_1	9.4 ^a	3.7 ^a	39.36%
814	2084	5^-_1	5.15	1.14	22.09%

to be continued

Intensities of the transitions in the ^{196}Pt experiment (*continued*)

E_γ	J_i^π	J_f^π	I_γ	dI_γ	$\frac{dI_\gamma}{I_\gamma}$
356	2_1^+	0_1^+	1000000.00	2984.43	0.30%
817	3_2^+	3_1^+	9.19	1.38	15.03%
831	$(3^-, 4^+)_2$	4_2^+	56.49	6.38	11.30%
854	$(3^-, 4^+)_2$	5_1^-	160.90	7.16	4.45%
868	$3^+, 4^+$	3_1^+	5.91	1.01	17.01%
878	$(3^-, 4^+)_1$	4_1^+	51.38	2.41	4.70%
916	2_4^+	2_2^+	18.31	0.92	5.03%
938	4_2^+	2_1^+	37.31	2.63	7.04%
977	3_2^-	3_1^-	272.45	28.74	10.55%
989	2_5^+	2_2^+	26.13	1.18	4.51%
1006	$3^+, 4^+$	4_1^+	13.65 ^b	0.95	6.93%
1006	2_3^+	2_1^+	101.64 ^b	4.41	4.34%
1013	2460	3_1^-	21.51	3.13	14.57%
1047	0_3^+	2_1^+	71.53	3.41	4.77%
1063	$(3^-, 4^+)_1$	2_2^+	6.83	0.82	12.04%
1091	3_1^-	2_1^+	2587.89	16.39	0.63%
1107	$2^+(1^-)$	2_2^+	33.52 ^b	4.19	12.51%
1109	$(3^-, 4^+)_2$	3_1^-	30.91 ^b	4.01	12.97%
1150	2597	3_1^-	112.60	6.10	5.42%
1180	2626	3_1^-	82.00	3.18	3.87%
1195	$3, 4^+$	2_2^+	20.39	1.44	7.04%
1249	2_4^+	2_1^+	70.39	3.44	4.89%
1264	2626	2_3^+	29.60	2.45	8.29%
1296	$(1^+, 2^+)_1$	2_2^+	58.42	2.41	4.13%
1297	2174	4_1^+	14.88	0.95	6.41%
1321	2_5^+	2_1^+	113.10	5.28	4.67%
1362	2_3^+	0_1^+	27.6 ^a	5.0 ^a	18.12%
1439	$2^+(1^-)$	2_1^+	451.08	14.13	3.13%
1447	3_1^-	0_1^+	388 ^a	82 ^a	21.13%
1468	0_4^+	2_1^+	132.95	4.61	3.47%
1492	2_6^+	2_1^+	34.52	2.05	5.95%
1576	1932	2_1^+	16.76	1.47	8.75%
1604	2_4^+	0_1^+	14.1 ^a	3.2 ^a	22.70%
1611	2626	3_1^+	20.95	2.78	13.28%
1628	1984	2_1^+	<23.14	0.81	3.50%
1632	$(1^+, 2^+)_2$	2_1^+	50.07	2.27	4.53%
1642	1998	2_1^+	5.49	1.67	30.39%

to be continued

Intensities of the transitions in the ^{196}Pt experiment (*continued*)

E_γ	J_i^π	J_f^π	I_γ	dI_γ	$\frac{dI_\gamma}{I_\gamma}$
356	2_1^+	0_1^+	1000000.00	2984.43	0.30%
1677	2_5^+	0_1^+	189 ^a	68 ^a	35.98%
1734	3_2^-	2_2^+	45.16	3.22	7.14%
1766	2781	3_1^+	11.27	1.97	17.53%
1769	$(3^-, 4^+)_2$	2_1^+	28.59	1.51	5.29%
1795	$2^+(1^-)$	0_1^+	<69.65	7.24	10.39%
1847	1847	0_1^+	<10.81	0.03	0.24%
1863	2878	3_1^+	6.83	1.07	15.62%
1932	1932	0_1^+	<33.44	0.08	0.25%
1938	2626	2_2^+	23.36	3.29	14.07%
1984	1984	0_1^+	<52.50	0.13	0.25%
1988	1988	0_1^+	<56.86	0.14	0.25%
1998	1998	0_1^+	<57.06	0.14	0.25%
2004	2878	4_1^+	9.14	0.98	10.69%
2068	3_2^-	2_1^+	107.52	3.80	3.53%
2270	2626	2_1^+	14.05	1.78	12.70%
2426	2781	2_1^+	26.80	1.93	7.21%
2523	2878	2_1^+	46.83	2.41	5.14%
2626	2626	0_1^+	<24.25	0.07	0.30%
2781	2781	0_1^+	<43.33	0.13	0.31%
2878	2878	0_1^+	<35.78	0.11	0.31%

^aIntensity deduced from branching ratio given in Nuclear Data Sheets [Xia07]

^bIntensity deduced by subtraction of doublet-peak areas in different coincidence spectra.

^fPeak appears in spectrum coincident to $2_1^+ \rightarrow 0_1^+$ transition. The transition could not be assigned.

^gPeak appears in spectrum coincident to $2_2^+ \rightarrow 2_1^+$ transition. The transition could not be assigned.

^hPeak appears in spectrum coincident to $4_1^+ \rightarrow 2_1^+$ transition. The transition could not be assigned.

^jPeak appears in spectrum coincident to $3_1^- \rightarrow 2_1^+$ transition. The transition could not be assigned.

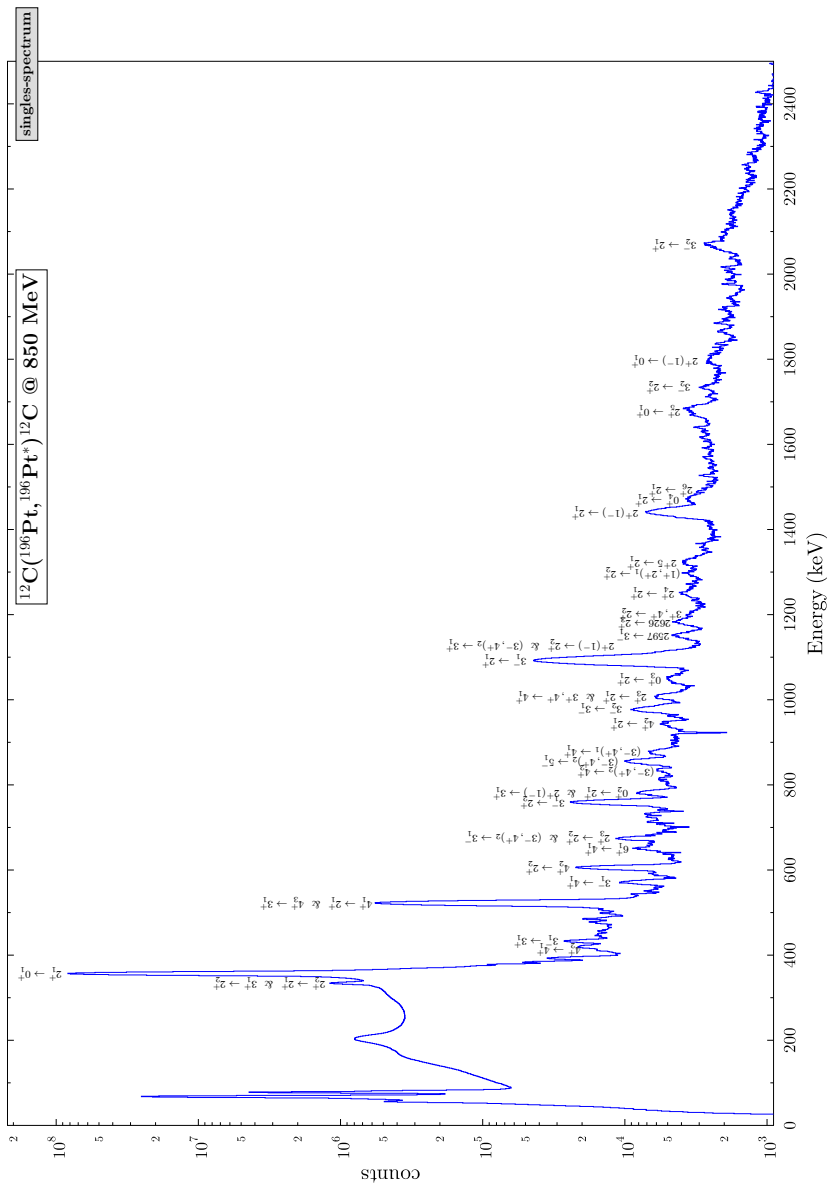


Figure B.15.: Singles Sum Spectrum of the ^{196}Pt experiment.

Table B.10.: Yields of the states in the ^{196}Pt experiment

J^π	E_x	Y	dY	Y_{rel}	dY_{rel}	$\frac{dY_{\text{rel}}}{Y_{\text{rel}}}$
2^+_1	356	1037140.09	3166.99	1.00×10^0	3.05×10^{-3}	0.31%
2^+_2	689	4953.68	124.93	4.776×10^{-3}	1.21×10^{-4}	2.54%
4^+_1	877	11,322.45	34.84	1.092×10^{-2}	4.73×10^{-5}	0.43%
3^+_1	1015	45.01	28.66	4.34×10^{-5}	2.76×10^{-5}	63.68%
0^+_2	1135	140.72	4.91	1.36×10^{-4}	4.76×10^{-6}	3.51%
5^-_1	1270	95.04	17.86	9.16×10^{-5}	1.72×10^{-5}	18.79%
4^+_2	1293	488.74	13.25	4.71×10^{-4}	1.29×10^{-5}	2.73%
2^+_3	1362	262.18	7.19	2.53×10^{-4}	6.98×10^{-6}	2.76%
0^+_3	1402	71.89	3.43	6.93×10^{-5}	3.31×10^{-6}	4.78%
3^-_1	1447	3902.53	212.94	3.76×10^{-3}	2.06×10^{-4}	5.47%
6^+_1	1526	103.52	5.24	9.98×10^{-5}	5.06×10^{-6}	5.07%
4^+_3	1535	43.86	5.11	4.23×10^{-5}	4.93×10^{-6}	11.66%
2^+_4	1604	151.36 ^c	12.44	1.46×10^{-4c}	1.20×10^{-5}	8.22%
2^+_5	1677	393.47 ^c	140.35	3.79×10^{-4c}	1.35×10^{-4}	35.67%
$(3^-, 4^+)_1$	1754	135.45	3.57	1.31×10^{-4}	3.47×10^{-6}	2.65%
$2^+(1^-)$	1795	501.06	14.90	4.83×10^{-4}	1.44×10^{-5}	2.99%
0^+_4	1823	132.95	4.61	1.28×10^{-4}	4.46×10^{-6}	3.48%
3^+	1832	9.19	1.38	8.86×10^{-6}	1.33×10^{-6}	15.03%
2^+_6	1847	34.52	2.05	3.33×10^{-5}	1.98×10^{-6}	5.96%
$3^+, 4^+$	1883	78.34	6.29	7.55×10^{-5}	6.07×10^{-6}	8.04%
$0^+, 1^+, 2^+$	1932	16.76	1.47	1.62×10^{-5}	1.42×10^{-6}	8.76%
$(1^+, 2^+)_1$	1984	134.05	2.41	1.29×10^{-4}	2.36×10^{-6}	1.83%
$(1^+, 2^+)_2$	1988	50.07	2.27	4.83×10^{-5}	2.19×10^{-6}	4.54%
2^+	1998	5.49	1.67	5.29×10^{-6}	1.62×10^{-6}	30.39%
$4^-, 5, 6^-$	2084	5.15	1.14	4.96×10^{-6}	1.10×10^{-6}	22.09%
$(3^-, 4^+)_2$	2124	405.62	21.03	3.91×10^{-4}	2.03×10^{-5}	5.19%
$0^+, 2^+$	2174	188.97	20.41	1.82×10^{-4}	1.97×10^{-5}	10.81%
3^-_2	2423	425.13	29.17	4.10×10^{-4}	2.81×10^{-5}	6.87%
$0^+, 1^+, 2^+$	2460	21.51	3.13	2.07×10^{-5}	3.02×10^{-6}	14.58%
$0, 1^-, 2$	2597	112.60	6.10	1.09×10^{-4}	5.89×10^{-6}	5.43%
$(1, 2, 3)$	2626	169.96	6.15	1.64×10^{-4}	5.95×10^{-6}	3.63%
a	2781	38.07	2.76	3.67×10^{-5}	2.67×10^{-6}	7.26%
b	2878	62.79	2.81	6.05×10^{-5}	2.71×10^{-6}	4.48%

^aThe literature [Xia07] reports a state at 2779(3) keV without J^π assignment.

^bThe literature [Xia07] reports a state at 2875.4 keV with a $J^\pi = 1^+(2^+)$ assignment.

^cYield has been determined from BR from [Xia07] data and from $I_\gamma(\rightarrow 2^+_1)$.



Bibliography

- [Ahn09] T. Ahn, L. Coquard, N. Pietralla et al. *Evolution of the $2_{1,ms}^+$ one-phonon mixed-symmetry state in $N = 80$ isotones as a local measure for the proton-neutron quadrupole interaction.* Phys. Lett. B **679** (2009) 19.
- [Ahn12] T. Ahn, G. Rainovski, N. Pietralla et al. *Identification of the $2_{1,ms}^+$ mixed-symmetry state in ^{136}Ce .* Phys. Rev. C **86** (2012) 014303.
- [Ala55] G. Alaga, K. Alder, A. Bohr, and B. Mottelson. *Intensity rules for beta and gamma transitions to nuclear rotational states.* Dan. Mat. Fys. Medd. **29** (1955) 1.
- [Ald56] K. Alder, A. Bohr, T. Huus, B. Mottelson, and A. Winther. *Study of Nuclear Structure by Electromagnetic Excitation with Accelerated Ions.* Rev. Mod. Phys. **28** (1956) 432.
- [Ald60] K. Alder and A. Winther. *On the Theory of Multiple Coulomb Excitation with Heavy Ions.* Mat. Fys. Medd. K. Dan. Vidensk. Selsk. **32** (1960).
- [Ald75] K. Alder and A. Winther. *Electromagnetic Excitation*, (North-Holland, 1975).
- [Ari76] A. Arima and F. Iachello. *Interacting boson model of collective states I. The vibrational limit.* Ann. Phys. **99** (1976) 253.
- [Ari77] A. Arima, T. Ohtsuka, F. Iachello, and I. Talmi. *Collective nuclear states as symmetric couplings of proton and neutron excitations.* Phys. Lett. B **66** (1977) 205.
- [Ari78a] A. Arima and F. Iachello. *Interacting boson model of collective nuclear states II. The rotational limit.* Ann. Phys. **111** (1978) 201.
- [Ari78b] A. Arima and F. Iachello. *New Symmetry in the sd Boson Model of Nuclei: The Group $O(6)$.* Phys. Rev. Lett. **40** (1978) 385.
- [ATL13] ATLAS webpage. *Floorplan of ATLAS.* <http://www.phy.anl.gov/atlas/facility/floorplan.html>, visited July 4th, 2013.

-
- [ATL14] ATLAS webpage. *ATLAS*. <http://www.phy.anl.gov/atlas/>, visited May 7th, 2014.
- [Bak78] C. Baktash, J. X. Saladin, J. J. O'Brien, and J. G. Alessi. *Electromagnetic properties of ^{194}Pt and the question of its triaxiality*. Phys. Rev. C **18** (1978) 131.
- [Bak79] F. T. Baker, A. Scott, T. Cleary et al. *$^{194}\text{Pt}(^{12}\text{C}, ^{12}\text{C}')$ reaction and the triaxial-rotor model*. Nucl. Phys. A **321** (1979) 222.
- [Bau09] C. Bauer. *Der $g(2_1^+)$ -Faktor im Radionuklid ^{140}Ba – Erste Anwendung der "Recoil-in-vacuum" Technik an REX-ISOLDE*. Master's thesis, TU Darmstadt, Germany, 2009.
- [Bau13] C. Bauer. *Level lifetimes and quadrupole moments from projectile Coulomb excitation of $A \approx 130$ nuclei*. Ph.D. thesis, TU Darmstadt, 2013.
- [Bea96] C. W. Beausang and J. Simpson. *Large arrays of escape suppressed spectrometers for nuclear structure experiments*. J. Phys. G Nucl. Part. Phys. **22** (1996) 527.
- [Ber72] I. Berkes, R. Rougny, M. Meyer-Lévy et al. *Electromagnetic Properties of Even-Even Platinum Nuclei*. Phys. Rev. C **6** (1972) 1098.
- [Ber81] G. Berrier-Ronsin, M. Vergnes, G. Rotbard et al. *Structure of ^{194}Pt via transfer reactions*. Phys. Rev. C **23** (1981) 2425.
- [Ber07] C. A. Bertulani. *Nuclear Physics in a Nutshell*, (Princeton University Press, 2007).
- [Boh84] D. Bohle, A. Richter, W. Steffen et al. *New magnetic dipole excitation mode studied in the heavy deformed nucleus ^{156}Gd by inelastic electron scattering*. Phys. Lett. B **137** (1984) 27.
- [Boh98] A. Bohr and B. Mottelson. *Nuclear deformations*. Nuclear Structure, (World Scientific, 1998).
- [Bol81] H. Bolotin, A. Stuchbery, I. Morrison et al. *Lifetimes of excited states in $^{196,198}\text{Pt}$; Application of interacting boson approximation model to even Pt isotopes systematics*. Nucl. Phys. A **370** (1981) 146.
- [Bol93] L. Bollinger, R. Pardo, K. Shepard et al. *The positive-ion injector of ATLAS: design and operating experience*. Nucl. Instrum. Methods. Phys. Res. B **79** (1993) 753.

-
- [Bör90] H. G. Börner, J. Jolie, S. Robinson, R. F. Casten, and J. Cizewski. *First measurement of $B(E2)$ values from $\sigma < N$ states of an $O(6)$ nucleus: Gamma-ray-induced Doppler broadening studies in ^{196}Pt .* Phys. Rev. C **42** (1990) R2271.
- [Bru97] R. Brun and F. Rademakers. *ROOT — An object oriented data analysis framework.* Nucl. Instrum. Methods. Phys. Res. A **389** (1997) 81.
- [Bur85] S. Burnett, A. Baxter, S. Hinds et al. *A measurement of $B(E3; 0^+ \rightarrow 3_1^-)$ and some $E2$ transition probabilities in $^{132,134,136,138}\text{Ba}$ using Coulomb excitation.* Nucl. Phys. A **432** (1985) 514.
- [Cas85] R. F. Casten and P. von Brentano. *An Extensive Region of $O(6)$ -Like Nuclei Near $A = 130$.* Phys. Lett. B **152** (1985) 22.
- [Cas88] R. F. Casten and D. D. Warner. *The interacting boson approximation.* Rev. Mod. Phys. **60** (1988) 389.
- [Cas00] R. F. Casten and N. V. Zamfir. *Evidence for a Possible $E(5)$ Symmetry in ^{134}Ba .* Phys. Rev. Lett. **85** (2000) 3584.
- [Cas01a] R. F. Casten. *Nuclear Structure from a Simple Perspective*, (Oxford University Press, 2001).
- [Cas01b] R. F. Casten and N. V. Zamfir. *Empirical Realization of a Critical Point Description in Atomic Nuclei.* Phys. Rev. Lett. **87** (2001) 052503.
- [Cas06] R. F. Casten. *Shape phase transitions and critical-point phenomena in atomic nuclei.* Nature Phys. **2** (2006) 811.
- [Ciz78] J. A. Cizewski, R. F. Casten, G. J. Smith et al. *Evidence for a New Symmetry in Nuclei: The Structure of ^{196}Pt and the $O(6)$ Limit.* Phys. Rev. Lett. **40** (1978) 167.
- [Ciz79] J. Cizewski, R. Casten, G. Smith et al. *The level structure of ^{196}Pt .* Nucl. Phys. A **323** (1979) 349.
- [Cle76] W. Cleveland and E. Zganjar. *Nuclear structure of ^{194}Pt .* Z. Phys. A **279** (1976) 195.
- [Coq09] L. Coquard, N. Pietralla, T. Ahn et al. *Robust test of $E(5)$ symmetry in ^{128}Xe .* Phys. Rev. C **80** (2009) 061304(R).

-
- [Coq10] L. Coquard, N. Pietralla, G. Rainovski et al. *Evolution of the mixed-symmetry $2_{1,ms}^+$ quadrupole-phonon excitation from spherical to γ -soft Xe nuclei*. Phys. Rev. C **82** (2010) 024317.
- [Coq11] L. Coquard, G. Rainovski, N. Pietralla et al. *O(6)-symmetry breaking in the γ -soft nucleus ^{126}Xe and its evolution in the light stable xenon isotopes*. Phys. Rev. C **83** (2011) 044318.
- [Cre] J. Creswell and J. Sampson. *MTsort*. Unpublished, University of Liverpool.
- [Dar] Daresbury Laboratory. *Multi Instance Data Acquisition System*. Unpublished.
- [Dea79] P. T. Deason, C. H. King, T. L. Khoo, J. A. Nolen, and F. M. Bernthal. *$^{194,196,198}\text{Pt}(p,t)$ reactions at 35 MeV*. Phys. Rev. C **20** (1979) 927.
- [Dew03] A. Dewald, O. Möller, D. Tonev et al. *Shape changes and test of the critical-point symmetry in $N = 90$ nuclei*. Eur. Phys. J. A **20** (2003) 173.
- [Dew05] A. Dewald, O. Möller, B. Saha et al. *Test of the critical point symmetry $X(5)$ in the mass $A = 180$ region*. J. Phys. G Nucl. Part. Phys. **31** (2005) S1427.
- [Die80] A. E. L. Dieperink, O. Scholten, and F. Iachello. *Classical Limit of the Interacting-Boson Model*. Phys. Rev. Lett. **44** (1980) 1747.
- [Dus05] K. Dusling and N. Pietralla. *Description of ground-state band energies in well-deformed even-even nuclei with the confined β -soft rotor model*. Phys. Rev. C **72** (2005) 011303.
- [Ebe08] J. Eberth and J. Simpson. *From Ge(Li) detectors to gamma-ray tracking arrays – 50 years of gamma spectroscopy with germanium detectors*. Prog. Part. Nucl. Phys. **60** (2008) 283 .
- [Epe09] E. Epelbaum, H.-W. Hammer, and U.-G. Meißner. *Modern theory of nuclear forces*. Rev. Mod. Phys. **81** (2009) 1773.
- [Faz92] B. Fazekas, T. Belgya, G. Molnár et al. *Level scheme and mixed-symmetry states of ^{134}Ba from in-beam $(n, n'\gamma)$ measurements*. Nucl. Phys. A **548** (1992) 249.

-
- [Few88] M. P. Fewell, G. Gyapong, and S. R. H. *Coulomb Excitation of the 4_1^+ States of $^{194,196,198}\text{Pt}$* . *Aust. J. Phys.* **41** (1988).
- [Fil81] A. J. Filo, S. W. Yates, D. F. Coope, J. L. Weil, and M. T. McEllistrem. *Positive- and negative-parity level structures of ^{194}Pt from $(n, n'\gamma)$ reaction spectroscopy*. *Phys. Rev. C* **23** (1981) 1938.
- [Fra01] C. Fransen, N. Pietralla, P. von Brentano et al. *First observation of a mixed-symmetry two-Q-phonon $2_{2,ms}^+$ state in ^{94}Mo* . *Phys. Lett. B* **508** (2001) 219.
- [Fra03] C. Fransen, N. Pietralla, Z. Ammar et al. *Comprehensive studies of low-spin collective excitations in ^{94}Mo* . *Phys. Rev. C* **67** (2003) 024307.
- [Gad00] A. Gade, I. Wiedenhöver, J. Gableske et al. *Proton–neutron structure of low lying collective quadrupole excitations in ^{126}Xe* . *Nucl. Phys. A* **665** (2000) 268.
- [Gam13] Gammasphere Website. *Gammasphere ROOT sorter*. <http://www.phy.anl.gov/gammasphere/doc/GSSort/>, visited October 14th, 2013.
- [Goe50] M. Goeppert Mayer. *Nuclear Configurations in the Spin-Orbit Coupling Model. I. Empirical Evidence*. *Phys. Rev.* **78** (1950) 16.
- [Hax49] O. Haxel, J. H. D. Jensen, and H. E. Suess. *On the “Magic Numbers” in Nuclear Structure*. *Phys. Rev.* **75** (1949) 1766.
- [Hic08] S. F. Hicks, J. R. Vanhoy, and S. W. Yates. *Fragmentation of mixed-symmetry excitations in stable even-even Tellurium nuclei*. *Phys. Rev. C* **78** (2008) 054320.
- [Iac87] F. Iachello and A. Arima. *The Interacting Boson Model*. Cambridge Monographs on Mathematical Physics, (Cambridge University Press, 1987).
- [Iac00] F. Iachello. *Dynamic Symmetries at the Critical Point*. *Phys. Rev. Lett.* **85** (2000) 3580.
- [Iac01] F. Iachello. *Analytic Description of Critical Point Nuclei in a Spherical-Axially Deformed Shape Phase Transition*. *Phys. Rev. Lett.* **87** (2001) 052502.
- [Isa86] P. van Isacker, K. Heyde, J. Jolie, and A. Sevrin. *The F-spin symmetric limits of the neutron-proton interacting boson model*. *Ann. Phys.* **171** (1986) 253.

-
- [Isa87] P. V. Isacker. *Quadrupole moments and E2 transitions with $\Delta\tau = 0, \pm 2$ in the γ -unstable $O(6)$ limit of the interacting boson model.* Nucl. Phys. A **465** (1987) 497.
- [Joh77] N. R. Johnson, P. P. Hubert, E. Eichler et al. *Lifetimes of ground-band states in ^{192}Pt and ^{194}Pt .* Phys. Rev. C **15** (1977) 1325.
- [Kat02] J. Katakura and K. Kitao. *Nucl. Data Sheets for $A = 126$.* Nucl. Data Sheets **97** (2002) 765.
- [Kha05] Y. Khazov, A. Rodionov, S. Sakharov, and B. Singh. *Nucl. Data Sheets for $A = 132$.* Nucl. Data Sheets **104** (2005) 497.
- [Kib05] T. Kibédi and R. Spear. *Electric monopole transitions between 0^+ states for nuclei throughout the periodic table.* At. Data Nucl. Data Tables **89** (2005) 77.
- [Kra87] K. S. Krane. *Introductory Nuclear Physics*, (Wiley, 1987).
- [Krü99] R. Krücken, C. J. Barton, C. W. Beausang et al. *Nature of excited 0^+ states in ^{154}Sm .* Phys. Lett. B **454** (1999) 15.
- [Krü02] R. Krücken, B. Albanna, C. Bialik et al. *$B(E2)$ Values in ^{150}Nd and the Critical Point Symmetry $X(5)$.* Phys. Rev. Lett. **88** (2002) 232501.
- [Kru11] A. Krugmann, Z. P. Li, J. Meng, N. Pietralla, and D. Vretenar. *Comparison of the confined β -soft rotor model and a microscopic collective Hamiltonian based on the relativistic mean field model in $^{150,152}\text{Nd}$.* J. Phys. G Nucl. Part. Phys. **38** (2011) 065102.
- [Lee90] I.-Y. Lee. *The GAMMASPHERE.* Nucl. Phys. A **520** (1990) c641.
- [Lee97] I. Lee. *Physics with GAMMASPHERE and beyond.* Prog. Part. Nucl. Phys. **38** (1997) 65.
- [Li09] Z. P. Li, T. Nikšić, D. Vretenar et al. *Microscopic analysis of nuclear quantum phase transitions in the $N = 90$ region.* Phys. Rev. C **79** (2009) 054301.
- [Lim92] C. Lim, R. Spear, M. Fewell, and G. Gyapong. *Measurements of static electric quadrupole moments of the 2_1^+ , 2_2^+ , 4_1^+ and 6_1^+ states of ^{196}Pt .* Nucl. Phys. A **548** (1992) 308.

-
- [Mar13] M. J. Martin. *Nucl. Data Sheets for A = 152*. Nucl. Data Sheets **114** (2013) 1497 .
- [Mau90] A. Mauthofer, K. Stelzer, J. Idzko et al. *Triaxiality and γ -softness in ^{196}Pt* . Z. Phys. A **336** (1990) 263.
- [May94] T. Mayer-Kuckuk. *Kernphysik*, (Teubner Stuttgart, 1994).
- [McG61] F. K. McGowan and P. H. Stelson. *Coulomb Excitation of the Second 2^+ States in W, Os, and Pt Nuclei*. Phys. Rev. **122** (1961) 1274.
- [Mil71] W. Milner, F. McGowan, R. Robinson, P. Stelson, and R. Sayer. *Coulomb excitation of $^{182,184,186}\text{W}$, $^{186,188,190,192}\text{Os}$ and $^{192,194,196,198}\text{Pt}$ with protons, ^4He and ^{16}O ions*. Nucl. Phys. A **177** (1971) 1.
- [Mol88] G. Molnár, R. A. Gatenby, and S. W. Yates. *Search for mixed-symmetry states in the $O(6)$ nucleus ^{134}Ba* . Phys. Rev. C **37** (1988) 898.
- [Möl06] O. Möller, A. Dewald, P. Petkov et al. *Electromagnetic transition strengths in ^{156}Dy* . Phys. Rev. C **74** (2006) 024313.
- [Möl09] T. Möller. *Projektil-Coulombanregung an ^{148}Sm und ^{154}Sm* . Master's thesis, TU Darmstadt, 2009.
- [Möl12] T. Möller, N. Pietralla, G. Rainovski et al. *Absolute β -to-ground band transition strengths in ^{154}Sm* . Phys. Rev. C **86** (2012) 031305.
- [Nat14] National Nuclear Data Center. *Information extracted from the Chart of Nuclides database*. <http://www.nndc.bnl.gov/chart/>, visited May 7th, 2014.
- [Nik09] T. Niksic, Z. P. Li, D. Vretenar et al. *Beyond the relativistic mean-field approximation. III. Collective Hamiltonian in five dimensions*. Phys. Rev. C **79** (2009) 034303.
- [Nol94] P. Nolan, F. Beck, and D. Fossan. *Large Arrays Of Escape-Suppressed Gamma-Ray Detectors*. Annu. Rev. Nucl. Part. Sci. **45** (1994) 561.
- [Ots78] T. Otsuka, A. Arima, F. Iachello, and I. Talmi. *Shell model description of interacting bosons*. Phys. Lett. B **76** (1978) 139.
- [Ots94] T. Otsuka and K.-H. Kim. *Multiphonon structure of γ -unstable or $O(6)$ nuclei*. Phys. Rev. C **50** (1994) R1768.

-
- [Owe] H. Ower, J. Gerl, and H. Scheit. *Computer code CLX*.
- [Owe80] H. Ower. *PhD Thesis*. Ph.D. thesis, Johann Wolfgang zu Goethe Universität zu Frankfurt am Main, 1980.
- [Pie94] N. Pietralla, P. von Brentano, R. F. Casten, T. Otsuka, and N. V. Zamfir. *Distribution of Low-Lying Quadrupole Phonon Strength in Nuclei*. Phys. Rev. Lett. **73** (1994) 2962.
- [Pie95] N. Pietralla, P. von Brentano, T. Otsuka, and R. Casten. *Odd-spin yrast states as multiple quadrupole-phonon excitations*. Phys. Lett. B **349** (1995) 1.
- [Pie98a] N. Pietralla, D. Belic, P. von Brentano et al. *Isovector quadrupole excitations in the valence shell of the vibrator nucleus ^{136}Ba : Evidence from photon scattering experiments*. Phys. Rev. C **58** (1998) 796.
- [Pie98b] N. Pietralla, P. von Brentano, A. Gelberg et al. *Symmetry changing transitions in γ -soft nuclei studied in the interacting boson model*. Phys. Rev. C **58** (1998) 191.
- [Pie99] N. Pietralla, C. Fransen, D. Belic et al. *Transition Rates between Mixed Symmetry States: First Measurement in ^{94}Mo* . Phys. Rev. Lett. **83** (1999) 1303.
- [Pie00] N. Pietralla, C. Fransen, P. von Brentano et al. *Proton-Neutron Mixed-Symmetry 3_{ms}^+ State in ^{94}Mo* . Phys. Rev. Lett. **84** (2000) 3775.
- [Pie01] N. Pietralla, C. J. Barton, R. Krücken et al. *Coulomb excitation of the 2_{ms}^+ state of ^{96}Ru in inverse kinematics*. Phys. Rev. C **64** (2001) 031301.
- [Pie03] N. Pietralla, C. Fransen, A. Gade et al. *Proton-neutron structure of the effective quadrupole-octupole coupled $E1$ transition operator*. Phys. Rev. C **68** (2003) 031305.
- [Pie04] N. Pietralla and O. M. Gorbachenko. *Evolution of the β excitation in axially symmetric transitional nuclei*. Phys. Rev. C **70** (2004) 011304.
- [Pie08] N. Pietralla, P. von Brentano, and A. F. Lisetskiy. *Experiments on multi-phonon states with proton-neutron mixed symmetry in vibrational nuclei*. Prog. Part. Nucl. Phys. **60** (2008) 225.

-
- [Rai06] G. Rainovski, N. Pietralla, T. Ahn et al. *Stabilization of Nuclear Isovector Valence-Shell Excitations*. Phys. Rev. Lett. **96** (2006) 122501.
- [Rai10] G. Rainovski, N. Pietralla, T. Ahn et al. *How close to the $O(6)$ symmetry is the nucleus ^{124}Xe ?* Phys. Lett. B **683** (2010) 11.
- [Rai14] *Private Communication*, 2014.
- [Rei09] C. Reich. *Nucl. Data Sheets for $A = 154$* . Nucl. Data Sheets **110** (2009) 2257.
- [Rut11] E. Rutherford. *The scattering of α and β Particles by Matter and the Structure of the Atom*. Philos. Mag. **21** (1911) 669.
- [Sch04] M. Scheck, H. von Garrel, N. Tsoneva et al. *Dipole strength distributions in the stable Ba isotopes $^{134-138}\text{Ba}$: A study in the mass region of a nuclear shape transition*. Phys. Rev. C **70** (2004) 044319.
- [Set91] A. Sethi, N. M. Hintz, D. N. Mihalidis et al. *Inelastic proton scattering from Pt isotopes and the interacting boson model*. Phys. Rev. C **44** (1991) 700.
- [Sie94] G. Siems, U. Neuneyer, I. Wiedenhöver et al. *Multiple quadrupole “phonon” excitations in ^{130}Ba* . Phys. Lett. B **320** (1994) 1.
- [Sin01] B. Singh. *Nucl. Data Sheets for $A = 130$* . Nucl. Data Sheets **93** (2001) 33.
- [Sin06] B. Singh. *Nucl. Data Sheets for $A = 194$* . Nucl. Data Sheets **107** (2006) 1531.
- [Son02] A. Sonzogni. *Nucl. Data Sheets for $A = 136$* . Nucl. Data Sheets **95** (2002) 837.
- [Son04] A. Sonzogni. *Nucl. Data Sheets for $A = 134$* . Nucl. Data Sheets **103** (2004) 1.
- [Ste77] K. Stelzer, F. Rauch, T. Elze et al. *Study of $E2$ transition probabilities in ^{194}Pt* . Phys. Lett. B **70** (1977) 297.
- [Stu03] A. E. Stuchbery. *γ -ray angular distributions and correlations after projectile-fragmentation reactions*. Nucl. Phys. A **723** (2003) 69.

-
- [Suh07] J. Suhonen. *From Nucleons to Nucleus: Concepts of Microscopic Nuclear Theory*. Theoretical and Mathematical Physics, (Springer, 2007).
- [Sul08] G. Suliman, D. Bucurescu, R. Hertenberger et al. *Study of the ^{130}Ba nucleus with the (p, t) reaction*. Eur. Phys. J. A **36** (2008) 243.
- [Tal93] I. Talmi. *Simple Models of Complex Nuclei*. Contemporary concepts in physics, (Taylor & Francis, 1993).
- [Van04] J. R. Vanhoy, J. A. Tanyi, K. A. Crandell et al. *Lifetimes in ^{126}Te from in-beam $(n, n'\gamma)$ measurements*. Phys. Rev. C **69** (2004) 064323.
- [War82] D. D. Warner and R. F. Casten. *Revised Formulation of the Phenomenological Interacting Boson Approximation*. Phys. Rev. Lett. **48** (1982) 1385.
- [War83] D. D. Warner and R. F. Casten. *Predictions of the interacting boson approximation in a consistent Q framework*. Phys. Rev. C **28** (1983) 1798.
- [Wer01] V. Werner, H. Meise, I. Wiedenhöver, A. Gade, and P. von Brentano. *Collective bands in the triaxial nucleus ^{124}Xe* . Nucl. Phys. A **692** (2001) 451.
- [Wil56] L. Wilets and M. Jean. *Surface Oscillations in Even-Even Nuclei*. Phys. Rev. **102** (1956) 788.
- [Win66] A. Winther and J. de Boer. *A computer program for multiple coulomb excitation*, p. 303, (Academic Press Inc., New York, 1966).
- [Wu96] C. Wu, D. Cline, T. Czosnyka et al. *Quadrupole collectivity and shapes of Os-Pt nuclei*. Nucl. Phys. A **607** (1996) 178.
- [Xia07] H. Xiaolong. *Nucl. Data Sheets for $A = 196$* . Nucl. Data Sheets **108** (2007) 1093.
- [Yam67] T. Yamazaki. *Tables of coefficients for angular distribution of gamma rays from aligned nuclei*. Nucl. Data A **3** (1967) 1.

List of Figures

1.1. Color-coded illustration of the ratio $R_{4/2}$ for the entire nuclear chart.	8
2.1. Qualitative illustration of the orbits resulting from the shell model.	13
2.2. Schematic low-lying level schemes of vibrating and rotating nuclei.	16
2.3. Schematic level scheme of a γ -soft nucleus; Relative energies of the levels in the ground state band of collective nuclei.	20
2.4. Symmetry triangle of the IBM.	25
2.5. Illustration of a typical O(6)-like levelscheme.	28
2.6. Illustration of the low-lying level scheme of the simplified IBM-2 Hamiltonian.	31
2.7. The decay signature of mixed-symmetric states.	33
2.8. Level scheme of the E(5) shape phase transitional point.	34
2.9. Level scheme of the X(5) shape phase transitional point.	36
2.10. Wave functions in the CBS rotor model.	37
3.1. Scattering angles θ_{sc} of projectile and recoil target nuclei of the ^{130}Ba experiment.	46
3.2. Floorplan of the ATLAS facility at the ANL.	51
3.3. Photograph of the Gammasphere array.	51
3.4. Photograph of a partly disassembled detector module of Gammasphere.	52
4.1. Determination of the velocity β for the Doppler correction.	56
4.2. Time spectrum and time gates of the ^{130}Ba experiment.	57
4.3. Time-energy matrix of the ^{130}Ba experiment.	58
4.4. Relative efficiency curve for the Pt experiment.	59
4.5. Multiplicity distribution of the events in the ^{194}Pt experiment.	61
4.6. $\gamma\gamma$ -coincidence matrix of the ^{194}Pt experiment.	61
4.7. Coincidence spectrum of the ^{132}Ba experiment gated on the $2_1^+ \rightarrow 0_1^+$ transition.	62
4.8. Sum spectrum of all detectors at different stages of the data analysis.	63
4.9. Angular distribution analysis of the $2_4^+ \rightarrow 2_1^+$ transition in ^{154}Sm	75
4.10. Singles spectrum of the ^{154}Sm experiment.	77

4.11. Singles and coincidence spectrum of ^{194}Pt	79
4.12. Singles and coincidence spectrum of ^{196}Pt	84
4.13. Singles spectrum of ^{130}Ba	90
4.14. Singles spectrum of ^{132}Ba	93
5.1. Strength distributions from the results of ^{130}Ba	99
5.2. Strength distributions from the results of ^{132}Ba	101
5.3. Evolution of the fragments of the $2_{1,\text{ms}}^+$ state in the Ba isotopic chain.	103
5.4. Overview on the $B(M1; 2^+ \rightarrow 2_1^+)$ strength distributions in the A = 130 mass region.	104
5.5. Evolution of the fragments of the $2_{1,\text{ms}}^+$ state in the N = 76 isotones.	106
5.6. Evolution of the fragments of the $2_{1,\text{ms}}^+$ state in the N = 74 isotones.	107
5.7. Overview of the results of the analysis of the ^{196}Pt experiment	110
5.8. Comparison of previous results on $B_{4/2}$ and $B_{2/2}$ of ^{196}Pt	112
5.9. Overview of the results of the analysis of the ^{194}Pt experiment	113
5.10. Comparison of previous results on $B_{4/2}$ and $B_{2/2}$ of ^{194}Pt	115
5.11. Overview on the present results of ^{154}Sm	118
B.1. Singles Sum Spectrum of the ^{130}Ba experiment.	125
B.2. Spectrum of ^{130}Ba coincident to the $2_1^+ \rightarrow 0_1^+$ transition.	126
B.3. Level scheme of the ^{130}Ba experiment.	127
B.4. Singles Sum Spectrum of the ^{132}Ba experiment.	129
B.5. Spectrum of ^{132}Ba coincident to the $2_1^+ \rightarrow 0_1^+$ transition.	130
B.6. Level scheme of the ^{132}Ba experiment.	131
B.7. Singles Sum Spectrum of the ^{154}Sm experiment.	136
B.8. Spectrum of ^{154}Sm coincident to the $2_1^+ \rightarrow 0_1^+$ transition.	137
B.9. Level scheme of the ^{154}Sm experiment.	138
B.10. Analysis of the angular distributions in ^{154}Sm	139
B.11. Singles Sum Spectrum of the ^{194}Pt experiment.	143
B.12. Spectrum of ^{194}Pt coincident to the $2_1^+ \rightarrow 0_1^+$ transition.	144
B.13. Spectrum of ^{194}Pt coincident to the $2_2^+ \rightarrow 2_1^+$ transition.	145
B.14. Level scheme of the ^{194}Pt experiment.	146
B.15. Singles Sum Spectrum of the ^{196}Pt experiment.	151
B.16. Spectrum of ^{196}Pt coincident to the $2_1^+ \rightarrow 0_1^+$ transition.	152
B.17. Spectrum of ^{196}Pt coincident to the $2_2^+ \rightarrow 2_1^+$ transition.	153
B.18. Level scheme of the ^{196}Pt experiment.	154

List of Tables

3.1. Polar angles θ_{Ge} of the detector rings of the Gammasphere array. . . .	53
3.2. Overview of the basic experimental parameters in the experiments. .	54
4.1. Results of the analysis of the ^{154}Sm data	76
4.2. Results of the analysis of the ^{194}Pt data	81
4.3. Results of the analysis of the ^{196}Pt data	86
4.4. Results of the analysis of the ^{130}Ba data	91
4.5. Results of the analysis of the ^{132}Ba data	95
5.1. Comparison of the present results of ^{154}Sm with X(5) and CBS pre- dictions.	117
B.1. Intensities of the transitions in the ^{130}Ba experiment	123
B.2. Yields of the states in the ^{130}Ba experiment	124
B.3. Intensities of the transitions in the ^{132}Ba experiment	128
B.4. Yields of the states in the ^{132}Ba experiment	132
B.5. Intensities of the transitions in the ^{154}Sm experiment	133
B.6. Yields of the states in the ^{154}Sm experiment	134
B.7. Intensities of the transitions in the ^{194}t experiment	140
B.8. Yields of the states in the ^{194}Pt experiment	147
B.9. Intensities of the transitions in the ^{196}Pt experiment	148
B.10. Yields of the states in the ^{196}Pt experiment	155



Acronyms

ANL Argonne National Laboratory

ATLAS Argonne Tandem Linear Accelerator System

BGO Bismuth-Germanate scintillator. Used for the suppression of Compton-scattered γ rays.

CBS Confined- β -soft rotor model. As a generalization of the X(5) solution it describes nuclei on the transition between the shape-phase transitional point and rigid deformation in the geometrical nuclear model.

Coulex Short for Coulomb excitation. The method is described in 3.1.

DAQ Data Acquisition system

E_{beam} Kinetic energy of the projectiles in the ion beam. Usually given in units of MeV

HO Harmonic Oscillator, described by the central potential $V(r) = 1/2 m\omega^2 r^2$.

HPGe Short for High-Purity Germanium detector

I_{beam} Beam intensity, sometimes referred to as beam current. It is a measure for how many projectile nuclei collide onto the target per unit of time. Usually given in units of pA.

IBM Interacting Boson Model, cf. sec 2.3

IBM-2 Interacting Boson Model 2. Extension of the IBM to also treat the proton-neutron degree of freedom, cf. sec 2.3.3

MSS Mixed symmetry states. States in the IBM-2 that have an F -spin of $F = F_{\text{max}} - 1$ and have wave functions non symmetric under the exchange of proton and neutron labels.

$R_{4/2}$ ratio of the excitation energies of the 4^+ and 2^+ Yrast states $E(2_1^+)/E(4_1^+)$.
Used as signature for collective behavior of a nucleus, cf. chapter 2.2.1.

W.u. Weisskopf unit or single particle unit. Cf. 3.2.2

Acknowledgements

Many people have a share in the completion of this work and I am very grateful for their support. In particular, I want to thank. . .

- my Professor, Norbert Pietralla, for the opportunity of working on this thesis. He has always been open for questions and discussions and provided valuable ideas on numerous issues of the analyses and their interpretation.
- Georgi Rainovski for the countless discussions we had on numerous issues with the analyses. He has always taken time for me and provided valuable input.
- the staff at ANL for providing excellent ion beams and for providing any kind of help with the Gammasphere spectrometer, especially to Shaofei Zhu and Darek Seweryniak for their extensive support during beam times even on weekends and during night shifts.
- Kim Lister for providing me with the experimental data of the Pt experiment he originally proposed, and Libby McCutchan for collaboration and for comparison of the intermediate results of our parallel analyses.
- my colleagues and friends with whom I shared office for many years: Tan Ahn and Laurent Coquard, who introduced the topic and the techniques of the analysis to me; Michael Reese and Robert Stegmann, who I frequently bothered with my programming questions; Christopher Bauer and Timo Bloch, with whom I had many discussions on our analyses.
- My colleagues and friends at the Institut für Kernphysik in Darmstadt, in particular Christopher Bauer, Timo Bloch, Robert Stegmann, Markus Zweidinger, Christopher Romig, Jacob Beller, Johann Isaak, Michael Thürauf, . . . for a lot of fun, recreation, and distraction, both on the job and after work; and, not to forget, countless discussions and conversations on challenges related to our work.

-
- Oliver Möller, Jörg Leske, Marcus Scheck, and Volker Werner, who I could always approach with questions and who have been very supportive since the times I started as a Bachelor student.
 - the administrative department of our institute, in particular Ursula von Dungen, Giovanna Umberti, and Marco Brunken, for handling most of the paperwork related to the funding of my work.
 - my parents, Bernhard and Margret Möller, for their unconditional and continuous support in any respect throughout my life.
 - my fiancée, Cathrin Wälzlein, for supporting and motivating me in stressful times, and for providing distraction from the daily routine.

This work was made possible by the financial support of the DFG under grant Nos. Pi393/2-2 and Pi393/2-3.

Lebenslauf

Persönliche Daten

Name	Thomas Wolfgang Möller
Geburtsdatum	01. April 1983
Geburtsort	Fulda
Staatsangehörigkeit	deutsch
Familienstand	ledig

Schulausbildung

1990 – 1994	Grundschule Fulda Gläserzell
1994 – 2003	Winfriedschule Fulda
Juni 2003	Abitur (Note 2,1)

Freiwilliges Soziales Jahr

2003 – 2004	Malteser Hilfsdienst gGmbH, Fulda
-------------	-----------------------------------

Hochschulausbildung

2004 – 2007	TU Darmstadt B.Sc. Physik (gut) <i>Multidetektor-γ-Spektroskopie nach Coulomb-Anregung des Edalgaskerns ^{126}Xe</i>
2007 – 2009	TU Darmstadt M.Sc. Physik (sehr gut) <i>Projekt-Coulombanregung an ^{148}Sm und ^{154}Sm</i>
seit 2009	TU Darmstadt, Promotionsstudium Arbeitsgruppe Prof. Dr. Dr. h.c. N. Pietralla



Erklärung zur Dissertation

Hiermit versichere ich, die vorliegende Dissertation ohne Hilfe Dritter nur mit den angegebenen Quellen und Hilfsmitteln angefertigt zu haben. Alle Stellen, die aus Quellen entnommen wurden, sind als solche kenntlich gemacht. Diese Arbeit hat in gleicher oder ähnlicher Form noch keiner Prüfungsbehörde vorgelegen.

Darmstadt, den June 25, 2014

(Thomas Möller)